ADDITIVE MANUFACTURING OF SHORT-FIBER COMPOSITES VIA STEREOLITHOGRAPHY

A Thesis
Submitted to the Graduate Faculty
of the
North Dakota State University
of Agriculture and Applied Science

By

Patrick Glenn Simpson

In Partial Fulfillment of the Requirements
for the Degree of
MASTER OF SCIENCE

Major Department:
Mechanical Engineering

December 2018

Fargo, North Dakota

North Dakota State University
Graduate School

Title

Additive Manufacturing of Short-Fiber Composites via Stereolithography

By

Patrick Glenn Simpson

The Supervisory Committee certifies that this ***disquisition*** complies with North Dakota State University's regulations and meets the accepted standards for the degree of

MASTER OF SCIENCE

SUPERVISORY COMMITTEE:

Dr. Chad Ulven
Chair

Dr. Dilpreet Bajwa

Dr. Dean Webster

Approved:

12/7/2018
Date

Dr. Alan R. Kallmeyer
Department Chair

ABSTRACT

The effectiveness of using a dual curing system, consisting of a photo and thermal initiator, for the additive manufacturing of carbon fiber short-fiber composites via stereolithography was investigated. The necessary processing parameters were developed that resulted in successful printing and curing of composites at a 5% fiber volume. The effects of layer height and print orientation of the short-fiber composites were evaluated for their effect on the material properties. There was no increase in the flexural modulus or fracture toughness, and a decrease the tensile and flexural strength of the short-fiber composites produced. This was found to be due to weak fiber/matrix interfacial properties, a wide fiber length distribution, and issues with fiber volume consistency. An increase in the tensile modulus was seen and that it could be manipulated with adjustments to layer height and part orientation.

ACKNOWLEDGEMENTS

I would like to thank the Army Research Laboratory for provide the funding for this research. I would like to thank my adviser, Dr. Chad Ulven, for providing thoughtful discussions, and guidance during this research. I would also like to thank my committee members, Dr. Dean Webster and Dr. Dilpreet Bajwa, for their advice during this research.

TABLE OF CONTENTS

ABSTRACT iii

ACKNOWLEDGEMENTS iv

LIST OF TABLES viii

LIST OF FIGURES xi

LIST OF APPENDIX TABLES xiv

LIST OF APPENDIX FIGURES xvii

1. INTRODUCTION 1

2. BACKGROUND 3

2.1. Stereolithography 3

2.1.1. Printing Methods 3

2.1.2. Printing Materials 4

2.1.3. Isotropic Material Properties 5

2.2. Short-Fiber Composites 6

2.3. Additive Manufacturing of Short-Fiber Composites 9

2.3.1. FDM Produced Short-Fiber Composites 9

2.3.2. SLA Produced Composites 12

2.4. Dual Cure Resin System 15

3. OBJECTIVES 16

4. RESEARCH METHODOLOGY 17

4.1. Materials and Equipment 17

4.1.1. Moai Printer 17

4.1.2. Photopolymer Resins 18

4.1.3. Carbon Fiber 18

4.1.4. Thermal Initiators 20

4.2. Sample Manufacturing 21
4.2.1. Resin Manufacturing 21
4.2.2. Processing Parameters for 3D Printing Parts 22
4.2.3. Post-Processing of 3D Printed Parts 25
4.3. Material Property Characterization of 3D Printed Composites 28
4.3.1. Thermal Initiator Selection 28
4.3.2. Viscosity Testing 29
4.3.3. Tensile Testing 31
4.3.4. Flexural Testing 34
4.3.5. Fracture Toughness Testing 36
4.3.6. Fiber Volume Consistency 38
4.3.7. Composite Void Content 40
4.3.8. Post-Cure Shrinkage 41
4.3.9. Scanning Electron Microscopy 42
5. RESULTS AND DISCUSSION 43
5.1. UV Cured Short Fiber Reinforced Composites 43
5.1.1. Tensile Testing 43
5.2. Dual Cured Short Fiber Reinforced Composite 45
5.2.1. Thermal Initiator Evaluation 45
5.2.2. Carbon Fiber Evaluation 50
5.2.3. Fiber Volume Consistency and Porosity 56
5.2.4. Material Characterization 59
6. CONCLUSIONS AND RECOMMENDATIONS 122
6.1. Conclusions 122
6.2. Future Recommendations 126

REFERENCES 128

APPENDIX A. EXPERIMENTAL DATA 134

APPENDIX B. STATISTICAL DATA 144

LIST OF TABLES

Table Page

2.1: Mechanical properties of commercially available SLA resins. 5

4.1: Peopoly resin constituents [9]. 18

4.2: Mechanical properties of various carbon fiber [41]. 19

4.3: Toray T-700 fiber properties [42]. 20

4.4: Carbiso MF SM45R-100 fiber properties [43]. 20

4.5 Thermal initiators to be investigated for a dual cure resin system. 21

4.6: Tensile testing experimental variables. 32

4.7: Tensile testing test matrix. 33

4.8: $Q_{critical}$ for Tukey HSD tension testing. 34

4.9: Flexural testing experimental variables. 35

4.10: Flexural testing test matrix. 36

4.11: Fracture toughness testing experimental variables. 37

4.12: Fracture toughness testing test matrix. 38

4.13: Qcritical for Tukey HSD fracture toughness testing. 38

4.14: Post-cure shrinkage test samples. 41

5.1: Tensile testing results for UV cured at 5% V_f carbon fiber. 44

5.2: Thermal initiator solubility and stability testing. 46

5.3: Thermal initiator onset temperature from DSC curves. 47

5.4: Viscosity of composite resins. 47

5.5: Printer settings changed for printing with carbon fiber resin. 51

5.6: Tensile testing results for Carbiso carbon fiber. 52

5.7: Tensile testing results for Toray T-700 carbon fiber. 54

5.8: Post-curing study for carbon fiber composite (Luperox P). 54

5.9: Post-curing study for carbon fiber composite (Cumene Hydroperoxide)..... 55
5.10: Summarized fiber volume consistency results for flexural samples..... 56
5.11: Density and void content of composite samples..... 58
5.12: Sample identification guide. 60
5.13: Summarized tensile testing results..... 63
5.14: Volumetric shrinkage (%) of post-cured samples..... 66
5.15: Statistical analysis groups..... 72
5.16: ANOVA summary for Young's modulus in 0º print orientation. 72
5.17: Tukey HSD results for Young's modulus in 0º print orientation..... 74
5.18: ANOVA summary for Young's modulus in 90º print orientation. 75
5.19: ANOVA summary for Young's modulus printed at 100 μm layer height. 76
5.20: Tukey HSD results for Young's modulus printed at 100 μm layer height..... 78
5.21: ANOVA summary for Young's modulus printed at 50 μm layer height. 78
5.22: Tukey HSD results for Young's modulus printed at 50 μm layer height..... 80
5.23: ANOVA summary for tensile strength in 0º print orientation..... 81
5.24: Tukey HSD results for tensile strength in 0º print orientation..... 82
5.25: ANOVA summary for tensile strength in 90º print orientation..... 82
5.26: Tukey HSD results for tensile strength in 90º print orientation..... 84
5.27: ANOVA summary for tensile strength printed at 100 μm layer height..... 84
5.28: Tukey HSD results for tensile strength printed at 100 μm layer height. 86
5.29: ANOVA summary for tensile strength at 50 μm layer height. 86
5.30: Tukey HSD results for tensile strength printed at 50 μm layer height. 88
5.31: Summarized flexural testing results..... 91
5.32: ANOVA summary for flexural modulus in 0º print orientation..... 93
5.33: Tukey HSD results for flexural modulus in 0º print orientation..... 95

5.34: ANOVA summary for flexural modulus in 90º print orientation. 95
5.35: Tukey HSD results for flexural modulus in 90º print orientation. 97
5.36: ANOVA summary for flexural modulus printed at 100 μm layer height. 97
5.37: Tukey HSD results for flexural modulus printed at 100 μm layer height. 99
5.38: ANOVA summary for flexural modulus printed at 50 μm layer height. 99
5.39: Tukey HSD results for flexural modulus printed at 50 μm layer height. 101
5.40: ANOVA summary for flexural strength in 0º print orientation. 101
5.41: Tukey HSD results for flexural strength in 0º print orientation. 103
5.42: ANOVA summary for flexural strength in 90º print orientation. 104
5.43: Tukey HSD results for flexural strength in 90º print orientation. 105
5.44: ANOVA summary for flexural strength printed at 100 μm layer height. 106
5.45: Tukey HSD results for flexural strength printed at 100 μm layer height. 107
5.46: ANOVA summary for flexural strength at 50 μm layer height. 108
5.47: Tukey HSD results for flexural strength printed at 50 μm layer height. 110
5.48: Summarized fracture testing results. 113
5.49: ANOVA summary for fracture toughness in the 0º print orientation. 115
5.50: ANOVA summary for fracture toughness in the 90º print orientation. 116
5.51: ANOVA summary for fracture toughness of 100 μm layer height. 118
5.52: ANOVA summary for fracture toughness of 50 μm layer height. 120

LIST OF FIGURES

Figure Page

2.1: Bottom-up SLA printer. 4

2.2: Schematic of layers SLA printing process. 6

2.3: Dual curing system. 15

3.1: Effects of layer height on fiber orientation. 16

4.1: Moai SLA printer. 18

4.2: Before (left) and after (right) support material being added. 23

4.3: Cura slicing software. 24

4.4: Sample long axis orientation. 25

4.5: UV cure oven. 26

4.6: Post-curing oven. 27

4.7: Surface defects from support removal. 27

4.8: Removal of supports and surface effects. 28

4.9: AR-G2 rheometer. 30

4.10: Tensile testing specimen (all dimensions in mm). 31

4.11: Flexural testing specimen (all dimensions in mm). 35

4.12: SENB specimen for fracture testing (all dimensions in mm). 37

4.13: Burn off sample testing areas. 39

4.14: Thermolyne muffle furnace. 40

4.15: Void content and density test specimen (all dimensions mm). 41

5.1: Representative stress-strain curves. 44

5.2: Viscosity testing with for shear rate from 1 s^{-1} to 25 s^{-1}. 48

5.3: Viscosity testing with for shear rate from 1 s^{-1} to 100 s^{-1}. 49

5.4: Milled Toray T-700 fiber length distribution. 50

5.5: SEM imaging of fracture surface of Carbiso fiber composite. 53
5.6: Cracks in cumene hydroperoxide post-cured specimens. 56
5.7: Tensile strength results for 0º print orientation. 61
5.8: Young's modulus results for 0º print orientation. 61
5.9: Tensile stregnth results for 90º print orientation. 62
5.10: Young's modulus results for 90º print orientation. 62
5.11: Fracture surface of CF50-0 (A) X200 and (B) X250 magnification. 64
5.12: Fracture surface of (A) CF100-90 and (B) CF50-90 specimens. 65
5.13: Surface cracking from thermal curing. 66
5.14: M100-90 fracture surface at (A) X500 and (B) X1000 magnification. 67
5.15: M50-90 fracture surface at (A) X500 and (B) X1000 magnification. 68
5.16: LP100-0 fracture surface at (A) X500 and (B) X1000 magnification. 69
5.17: Cracks in CF50-90 sample from printing. 70
5.18: Examples of CF50-90 print failures. 70
5.19: Box plot of ANOVA results for Young's modulus in 0º print orientation. 73
5.20: Box plot of ANOVA results for Young's modulus in 90º print orientation. 75
5.21: Box plot of ANOVA results for Young's modulus printed at 100 μm layer height. 77
5.22: Box plot of ANOVA results for Young's modulus printed at 50 μm layer height. 79
5.23: Box plot of ANOVA results for tensile strength in 0º print orientation. 81
5.24: Box plot of ANOVA results for tensile strength in 90º print orientation. 83
5.25: Box plot of ANOVA results for tensile strength printed at 100 μm layer height. 85
5.26: Box plot of ANOVA results for tensile strength printed at 50 μm layer height. 87
5.27: Flexural strength results for 0º print orientation. 89
5.28: Flexural modulus results for 0º print orientation. 90
5.29: Flexural stregnth results for 90º print orientation. 90

5.30: Flexural modulus results for 90º print orientation. 91
5.31: Box plot of ANOVA results for flexural modulus in 0º print orientation. 94
5.32: Box plot of ANOVA results for flexural modulus in 90º print orientation. 96
5.33: Box plot of ANOVA results for flexural modulus printed at 100 μm layer height. 98
5.34: Box plot of ANOVA results for flexural modulus printed at 50 μm layer height. 100
5.35: Box plot of ANOVA results for flexural strength in 0º print orientation. 102
5.36: Box plot of ANOVA results for flexural strength in 90º print orientation. 104
5.37: Box plot of ANOVA results for flexural strength printed at 100 μm layer height. 106
5.38: Box plot of ANOVA results for flexural strength printed at 50 μm layer height. 109
5.39: Fracture toughness for 0º print orientation. 112
5.40: Fracture toughness for 90º print orientation. 112
5.41: Fracture testing specimens. 113
5.42: Box plot of ANOVA results for fracture toughness in the 0º print orientation. 115
5.43: Box plot of ANOVA results for fracture toughness in the 90º print orientation. 117
5.44: Box plot of ANOVA results for fracture toughness of 100 μm layer height. 119
5.45: Box plot of ANOVA results for fracture toughness of 50 μm layer height. 120

LIST OF APPENDIX TABLES

Table Page

A.1: Fiber volume consistency for 100 μm layer height. 140

A.2: Fiber volume consistency for 50 μm layer height. 140

A.3: Density measurements results. 141

A.4: Void content measurement results. 141

A.5: Shrinkage due to post-curing M100. 142

A.6: Shrinkage due to post-curing M50. 142

A.7: Shrinkage due to post-curing LP100. 142

A.8: Shrinkage due to post-curing LP50. 143

A.9: Shrinkage due to post-curing CF100. 143

A.10: Shrinkage due to post-curing CF50. 143

B.1: ANOVA summary for Young's modulus 0º print orientation. 144

B.2: Tukey HSD results Young's modulus 0º print orientation. 144

B.3: ANOVA summary for Young's modulus 90º print orientation. 145

B.4: Tukey HSD results Young's modulus 90º print orientation. 145

B.5: ANOVA summary for Young's modulus printed at 100 μm layer height. 146

B.6: Tukey HSD results for Young's modulus printed at 100 μm layer height. 146

B.7: ANOVA summary for Young's modulus printed at 50 μm layer height. 147

B.8: Tukey HSD results for Young's modulus printed at 50 μm layer height. 147

B.9: ANOVA summary for tensile strength 0º print orientation. 148

B.10: Tukey HSD results tensile strength 0º print orientation. 148

B.11: ANOVA summary for tensile strength 90º print orientation. 149

B.12: Tukey HSD results tensile strength 90º print orientation. 149

B.13: ANOVA summary for tensile strength printed at 100 μm layer height. 150

B.14: Tukey HSD results for tensile strength printed at 100 μm layer height. 150
B.15: ANOVA summary for tensile strength printed at 50 μm layer height. 151
B.16: Tukey HSD results for tensile strength printed at 50 μm layer height. 151
B.17: ANOVA summary for flexural modulus 0º print orientation. 152
B.18: Tukey HSD results flexural modulus 0º print orientation. 152
B.19: ANOVA summary for flexural modulus 90º print orientation. 153
B.20: Tukey HSD results flexural modulus 90º print orientation. 153
B.21: ANOVA summary for flexural modulus printed at 100 μm layer height. 154
B.22: Tukey HSD results for flexural modulus printed at 100 μm layer height. 154
B.23: ANOVA summary for flexural modulus printed at 50 μm layer height. 155
B.24: Tukey HSD results for flexural modulus printed at 50 μm layer height. 155
B.25: ANOVA summary for flexural strength 0º print orientation. 156
B.26: Tukey HSD results flexural strength 0º print orientation. 156
B.27: ANOVA summary for flexural strength 90º print orientation. 157
B.28: Tukey HSD results flexural strength 90º print orientation. 157
B.29: ANOVA summary for flexural strength printed at 100 μm layer height. 158
B.30: Tukey HSD results for flexural strength printed at 100 μm layer height. 158
B.31: ANOVA summary for flexural strength printed at 50 μm layer height. 159
B.32: Tukey HSD results for flexural strength printed at 50 μm layer height. 159
B.33: ANOVA summary for fracture toughness 0º print orientation. 160
B.34: Tukey HSD results fracture toughness 0º print orientation. 160
B.35: ANOVA summary for fracture toughness 90º print orientation. 161
B.36: Tukey HSD results fracture toughness 90º print orientation. 161
B.37: ANOVA summary for fracture toughness printed at 100 μm layer height. 162
B.38: Tukey HSD results for fracture toughness printed at 100 μm layer height. 162

B.39: ANOVA summary for fracture toughness printed at 50 μm layer height. 163

B.40: Tukey HSD results for fracture toughness printed at 50 μm layer height. 163

LIST OF APPENDIX FIGURES

Figure Page

A.1: DSC curves for Moai resin. 134

A.2: DSC curves for Luperox P. 134

A.3: DSC curves for dicumyl peroxide 135

A.4: DSC curves for cumene hydroperoxide. 135

A.5: Moai resin viscosity curve 1 s^{-1} to 25 s^{-1} 136

A.6: Moai resin viscosity curve 1 s^{-1} to 100 s^{-1} 136

A.7: Moai resin + Luperox P viscosity curve 1 s^{-1} to 25 s^{-1}. 137

A.8: Moai resin + Luperox P viscosity curve 1 s^{-1} to 100 s^{-1}. 137

A.9: Moai resin + carbon fiber viscosity curve 1 s^{-1} to 25 s^{-1}. 138

A.10: Moai resin + carbon fiber viscosity curve 1 s^{-1} to 100 s^{-1}. 138

A.11: Moai resin + carbon fiber + Luperox P viscosity curve 1 s^{-1} to 25 s^{-1}. 139

A.12: Moai resin + carbon fiber + Luperox P viscosity curve 1 s^{-1} to 100 s^{-1}. 139

1. INTRODUCTION

In the 1980s, the ability for engineers to bring virtual models into the real world directly became a possibility with the advent of the first 3D printing method, stereolithography (SLA) [1]. This impacted the design process by providing a way of streamlining prototyping, proof of concepts, design verification, and allowed for the production of complex geometries that could not be made using traditional manufacturing methods. While SLA was the first patented 3D printing method there are several other methods currently in use such as: fusion deposition modeling (FDM), jetted photopolymer (PolyJet), selective laser sintering (SLS), and laminated object manufacturing (LOM). Although the different methods can vary through the materials they use, and differences in manufacturing techniques the overall process is the same. The manufacturing of a part is accomplished by using a computer-controlled process that adds material together in a layer-by-layer process, known as additive manufacturing (AM). In this process a virtual model of the part to be made is created with the use of computer-aided design software. The virtual model is then sliced into multiple layers along a plane in one direction, the toolpath for the creation of the part is defined, and the part is created on a computer controlled machine.

A current drawback of AM parts is that the material properties of the parts produced are much lower than that of parts manufactured using traditional manufacturing such as milling, injection molding, and traditional composite manufacturing methods [2-4]. If the material properties of the parts produced using AM could be increased to be on par with that of traditional manufacturing methods a new era of design could be opened up. This would be accomplished by the ability to use AM to make parts that could not be produced using any other methods due to their complex geometry. With the advent of computer aided design (CAD) software the design

process was changed, but we are still limited by what can be made in the virtual world and what can be manufactured in the real world. With the incorporation of AM into the final production processes the complexity of the geometries that could be manufactured increases. This increase in complexity of part geometry can allow for a decrease in the over complexity of the part, sub-assembly, or whole assembly, along with helping to relieve supply chain issues. For instance, by combing multiple parts into one you can remove the need for several fasteners. This will decrease the number of parts needed, number of components to analyze, and possible points of failure.

The research conducted to investigate methods to further develop the capabilities of AM by increasing the material properties of parts manufactured using SLA, is detailed in the 5 remaining sections. The second section will look at different SLA methods, and the current state of research in the area of using short fibers as a reinforcement to in AM. The third section provides the objectives of this research to develop and evaluate the processes involved to manufacture a short fiber composite part using SLA. The fourth section includes methodology that will be used to meet the objectives in regards to the materials and machines that will be used, the processes undertaken for manufacturing samples, and the design of the experiments to be used in characterization of the materials produced. The fifth section summarizes the results of the research by looking at the properties of the commercially available resin being used, and comparing that to the effects of incorporating short fiber as a reinforcement. The sixth section summarizes the results, and provides some recommendations for future research.

2. BACKGROUND

2.1. Stereolithography

SLA manufactures objects by curing a liquid photopolymer resin into a solid object via a computer control light source. The polymer used is typically an acrylic functionalized monomer that are polymerized by free radical polymerization. The free radicals used in SLA are photoinitated by a light source employed in the machine. The light used can be ultraviolet laser or even digital projection units, as long as the wavelength generated is within that of the wavelength need to cause initiation of the free radical. To accurately produced parts there are numerous aspects to take into consideration ranging from the chemistry aspects of the resin used, physics behind the optics for the lasers, or the necessary software to correct for distortions. For an in depth look at the principals of SLA the book, “Rapid Prototyping & Manufacturing Fundamentals of Stereolithography” by Paul F. Jacobs covers all aspects of the process [5].

2.1.1. Printing Methods

Within SLA there are different styles of printers that can be differentiated based off of the direction the part is moved during printing, and the direction/source of the UV light that is applied to the resin. The different types of SLA can be broken down into three main categories: top-down, continuous liquid interface production (CLIP), and bottom-up.

For the top-down method a build platform is lowered into a vat of liquid resin dropping one layer height at a time. The UV light source is then projected downward tracing out the 2D geometry of that part for the layer. As each layer is completed the part is lowered down and the process is repeated. The CLIP method uses a digital light-processing imaging unit to project UV light through an oxygen-permeable window at the bottom of the unit, while the part is raised vertically out of the resin [6]. This production method can allow for much higher printing speeds

when compared to the bottom-up or top-down methods due to the continuous nature of the production process when compared to the sequential process of the other two methods [6]. For the bottom-up method the build plate is lowered into a small vat of liquid resin and held one layer height above the bottom of the vat, and the UV light source is projected up through the vat tracing out the 2D geometry. After one layer is finished, a peel step is needed to separate the solid resin layer from the build plate. The build plate is then raised to allow liquid resin to coat the vat underneath the part, and the build platform is moved into positon for the next layer. The basic components of a bottom-up SLA printer are shown in Figure 2.1.

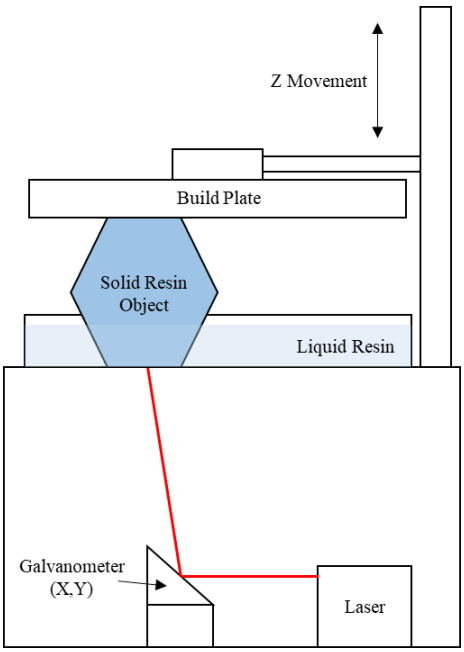

Figure 2.1: Bottom-up SLA printer.

2.1.2. Printing Materials

Currently most SLA printers use acrylic and epoxy base polymers, with acrylic being the more commonly used material [2]. Table 2.1 shows the tensile strength and Young's modulus of a few commercially available resins for desktop SLA printers [7-9].

Table 2.1: Mechanical properties of commercially available SLA resins.

Brand	Type	Tensile Strength (MPa)	Young's Modulus (GPa)
DruckWege Resin Type D [7]	Epoxy	35.7	1.56
Formlabs Clear FLGPCL03 [8]	Acrylic	65.0	2.80
Moai Standard Resin [9]	Acrylic	60.0	0.83

While Table 1 shows the material properties for a given resin as stated from the manufacturer, other factors can influence the actual materials properties of parts produced. One of the most important of these is the post-cure procedure followed after printing [10]. Most post-cure processes are done at an elevated temperature while exposing the part to a UV light source for a set amount of time. Depending on the type of light source (LED, incandescent bulb, or the sun), intensity of the light source, and the thickness of the part, the post-curing parameters can have a large effect on the material properties of the final part [10].

2.1.3. Isotropic Material Properties

An appealing advantage of SLA over other 3D printing methods, such as FDM, is the ability to manufacture parts that have isotropic material properties [11]. For parts produced using FDM, the part has the properties of the material in the plane of printing, but perpendicular to that it becomes dependent on the mechanical adhesion of the polymer layers to each other for the part's mechanical properties [11]. This is due to the part being produced using a thermoplastic material that is heated and extruded to form the layers. Although the individual strands that make up the layers are small, each line has cooled to a certain extent before the next line is applied, and this process does not allow for the entanglement of the polymer chains from one line to the next, and therefore limiting the mechanical properties to that of the adhesion of one line to the next.

For parts manufactured using SLA it is possible to produce parts that have near isotropic mechanical properties [11]. Although the part is produced in a layer-by-layer process, as like in

FDM, the thermoset polymer is not completely cured with in the layer before the part is raised and the next layer is printed. This allows for unreacted polymer functional groups in a previous layer to react with the polymer getting cured in the current layer. A schematic of this is shown in Figure 2.2.

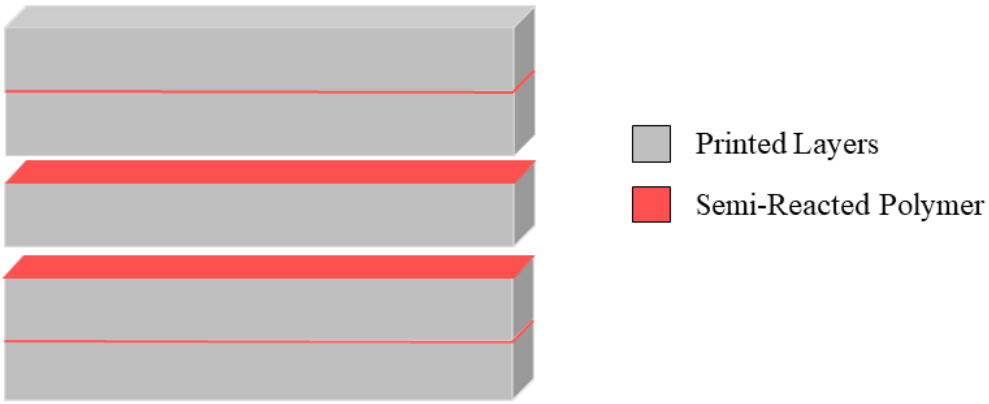

Figure 2.2: Schematic of layers SLA printing process.

Because of the ability of SLA to produced parts with isotropic properties, the orientation of the part while printing does not depend on what direction force will be applied to the finished part, but what orientation of the part will optimize the printing process.

2.2. Short-Fiber Composites

One of the limiting factors of SLA is the material properties of the resins used to create parts. The parts produced using these resins are weak and brittle, limiting their use for many end use structural applications [12]. One method of improving the properties of a material is the incorporation of a reinforcement material in the creation of a composite. Short-fiber composites have traditional been produced via injection and compression molding, and by using short-fibers as a reinforcement the same manufacturing methods used for polymers can be used to form the composites, but with increased material properties [13].

For sort-fiber composites the composites properties are a function of the fiber length due to the inclusion of end effects from the fiber [13]. The end effects of the fibers effect the stress transfer within the composite and have a large effect of the behavior and failure of the composites themselves. There have been numerous publications related to the theory of stress transfer between the matrix and fiber with a shear-lag model being a more common approach when analyzing and predicting mechanical behavior [13, 14]. An important aspect from the shear-lag model is the need for a minimum fiber length in which the maximum allowable fiber stress can be achieved. This is known as the critical fiber length l_c shown in Equation 2.1.

$$l_c = \frac{\sigma_{fu} d}{2\tau_y} \tag{2.1}$$

Where σ_{fu} is the ultimate fiber strength, τ_y is the matrix yield stress in shear, and d is the fiber diameter [13]. When the fiber is shorter then this the stress transfer from the matrix to the fiber is limited and the reinforcement is not as effective, due to the matrix or interface failing instead of the fiber itself [13]. As the fiber length is increased longer than the critical length the reinforcement becomes more effective, and at much longer lengths (50 times l_c) can considered continuous [13]. The ends of the fibers also play and important role in the behavior and properties of the composite. The fiber ends act as stress concentrators within the composite, lowering both the elastic modulus and strength [13].

To evaluate the effectiveness of the SLA process a theoretical prediction of the modulus can be used to evaluate the properties of the samples manufactured. The Halpin-Tsai equations (Equations 2.2 thru 2.5) allow for the theoretical prediction of the Young's Modulus for a unidirectional short fiber composite, and then an empirical equation can be used to predict the Young's Modulus of a randomly oriented short fiber composite [13]. The longitudinal modulus can be found from,

$$E_L = \left[\frac{1 + \left(2l/d\right)\eta_L V_f}{1 - \eta_L V_f}\right] E_m \,, \tag{2.2}$$

and the transverse modulus can be found by,

$$E_T = \left[\frac{1 + 2\eta_T V_f}{1 - \eta_T V_f}\right] E_m \,, \tag{2.3}$$

where,

$$\eta_L = \frac{\left(E_f/E_m\right) - 1}{\left(E_f/E_m\right) + 2\left(l/d\right)}, \tag{2.4}$$

and,

$$\eta_L = \frac{\left(E_f/E_m\right) - 1}{\left(E_f/E_m\right) + 2}, \tag{2.5}$$

where E_f is the Young's Modulus of the fiber, E_m is the Young's modulus of the matrix, V_f is the fiber volume content, l is the fiber length, and d is the fiber diameter [13]. The Young's modulus for a randomly distributed short fiber composite, E_R, can then be found from Equation 2.6,

$$E_R = \frac{3}{8}E_L + \frac{5}{8}E_T \tag{2.6}$$

Short-fiber composites usually find their applications in situations where isotropic material properties are desired. Unlike continuous fiber composites that are composed of layers of fibers in one direction, short-fiber composites ideally are non-layered with fibers randomly distributed in all directions, allowing for isotropic properties [13]. Short-fiber composites are traditionally manufactured via injection or compression molding, and these manufacturing processes can influence the fiber orientation due to the flow of the material during manufacturing

final material properties [15]. While the flow induced alignment can be taken advantage of to some extent, it can be limited due to the requirements of the mold design, and can be an undesired effect when isotropic properties are desired [16]. To aid in design there have been several analytical and experimental papers published in the area of fiber ordination and distribution and their effects on the final material properties of parts produced using traditional manufacturing methods [15-21].

2.3. Additive Manufacturing of Short-Fiber Composites

With short fibers already in wide spread use as a reinforcement material for traditional manufacturing methods, such as injection and compression molding, they have found their way into use for additive manufacturing methods as well [2, 4, 22-32]. The following sections will highlight the research being carried out in the area of the AM of composites, based off of the additive manufacturing method being used, specifically focusing on FDM and SLA technology.

2.3.1. FDM Produced Short-Fiber Composites

For FDM there are numerous types of reinforcements ranging from nanoparticle to continuous fiber, of both natural and synthetic materials, that are currently being researched and available for sell on a commercial level [2, 4, 29]. For the purpose of this research, the review of current literature will be limited to the area of carbon fiber reinforced FDM materials.

While there are several studies that have looked at using continuous fiber as a reinforcement in FDM, there are commercially available printers made by Markforged, USA. The MarkOne printer can use a variety of fiber reinforcements such as glass, carbon, and Kevlar with a nylon matrix. In an article by Goh G. et al [22] they looked at the mechanical properties of specimens manufactured using the MarkOne printer made with both glass and carbon fiber reinforcement. They found that the stiffness and strength was increased when compared to

samples made of just nylon, but the properties where less than that of traditional composite manufacturing methods [22]. The reason identified for this was the porosity of the extruded material, voids with the layers, and weak bonding between the layers due to the lack of consolidation within the manufacturing process [22].

A large amount of prior research and literature is available in the area of short carbon fiber composites manufactured using FDM with a variety of matrix materials. In work by Ferreira R. et al [23] they looked at using short carbon fiber as a reinforcement in a polylactic acid (PLA) matrix. They compared a commercial available PLA printer filament with that of a commercial available PLA filament with 15% weight carbon fiber. The study looked at the effects of the print orientation on the material properties by holding the printing parameters the same and varying the direction in which the test sample was printed. This samples were printed with all layers in the same direction to best replicate a unidirectional laminate composite. Ferreira R. et al found that the carbon fiber increased the stiffness the most (220%) in the printing direction (longitudinal), while some improvement (160%) was seen in the transverse stiffness [23]. They also observed a decrease in the tensile strength in all directions with this being attributed to poor adhesion between the matrix and fiber [23]. It was also noted that the printing process aligned the carbon fibers in the printing direction, and that voids were present in the samples that where left behind by the printing process [23].

Work done by Ning F. et al [24] looked at the effects of different carbon fiber weight percent on the material properties of composites parts made with an acrylonitrile butadiene styrene (ABS) matrix. The samples were prepared using carbon fibers of 100 μm and 150 μm in length at different fiber weights of 3, 5, 7.5, 10, and 15 percent, and both tensile and flexural properties were investigated. The result suggested that the maximum improvements to tensile

strength, Young's modulus, flexural strength, flexural modulus, and flexural toughness at a fiber weight of 5% [24]. Above 5 wt.% the resulting mechanical properties began to decrease back to or below that of the pure ABS samples, this being attributed to an increase in porosity within the samples [24]. The authors found that as the carbon fiber amount was increased so did the number void amount of the specimen, with the pores being generated due to gas evolution and physical gap at the layer interfaces [24]. It was also found by Ning F. et al that increasing the fiber length from 100 μm to 150 μm increased the tensile strength and Young's modulus there was no difference in the yield strength [24]. Ning F. et al study highlights one of the drawbacks of FDM, being that the fabrication processes results in voids left in the sample in the form of gaps between the layers and the individual extruded lines making up the layers themselves.

The work done by Tekinalp et al. [28] evaluated the material properties of carbon fiber reinforced ABS, for fiber weights of 10, 20, 30, and 40 percent, and looked at the fiber orientation effects of the FDM process. To accomplish this the Tekinalp et al. compared samples prepare by both compression molding and FDM printing, and found that the FDM printing process highly orientated the fibers in the printing direction [28]. While both samples had increased tensile strength and Young's modulus, due to the porosity in the FDM samples the compression molded samples had overall higher properties [28]. While the fibers are orientated in the direction of printing that direction is might not always be the direction of loading in a part due to the different infill patterns available, and how the FDM process can vary depending on what software is used. Tekinalp et al. point out, like others, that the porosity generated be the FDM printing process has a negative effect on the material properties and is an issue that will need to be addressed to further increase material properties [28].

From the literature, carbon fiber can offer a method of increasing the material properties for FDM, but one of the main areas of concern that was pointed out was the formation of voids and gaps due to the FDM printing process [23, 24, 28]. There is also the issue of the effect of the printing processing parameters themselves. These include the nozzle temperature, bed temperature, print speed, layer height, air gap, nozzle diameter, infill amount, infill pattern, and number of perimeters to name a few. Changing few of these parameters can have an effect on mechanical properties of the parts produced from the same material, as shown by Lanzotti A. et al [33].

2.3.2. SLA Produced Composites

Whereas FDM based methods have a number of publications in the area of short fiber composite characterization, the area of SLA manufactured composites is lacking in published studies and available data using carbon fiber as a reinforcement. Because of this, the area of review will be broadened to include other reinforcement materials and fiber types.

There have been various nanosized reinforcements studied as a method of increasing the material properties of SLA manufactured parts such as: cellulose nanocrystals (CNC), multi-wall carbon nanotubes (MWCNTs), and silver nanoparticles (AgNPs) [25-27, 31]. Feng X. et al [27] used lignin-coated cellulose nanocrystals (L-CNC) at 0, 0.1, 0.5, and 1 weight percent with an acrylic matrix. The research was carried out using Form+1 (Formlabs, Somerville, MA) which is a bottom-up desktop SLA printer. At a loading of 0.5 wt.% L-CNC there was an increase in the tensile strength and Young's modulus by 3% and 5% respectively [27]. This was achieved only after a thermal post-cure being carried out on the specimens with the non-post cured specimens showing unimproved or reduced properties depending on the loading of L-CNC [27]. The

decrease in material properties that was seen at higher weight percent was attributed to poor dispersion of the L-CNC and poor adhesion between the L-CNC and matrix [27].

Sandoval et al. [25] investigated a composite made from MWCNTs at 0.025 and 0.1 weight percent with an epoxy-based matrix using the commercial resin, DSM Somos® WaterShed™ 11120. A top-down printer the 3D Systems SLA-250/50 machine (3D Systems, Rock Hill, SC) was modified from a 47 liter vat to a 500 ml vat with the sweeping mechanism removed, and a peristaltic pump was used to recirculate the resin mixture [25]. The research looked at the increasing the tensile strength and fracture strength of the resin. For 0.025 wt.% of MWCNTs, an increase in tensile strength of 5.7% with an increase in fracture strength of 26% was reported. While at 0.10 wt.% an increase of 7.5% and 33% in tensile and fracture strength, respectively was reported, but it was pointed out that at the higher loading of 0.1% MWCNTs there were issues with agglomeration of the MWCNTs [25]. The elongation at break decreased 28% for the MWCNTs reinforced resin, and the fracture mode was reported as a brittle type verse as more of a ductile failure mode that was seen in the pure resin [25].

Short glass fibers have been studied more as reinforcement materials for SLA in part due to the decrease in opacity when compared to that of carbon fiber [4]. In one study, Cheah, C. et al. [32] looked at using short glass fibers 1.6 mm in length at various fiber volume fractions of 0, 5, 10, 15, and 20 percent, and an urethane acrylic matrix, DeSolite SCR310. The experiment was carried out for comparing molded and 3D printed samples. Although the paper does not state what machine was used to print the samples it can be inferred that a top-down style was used [32]. Cheah, C. et al saw improvements for all fiber volumes, with increased mechanical properties achieved by increasing fiber amount and part shrinkage can be reduced. For a fiber volume of 20% they were able to achieve an increase in tensile strength of 24%, and an 80%

increase in the Young's modulus [32]. The top-down SLA machine that was employed resulted in the manufacture of composites that were close to unidirectional in fiber orientation due to the scraping step in between layers [32]. While the creation of unidirectional composites is desirable in some applications, the leveling step would prevent the printing of an isotropic part, and therefore could limit potential applications and restrict the printing process based on how the part must be printed.

Along with short glass fibers, there have also be studies that have looked into the use of continuous glass fiber as a reinforcement in SLA. Karalekas D. et al. [3] placed a single layer of nonwoven glass fiber mats, of various thickness, within specimens produced using SLA. This was done by pausing the printer at a predetermined build height placing the mat of the specimen and resuming the print [3]. Karalekas D. et al. were able to show an increase in the Young's modulus, but a decrease in tensile strength for thinner mats. For the thicker mats the Young's modulus was shown to decrease, this was contributed to the inability for the photopolymer to fully cure with in the thicker mats [3]. While this study was able to show that continuous glass fibers could be placed into the part for reinforcement, the fact that it was added by hand during the build process is inefficient, especially if multiple layers of fiber are to be used in the manufacturing of a part, and would be difficult for the manufacturing of complex parts.

There is limited literature available on the use of carbon fibers with SLA, this could be due in part to the limitation of carbon fibers being opaque [2, 4, 29]. Some research has been carried out in this area using continuous carbon fiber by Gupta A. et al. [30] where to overcome the issues of fully curing the part a dual curing system was used. The dual curing system employed a photo initiator for initially curing the fiber and matrix in the desired geometry, and a thermal initiator to cure the remaining resin. While Gupta A. et al was able to show that the

system was fully cured, they did not report any information on the material properties of the composite produced [30].

2.4. Dual Cure Resin System

The use of a dual cure resin system, as proposed by Gupta A. et al [30], shows promise a method of fully curing a short fiber composite manufactured using SLA, and this is demonstrated in latter sections 5.1 and 5.2. The ability for the thermal initiator to cure the areas that the UV light cannot, due to the opacity of the carbon fiber, could prove to be an effective method in the manufacturing of short fiber composite via STL, shown in Figure 2.3.

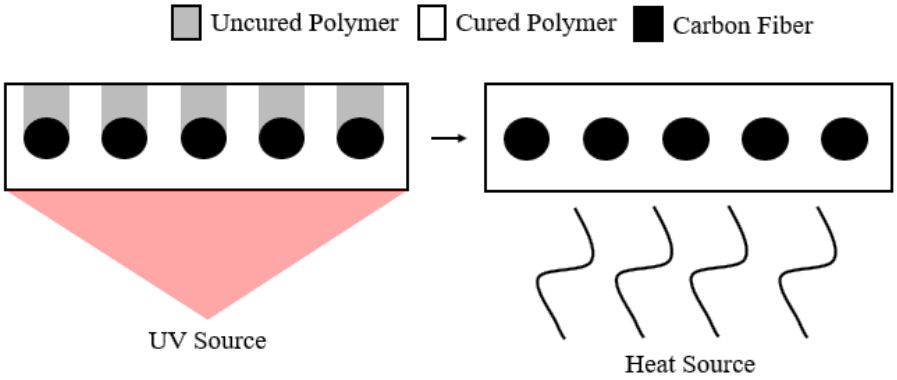

Figure 2.3: Dual curing system.

3. OBJECTIVES

From the available literature in section 2.3, there is a limited amount of information and results in the development of short-fiber composite manufactured using SLA, in particular ones that use carbon fiber as the reinforcing material. The brittle nature of acrylic leads to a low fracture toughness, and therefore, a low facture toughness in the parts made using SLA printing [34, 35]. By incorporating fibers into the acrylic polymer, the fracture toughness could be increased, along with other mechanical properties such as tensile strength and Young's modulus [13, 22, 32, 36, 37]. By taking advantage of the layer-by-layer manufacturing process it could be possible to produce either an isotropic material, or an orthotropic material by influencing the fiber orientation during the fabrication process by taking advantage of the differences in fiber length verses layer height, as shown in Figure 3.1.

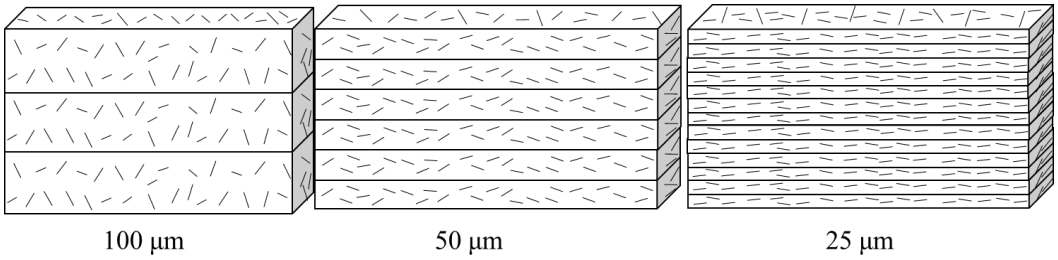

Figure 3.1: Effects of layer height on fiber orientation.

The purpose of this research will primarily be aimed at increasing the mechanical properties of parts manufactured using SLA with fiber reinforcement. To accomplish this, the research objectives are be defined as:

- Determine and develop the processing parameters needed to manufacture short fiber composite using SLA with carbon fiber as a reinforcement
- Evaluate the effect of print orientation on material properties
- Evaluate the effect of layer height on material properties

4. RESEARCH METHODOLOGY

This section will detail the materials and equipment used, the methods for sample manufacturing, testing, and data analysis for this research. The section is organized into three different main sub-sections, materials and equipment, sample manufacturing, and material characterization. The materials and equipment section will look at the base materials and the SLA printer used for this research. The section on sample manufacturing will cover the steps used to produce the samples used in this study. While the material characterization section will discuss the testing methods and data analysis used for characterization of the samples.

4.1. Materials and Equipment

The following subsections will detail the materials and SLA printer that were used to produce both short-fiber composites, and the controls used in this study.

4.1.1. Moai Printer

A Moai Laser SLA Printer manufactured by Peopoly, and purchased from MatterHackers, (Lake Forest, CA) as a DIY kit, was assembled and calibrated by the author. The Moai is a bottom-up printer that uses a 405 nm 70-micron spot size laser and is based on an open sourced design. This allows for the modification of both hardware and software along with direct G-Code modification, with the limitation of the firmware being closed source. All printing settings used in the research are in reference to the Moai printer using firmware version 1.6. Figure 4.1 is of the Moai printer currently being used to conduct this study.

Figure 4.1: Moai SLA printer.

4.1.2. Photopolymer Resins

The photopolymer resin being used in this research is Moai Standard Clear resin, by Peopoly. It is an acrylic-based photopolymer designed to work with the Moai printer being used in this research. The data in Table 4.1 shows the given makeup of the resin according to the manufacture.

Table 4.1: Peopoly resin constituents [9].

Chemical	Approximant Weight (%)
Urethane Acrylate	30-50
Acrylic Monomer	55-60
1,6 - Hexanediol Diacrylate	5-15
Photo initiator	0-5

4.1.3. Carbon Fiber

Carbon fiber has been used as a reinforcement in polymer matrix composite for many years [38]. This material is widely used for its high strength, modulus, and thermal resistance

along with its light weight. The high specific properties lead to carbon fiber composites being used in a number of industries such as, aerospace, automotive, sports, aeronautics, and leisure [39, 40]. The exact mechanical properties of carbon fiber can vary depending on the precursors used and the processing parameters during its manufacturing. Table 4.2 shows the mechanical properties of some carbon fibers depending on what precursors are used in their manufacturing [41].

Table 4.2: Mechanical properties of various carbon fiber [41].

Precursor	Tensile Strength (GPa)	Tensile Modulus (GPa)
Polyacrylonitrile (PAN)	2.5-7.0	250-400
Mesophase Pitch	1.5-3.5	200-800
Rayon	1.0	50

The primary carbon fiber that will be used in this study will be, Toray T-700. The fiber was purchased form Composite Envisions (Wausau, WI) as a chopped 3 mm fiber and is sized for epoxies. The fiber was then milled in a Retsch Rotor Beater Mill SR 300 (Retsch GmbH, Haan, Germany) using a 120 µm screen. The milled fiber was then sieved using a stack of screens, with a stacking sequence of 2 mm, 250 µm, 106 µm, and 76 µm. The fibers were collected in-between the 106 µm and 76 µm screens.

To evaluate the size of the milled carbon fiber produce, a glass slide was prepared that was coated with a thin layer of the Moai resin. A sample of fibers was then applied on the surface of the glass slide, and held in front of the light in the UV cure oven for 1 minute. A sample of fibers were observed using an Axovert 40Mat (Carl Zeiss AG, Oberkochen, Germany), with images obtained by a ProgRes C10plus camera (Jenoptik AG, Jena, Germany), to determine the average length along with the length distribution. The processed fibers were then placed in an oven at 80 °C and dried for a minimum of 8 hours before use. The mechanical properties of the fibers as provided by the manufacturer are shown in Table 4.3.

Table 4.3: Toray T-700 fiber properties [42].

T-700 Fiber Properties	
Fiber Diameter	7 µm
Fiber Length	3 mm
Tensile Strength	4.90 GPa
Tensile Modulus	230 GPa

A second fiber was also used during this research, Carbiso MF SM45R-100 manufactured by ELG Carbon Fibre Ltd, (Conseley, UK). The fibers are reclaimed from end-of-life composite materials that are then take through a modified pyrolysis process, milled, and sorted [43]. The fibers that were used were dried for a minimum of 8 hours in an oven at 80°C. Due to the reclamation process the fiber is unsized, and has the mechanical properties, as provided by the manufacturer, shown in Table 4.4.

Table 4.4: Carbiso MF SM45R-100 fiber properties [43].

Carbiso MF Fiber Properties	
Fiber Diameter	7 µm
Fiber Length	80-100 µm
Tensile Strength	4.150 GPa
Tensile Modulus	230-255 GPa

4.1.4. Thermal Initiators

The exact make up and composition of the base resin being used is not known, therefore a variety of thermal initiators will be investigated in order to identify the optimum thermal initiator to be used in a dual cure system. This will be based off of the thermal initiators solubility with the resin system, the stability of the resin system at room temperature, and the temperatures needed for post-curing of the samples. The initial thermal initiators to be investigated are summarized in Table 4.5.

Table 4.5 Thermal initiators to be investigated for a dual cure resin system.

Name	Trade Name	CAS Number	Source
Dilauroyl Peroxide	Luperox LP	105-74-8	Alfa Aesar
Cumene Hydroperoxide	--	80-15-9	Sigma-Aldrich
Dicumyl Peroxide	--	80-43-3	Sigma-Aldrich
Tert-Butyl Peroxybenzoate	Luperox P	614-45-9	Sigma-Aldrich
Benzoyl Peroxide	Luperox A98	94-36-0	Alfa Aesar

4.2. Sample Manufacturing

The following subsections will detail the processing parameters that will be used to produce both short-fiber composites, and the controls that will be used in this study.

4.2.1. Resin Manufacturing

To ensure that the fiber and any other added components are well dispersed the following process was carried out:

1. The necessary fiber amount is added to the resin and hand mixed for 2 minutes.
2. The resin mixture is then mixed using a high-speed mixer for 20 minutes.
3. The resin mixture is then placed in an ice bath and sonicated in 10 second pluses, with a 1 minute break between pulses, for a total of 5 minutes of sonication.
4. The necessary thermal initiator amount is then added.
5. The resin mixture is then mixed in a high-speed mixer for 20 minutes.
6. The resin mixture is then degassed in a vacuum chamber for 10 minutes, or until bubbling stops.

The resin and fiber was first mixed and sonicated separately, due to the increase in temperature of the resin during this process, as a way of protecting the thermal initiator. The vacuum chamber is used to remove any air trapped within the system that could then cause voids within the manufactured sample. Upon the completion of the degassing the resin is immediately used to manufacture samples to limit the time allowed for setting of the fiber to occur.

4.2.2. Processing Parameters for 3D Printing Parts

To create samples for testing, the test samples were designed first using SolidWorks (Dassault Group, Paris, France), a CAD software, to create the need geometry of the specimens. The files were then exported from Solidworks in a Standard Tessellation Language (stl) file format. The stl files are then loaded into another software package, XYZware (New Kinpo Group, New Taipei City, Taiwan) that is used to orient the part in the desired print orientation, and used to generate the necessary supports to facilitate the printing process. XYZware was used to generate all supports and part orientations for this research. The supports that are made within XYZware serve multiple purposes such as elevating the part above and securing it to the print bed. The silicon layer that is coated along the bottom of the vat is deformed when the bed is initially lowered. The part to be printed is raised up from the print bed by these supports a sufficient distance, generally 3 to 6 mm, to allow for compensation due to the compression of the silicon layer so as to not affect the geometry of the part being printed.

Generally, when printing with bottom-up style machines the part is oriented to reduce the size of the cross-section of the largest axis of the part. This is done to reduce the stresses within the part when the peel step is carried out. If too high of stresses are present it can result in layer separation, warping of the part, or separation/shifting from the printing bed. To be able to print the parts need for this research it was necessary to the increase the amount and size of some of the supports used. An example of the supports applied in the XYZware software is shown in Figure 4.2.

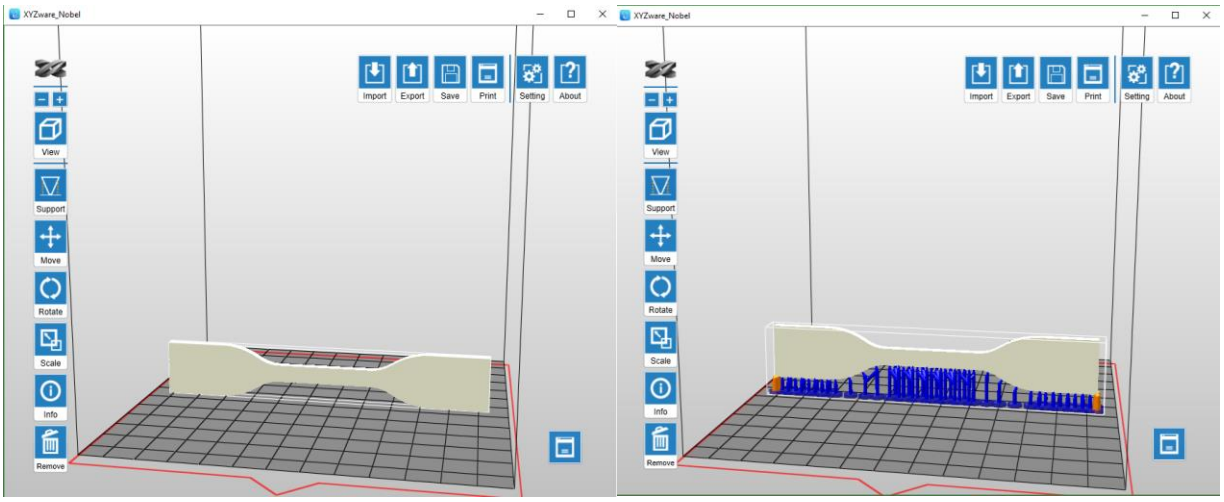

Figure 4.2: Before (left) and after (right) support material being added.

The modified stl file is then exported and used in Cura 3.2 Moai Edition (Ultimaker, Geldermalsen, Netherlands) to generate the gcode that is used for running the printer. The Cura software is an open-source 3D printing software that was originally developed for the use in FDM printers. The Moai Edition of this software allows for its use in SLA type printers and was used for all gcode file creation in this research. An example of the Moai Cura software's interface is shown in Figure 4.3.

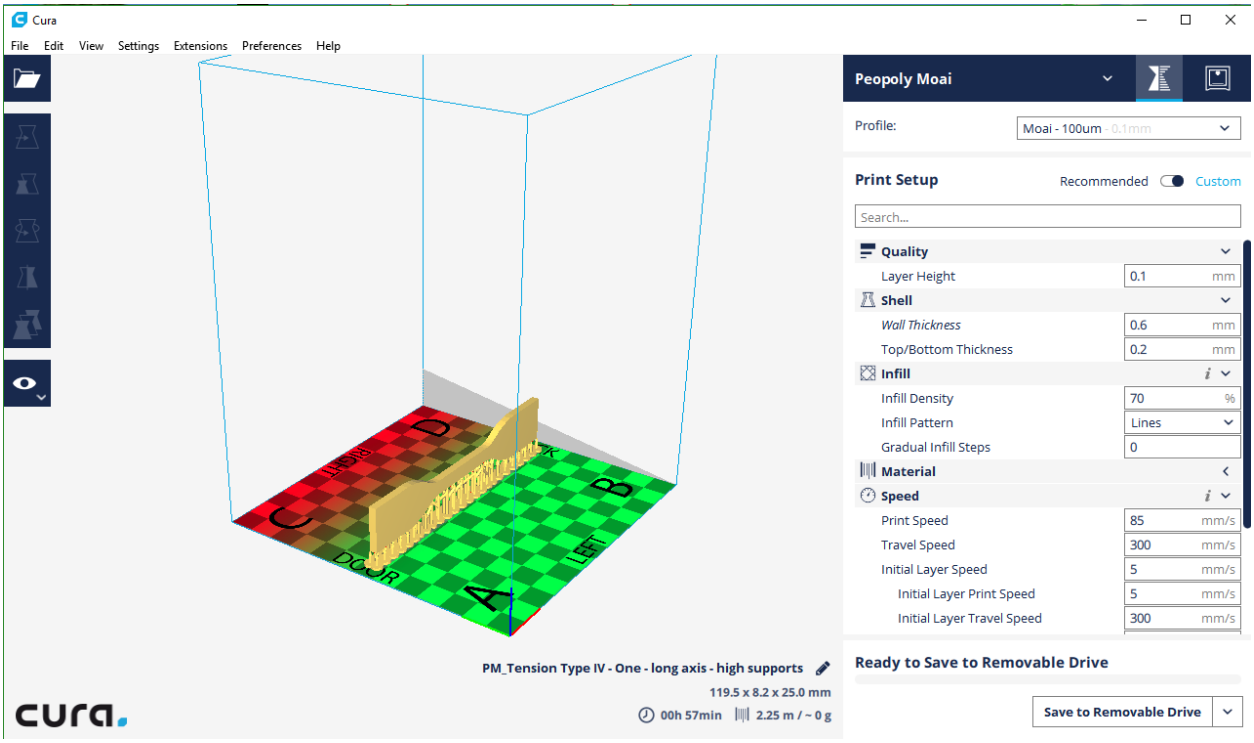

Figure 4.3: Cura slicing software.

Within the Cura software is where the modifications to the printing parameters can be made. The most important of these would be the layer height, laser speed, and infill amount. For samples printed with neat (non-fiber reinforced) resin, the layer height would have the most effect on the print resolution when trying to print fine/small details. For the application in printing short-fiber composites it is proposed that the layer height can be used to influence the fiber orientation.

The laser speed, along with the laser power which is set directly on the printer, controls the amount of energy being delivered to the area, and therefore directly effects the curing of the part being printed [5]. The infill amount is used to control the amount of space between the laser scans within the part, if any that occurs during the printing process. The infill patterns can also be change, but only the line pattern was used for this research. While the laser spot is where the energy is being delivered to initiate the polymerization, there is an area around the laser spot that

the polymerization process spreads past [5]. This allows for the spacing between the scan lines, but stills allows for curing of part into a solid. By increasing the space between the scans the print time can be reduced, but if the spacing is increased too much the part can fail to fully cure and as a result a solid part will not be formed.

For all samples that are manufactured using the 3D printer for this research a naming convention will be implemented that will reference the long axis of the sample to the printed layer orientation, this is illustrated in Figure 4.4.

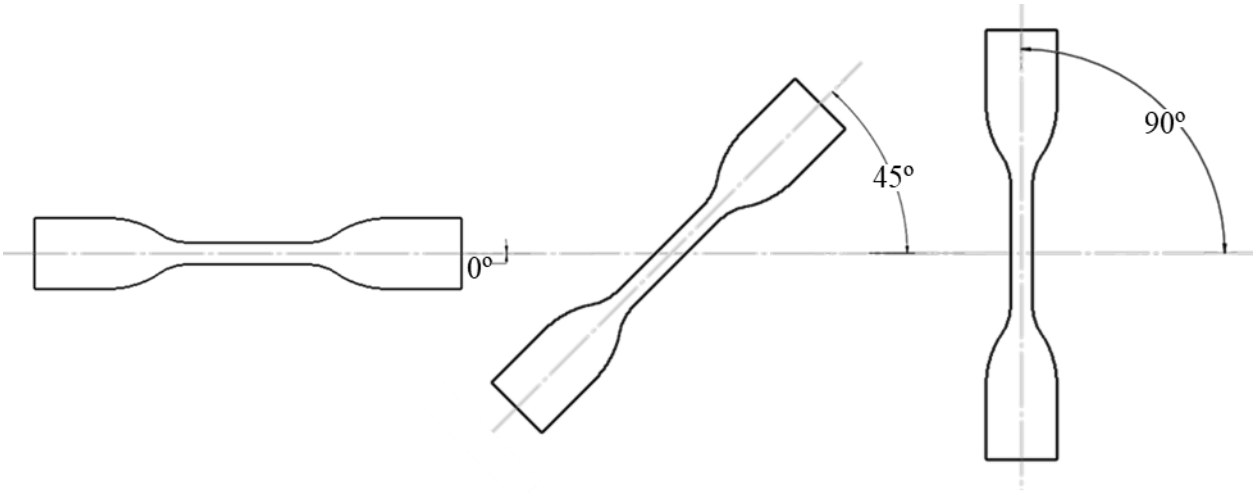

Figure 4.4: Sample long axis orientation.

4.2.3. Post-Processing of 3D Printed Parts

For all samples prepared, the finished parts were washed in ethanol after being removed from the build platform. This allows for the removal of any uncured resin, and in the case of the fiber reinforced samples any lose fibers from the surface. The supports that were generated during the printing process are left in place at this time to support the sample while it was being post-cured.

For the neat (non-fiber reinforced) samples, the resin manufacturer recommends post-curing in a 405 nm UV light for a period of time until the surface cannot be scratched by a finger

nail [9]. While other resin manufactures provide more detailed post-curing instructions of elevated temperature and times. For this research the neat samples were post-cured in an in-house built cure oven, shown in Figure 4.5.

Figure 4.5: UV cure oven.

This oven consist of three 25 Watt LED UV lights, a heating element, and a rotating platform. The temperature and the time for the post-cure can be adjusted by the use of PID controller. For the neat samples a temperature of 80 °C was used while being exposed to the UV light for 1 hour.

Unless otherwise stated the fiber reinforced sample's post-curing was carried out using a VWR Forced Convection Oven (VWR International, Radnor, PA), shown in Figure 4.6.

Figure 4.6: Post-curing oven.

The temperature that the samples are post-cured at will be dependent on the thermal initiator that is used, with DSC being used to determine at what temperature the resin system will begin to initiate, and how long the samples will need to be held at that temperature.

After post-curing is complete, the supports are removed from the sample. This leaves behind dimples in the surface that can act as defects that affect the ultimate tensile strength of the material during testing [44]. An example of these surface defects are shown in Figure 4.7.

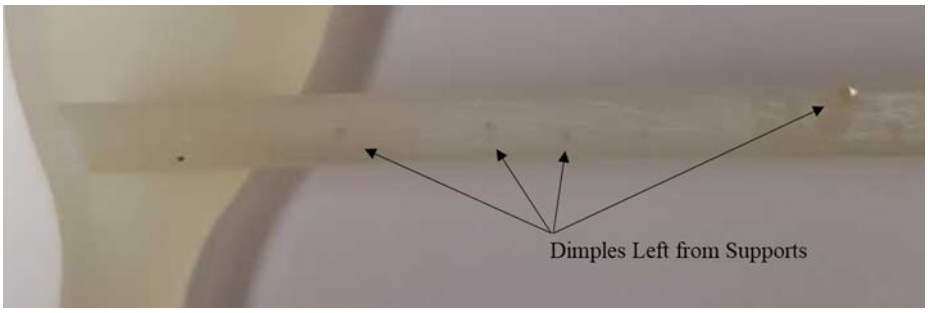

Figure 4.7: Surface defects from support removal.

To completely remove the dimples, the area that had the supports attached were sanded with increasingly finer grits of sand paper, ranging from 60 to 600, with care taken to preserve the sample geometry which varies depending on the desired testing. This was done for all printed samples used in this study. Figure 4.8 shows the progression at various points in removing the support material and surface defects.

Figure 4.8: Removal of supports and surface effects. A) Supports removed, B) sanded with 60 grit paper, and C) sanded with 600 grit paper

4.3. Material Property Characterization of 3D Printed Composites

The following subsections will detail the material characterization that was used to experimentally evaluate both short-fiber composites and the controls that were used in this study.

4.3.1. Thermal Initiator Selection

In an effort to identify a thermal initiator that worked best as a dual cure system, several were evaluated with the first key issue being the solubility of the initiator within the resin. As mentioned in section 2.3.2, Gupta A. et al [30] proposed a dual cure system using Luperox LP that remained in a solid state in the sample until post-curing at an elevated temperature. To achieve a good dispersion of the initiator within the system different thermal initiators were mixed at a loading of 1 wt.% with the resin. The mixtures were monitored to determine if the

initiator was soluble in the resin, and also monitored for one week at room temperature to insure stability for the 3D printing process.

Upon completion of solubility testing the selected thermal initiators were evaluated experimentally via differential scanning calorimetry (DSC) in accordance with ASTM E2160 [45]. The testing was carried out over a range from 25°C to 180°C at a ramp rate of 10°C/min, using a Q20 DSC (TA Instruments, New Castle, DE). This was done to determine the thermal initiators onset temperature, and to experimentally determine if any reactions are occurring after UV curing. The samples were tested at a fiber volume (V_f) of 5%, and a thermal initiator content of 1 wt.% of thermal initiator to 99 wt.% of Moai resin. The neat Moai resin was also tested to determine if there is any activation of the photo initiator at elevated temperatures.

For each sample tested two runs were carried out. The first was of an uncured sample, and the second was a sample that had been UV cured by placing the DSC pan in the UV cure oven 25.4 mm away from the light source for one minute at room temperature. All graphs produced from the DSC data were made using TA Universal Analysis (TA Instruments, New Castle, DE).

4.3.2. Viscosity Testing

To examine both the effects of the fiber reinforcement and thermal initiator on the resin system, viscosity testing was carried out using a AR-G2 Rheometer (TA Instruments, New Castle, DE) with a 40 mm steel parallel plate and Peltier plate, shown in Figure 4.9.

Figure 4.9: AR-G2 rheometer.

The gap between the plates was set to 1000 μm to allow for at least 10 times the length of the fiber (assumed a fiber length of 100 μm) in the resin, as per the AR-G2 TA Instruments rheology manual [46]. Two controlled shear rate test were ran for each sample, one from a range of 1 to 25 s^{-1} on a linear scale with 25 sample points, and the other from 1 to 100 s^{-1} on a log scale at 5 decades. All test were carried out at room temperature, and the data was post processed using Rheology Advantage Data Analysis (TA Instruments, New Castle, DE).

The experimental data points where then fitted with a model that resulted in the smallest standard error. This was found to be Ostwald-de-Waele equation (power law equation) for both of the testing rates, shown in Equation 4.1,

$$\tau = \bar{K}\dot{\gamma}^{n}, \tag{4.1}$$

were, τ is the shear stress, $\dot{\gamma}$ is the shear rate, n is the power-law index, and $\overline{K}$ is the consistency index of the polymer [47]. The best fit was determined based off of the standard error of model with the smaller number being the best fit and defined as Equation 4.2,

$$SE = \frac{\left[\frac{\sum(x_m - x_c)^2}{n-2}\right]^{1/2}}{Range} x1000, \tag{4.2}$$

where X_m is the measured value, X_C is the calculated value of x for each data point, n is the number of data points, and the range is the maximum value of X_m [46, 47].

4.3.3. Tensile Testing

4.3.3.1. Sample Manufacturing and Testing

The tensile testing was carried out using an Instron 5567 load frame (Instron, Norwood, MA), a 25.4 mm extensometer, and a 2 kN load cell. The load frame was controlled and data collected using Bluehill software (Instron, Norwood, MA). While there are no ASTMs directly concerning 3D printed materials, all tensile testing will be carried out referencing ASTM D638 [48] and ASTM 3039 [49]. The specimen geometry was of the type IV according to ASTM D638, with the specimen dimensions shown in Figure 4.10 [48].

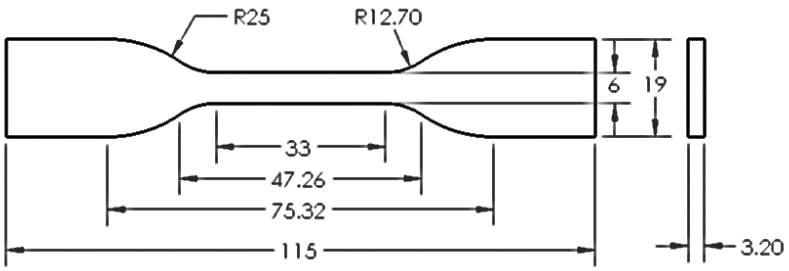

Figure 4.10: Tensile testing specimen (all dimensions in mm).

The type IV specimen was chosen due to the limiting size of the build plate (130 mm x 130 mm) of the Moai printer being used to conduct this research. All samples were tested at a

constant cross-head rate of 1 mm/min, so failure of the specimen occurred within 1 to 10 minutes of testing, per ASTM D3039 [49]. For each sample 5 specimens were tested.

To evaluate the effect of using SLA to manufacture short-fiber composites the sample parameters that were evaluated are; carbon fiber reinforcement, thermal initiator effects, different layer heights, and different print orientations. So as to determine what effect the different manufacturing parameters and fiber volumes have on the Young's modulus and ultimate tensile strength. To develop the experiment a two level full factorial design was used with the above mentioned parameters. Table 4.6 shows the identification of each factor, while Table 4.7 is the experimental test matrix.

Table 4.6: Tensile testing experimental variables.

Factor	Level 1	Level 2
Print Orientation	0°	90°
Layer Height	100 µm	50 µm
Fiber Volume	0	5% V_f
Thermal Initiator	0	0.5 wt%

Table 4.7: Tensile testing test matrix.

Test Number	Print Orientation	Layer Height	Fiber Volume	Thermal Initiator
1	1	1	1	1
2	1	1	1	2
3	1	1	2	1
4	1	1	2	2
5	1	2	1	1
6	1	2	1	2
7	1	2	2	1
8	1	2	2	2
9	2	1	1	1
10	2	1	1	2
11	2	1	2	1
12	2	1	2	2
13	2	2	1	1
14	2	2	1	2
15	2	2	2	1
16	2	2	2	2

4.3.3.2. Data Analysis

The experimental data was evaluated statistically to identify any trends using MatLab R2016b (MathWorks, Natick, MA), and Excel (Microsoft, Redmond, WA). The effects of layer high and print orientation were compared using a one-way ANOVA analyst at a 95% confidence interval. While ANOVA allows for the identification if there is a difference between the means within a group it will not identify which groups are different [50]. To identify which samples differ from each other additional statistical analysis was carried out. Tukey's Honest Significant Difference (HSD) was chosen to identify which samples differ from each other within the groups compared using ANOVA. The Tukey HSD is calculated by first applying Equation 4.3.

$$Q_{HSD} = \frac{M_i - M_j}{\sqrt{\frac{MS_W}{n}}}, \tag{4.3}$$

where M_i and M_j are the means of the pairs to be compared, with M_i being larger then M_j, MS_W is the mean square within from the ANOVA analysis, and n is the sample size [50-52]. The Q_{HSD}

value is then compared to a $Q_{critical}$ value based off of sample size, degrees of freedom for the error term, and desired confidence level, and can be found from numerous sources as published tables [50, 51].

The Tukey test for the tension samples was carried out at both a 95% and 99% confidence level with the highest confidence level being reported per compared pair, with the corresponding $Q_{critical}$ values shown in Table 4.8 [51].

Table 4.8: $Q_{critical}$ for Tukey HSD tension testing.

Confidence Level	$Q_{critical}$
95%	4.3729
99%	5.3738

4.3.4. Flexural Testing

4.3.4.1. Sample Manufacturing and Testing

The flexural testing was carried out using an Instron 5567 load frame (Instron, Norwood, MA) with a 2 kN load cell. The load frame was controlled and data collected using Bluehill software (Instron, Norwood, MA). While there are no ASTMs directly concerning 3D printed materials, all flexural testing will be carried out referencing ASTM D790 [53]. The flexural testing was carried out as a three-point bending utilizing center loading, with specimens having a span-to-thickness ratio of 16:1. The crosshead rate for testing was determine using Equation 4.4, as per ASTM D790.

$$R = \frac{ZL^2}{6d} \tag{4.4}$$

where R is the crosshead rate, Z is the rate of straining of the outer fiber (0.01), L is the support span, d is the depth of the beam [53]. The specimen geometry was determined based off of ASTM D790 so as to fit within the build envelope of the printer, with the specimen dimensions shown in Figure 4.10 [53].

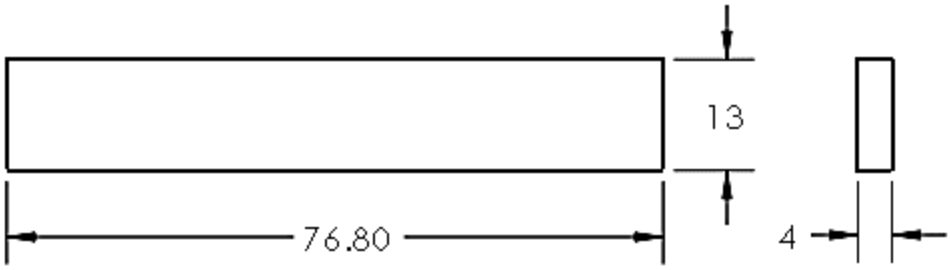

Figure 4.11: Flexural testing specimen (all dimensions in mm).

To evaluate the effect of using SLA to manufacture short-fiber composites samples were tested at, different fiber volumes, different layer heights, and print orientations so as to determine what effect the different manufacturing parameters and fiber volumes had on the flexural strength and stiffness. To develop the experiment a two level full factorial design was used with the above mentioned parameters. Table 4.9 shows the identification of each factor, while Table 4.10 is the experimental test matrix.

Table 4.9: Flexural testing experimental variables.

Factor	Level 1	Level 2
Print Orientation	0°	90°
Layer Height	100 µm	50 µm
Fiber Volume	0	5% V_f
Thermal Initiator	0	0.5 wt%

Table 4.10: Flexural testing test matrix.

Test Number	Print Orientation	Layer Height	Fiber Volume	Thermal Initiator
1	1	1	1	1
2	1	1	1	2
3	1	1	2	1
4	1	1	2	2
5	1	2	1	1
6	1	2	1	2
7	1	2	2	1
8	1	2	2	2
9	2	1	1	1
10	2	1	1	2
11	2	1	2	1
12	2	1	2	2
13	2	2	1	1
14	2	2	1	2
15	2	2	2	1
16	2	2	2	2

4.3.4.2. Data Analysis

The data analysis for the flexural testing was carried out in the same manner as the tensile testing, as described in section 4.3.3.2. The same parameters for the $Q_{critical}$ that were used for the tensile testing were used for the flexural testing due to the same sample size.

4.3.5. Fracture Toughness Testing

4.3.5.1. Sample Manufacturing and Testing

The fracture toughness testing was carried out using an Instron 5567 load frame (Instron, Norwood, MA) with a 2 kN load cell. The load frame was controlled and data collected using Bluehill software (Instron, Norwood, MA). While there are no ASTMs directly concerning 3D printed materials, all fracture toughness testing was carried out referencing ASTM D5045 [54]. The testing was conducted using the three point bend method that utilizes a single edge notched beam (SENB) specimen [54]. To find the necessary specimen geometry ASTM E399 [55] was referenced to find the minimum recommended thickness based off the ratio of yield strength to

Young's modulus. Based off of ASTM D5045 and the printer bed size a thickness, *B*, was chosen as 7 mm. The other dimensions of the specimen are then based off of this value to insure plane-strain conditions and are shown in Figure 4.12 [54].

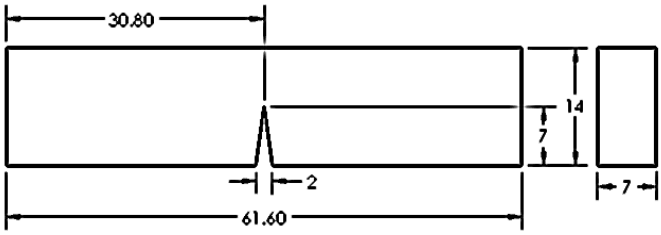

Figure 4.12: SENB specimen for fracture testing (all dimensions in mm).

As per ASTM D5045, a natural crack was generated by sliding a razor blade in the 3D printed notch until the crack was of the specified length [54]. The fracture toughness was then calculated per section A1.4 of ASTM D5045 [54].

To evaluate the effect of using SLA to manufacture short-fiber composites samples were tested at different fiber volumes, different layer heights, and print orientations so as to determine what effect the different manufacturing parameters and fiber volumes had on the fracture toughness. To develop the experiment a two level full factorial design was used with the above mentioned parameters Table 4.11 shows the identification of each factor, while Table 4.12 is the experimental test matrix.

Table 4.11: Fracture toughness testing experimental variables.

Factor	Level 1	Level 2
Print Orientation	0°	90°
Layer Height	100 µm	50 µm
Fiber Volume	0	5% V_f
Thermal Initiator	0	0.5 wt%

Table 4.12: Fracture toughness testing test matrix.

Test Number	Print Orientation	Layer Height	Fiber Volume	Thermal Initiator
1	1	1	1	1
2	1	1	1	2
3	1	1	2	1
4	1	1	2	2
5	1	2	1	1
6	1	2	1	2
7	1	2	2	1
8	1	2	2	2
9	2	1	1	1
10	2	1	1	2
11	2	1	2	1
12	2	1	2	2
13	2	2	1	1
14	2	2	1	2
15	2	2	2	1
16	2	2	2	2

4.3.5.2. Data Analysis

The data analysis for the flexural testing was carried out in the same manner as the tensile testing, as described in section 4.3.3.2. With $Q_{critical}$ values due to the different sample size shown in Table 4.13 [51].

Table 4.13: Qcritical for Tukey HSD fracture toughness testing.

Confidence Level	$Q_{critical}$
95%	4.7511
99%	6.1023

4.3.6. Fiber Volume Consistency

To evaluate the consistency of the fiber volume content, due to the various printing times need in manufacturing samples, burn off testing was carried out. The samples that were analyzed were taken at 3 different points from flexural specimens printed in the 90° print orientation as 2 mm sections, as shown in Figure 4.13.

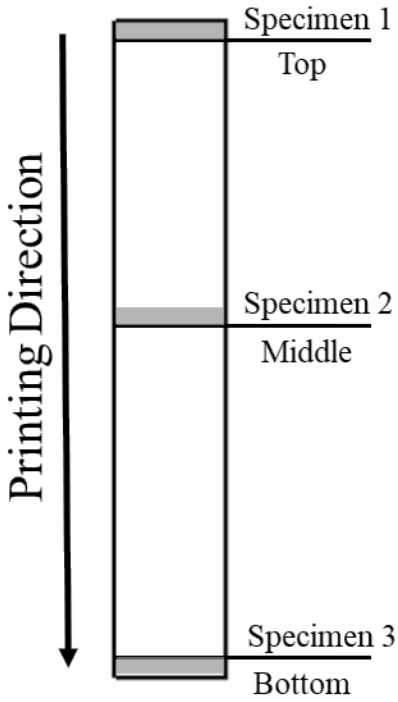

Figure 4.13: Burn off sample testing areas.

The testing was carried out using a Thermolyne Type 2000 muffle furnace (Thermolyne, Dubuque, IA), pictured in Figure 4.14.

Figure 4.14: Thermolyne muffle furnace.

The burn off testing was carried out referencing ASTM D3171-15 procedure G, with the samples being held at a temperature of 550 ºC for 1 hour [56]. Two specimens each were tested for the two different layer heights to determine at what point, if any, the print times start to effect the fiber content due to settling. The print times for the 100 μm and 50 μm layer heights were 3.00 and 5.25 hours, respectively.

4.3.7. Composite Void Content

To determine the void content of the carbon fiber composites, first the density was found as per ASTM D792-13 Test Method A [57]. Cubes were printed of 0.5 wt.% Luperox P at 100 μm layer height, and for 100 μm and 50 μm layer height for resin containing 5% V_f carbon fiber and 0.5%wt Luperox P. All samples were prepared and post-cured as outlined in section 4.2. The specimen geometry used is shown in Figure 4.15.

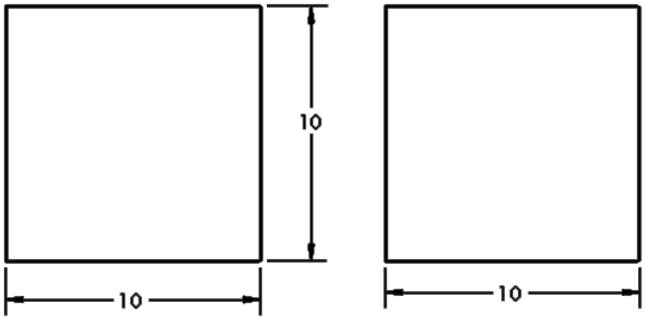

Figure 4.15: Void content and density test specimen (all dimensions mm).

The water temperature at the time of testing was 23.7 ºC, and the density was found per section 13.1 and 13.2 of ASTM D792-13 [57]. Two specimens were tested per sample and the same composite samples that were used to find the density were then used to determine the void content as per ASTM D3171-15 Procedure G [56]. The burn off testing was carried out using the same Thermolyne Type 2000 muffle furnace that was used in section 4.3.6. Two specimens per sample were tested with a burn off time of 1.5 hours at 550 ºC.

4.3.8. Post-Cure Shrinkage

To determine the shrinkage that occurred during the post-curing process samples were prepared of the same geometry used for the density measurements, shown in Figure 4.15. For the testing 5 specimens per sample were prepared and evaluated. The samples that were tested are shown in Table 4.14.

Table 4.14: Post-cure shrinkage test samples.

Sample Constituents	Layer Height
Moai Resin	100
Moai Resin	50
Moai Resin + 0.5 wt.% Luperox P	100
Moai Resin + 0.5 wt.% Luperox P	50
Moai Resin + 0.5 wt.% Luperox P + 5% V_f Carbon Fiber	100
Moai Resin + 0.5 wt.% Luperox P + 5% V_f Carbon Fiber	50

The samples were prepared as per sections 4.2.1 and 4.2.2, and the cubes numbered for easy identification. The sides of the cubes were marked with an X, Y, and Z in reference to the printing axis defined by the Moai printer. The sides were measured using a digital caliper before post-curing. The samples were then post-cured as per section 4.2.3, and measured again. The difference in the corresponding sides and the overall volume difference was then calculated along with the mean and standard deviation.

4.3.9. Scanning Electron Microscopy

Scanning electron microscopy (SEM) will be utilized to examine the fracture surface of tested samples. This will allow for examination of the fracture surface in determining failure types, and to evaluate the dispersion and the orientation of the fibers with in the sample [58]. Samples were attached to cylindrical aluminum mounts with colloidal silver paste (SPI Supplies, West Chester, Pennsylvania, USA). The specimens were sputter coated (Cressington 108auto, Ted Pella, Redding, California, USA) with a conductive layer of gold. Images were obtained with a JEOL JSM-6490LV scanning electron microscope (JEOL USA, Inc., Peabody MA, USA); energy-dispersive X-ray information was collected at an accelerating voltage of 15 kV using a Thermo Scientific UltraDry Premium silicon drift detector with NORVAR light element window and Noran System Six imaging system (ThermoFisher Scientific, Madison WI, USA).

5. RESULTS AND DISCUSSION

5.1. UV Cured Short Fiber Reinforced Composites

To evaluate the effectiveness as carbon fiber as a reinforcement in SLA printed parts it was first attempted to print parts using only the photo initiator that was present in the Moai resin. The following section 5.1.1 summarizes the results from evaluating the tensile properties of these parts.

5.1.1. Tensile Testing

A short-fiber composite resin consisting of Carbiso MF SM45R-100 carbon fiber and Moai resin, at a fiber volume of 5%, was prepared as detailed in section 4.2.1 with the exception of the addition of a thermal initiator. Tensile samples were prepared as per sections 4.2.2 and 4.2.3 with a layer height of 50 μm and 100 μm and a print orientation of 0º. Due to no thermal initiator being used, the samples were post-cured in the same manner as the neat samples in the UV oven in section 4.2.3. The tensile testing was carried out as described in section 4.3.3. Representative stress-strain curves of the neat Moai resin and 5% V_f for 100 μm and 50 μm layer heights are shown in Figure 5.1 for comparison.

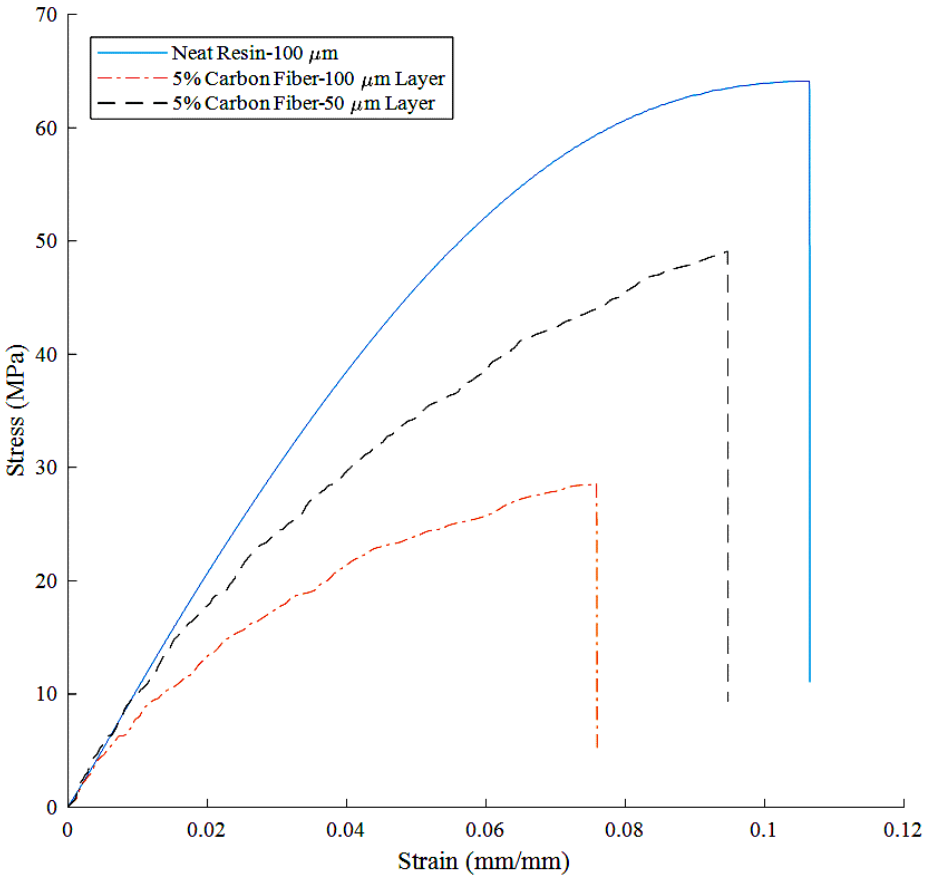

Figure 5.1: Representative stress-strain curves.

The maximum tensile strength and Young's modulus was found as specified in ASTM D638 section 11.2 and 11.4 respectively with the results summarized in Table 5.1.

Table 5.1: Tensile testing results for UV cured at 5% V_f carbon fiber.

Fiber Volume (%)	Print Orientation	Layer Height (μm)	Tensile Strength (MPa)	Young's Modulus (GPa)
0	0°	100	58.9 ± 5	2.72 ± 0.059
5	0°	100	26.2 ± 4.1	1.98 ± 0.03
5	0°	50	52.0 ± 2.3	2.64 ± 0.04

From the results in Table 5.1, the addition of the carbon fiber did not increase any of the material properties when compared to the neat Moai resin properties. Applying the Halpin-Tsai Equations (Equations 2.2 thru 2.5) to predict the Young's modulus for a randomly distributed short fiber composite, E_R, (Equation 2.6) the theoretical modulus should be 4.27 GPa.

For the sample printed at 100 µm layer height there is a decrease in both strength and modulus, while the sample printed at 50 µm layer height shows a smaller decrease. This is due to the UV radiation being unable to activate the photo initiator in order to fully cure the resin due to the opaque nature of the carbon fiber [2, 4, 29, 30]. The increase of properties between the 100 µm and 50 µm layers could be due to the fibers being aligned in the direction of the tensile testing, but is more likely due to the decreased layer height allowing for more of the matrix to be cured. This is evident by the fact that the material properties of the sample are approaching that of the neat resin. To counter act this the use of a dual cure resin system is implemented for the remainder of this research.

5.2. Dual Cured Short Fiber Reinforced Composite

5.2.1. Thermal Initiator Evaluation

5.2.1.1. Solubility and Stability of Thermal Initiators

In order to fully cure all of the resin with in the sample the use of a dual cure system that uses both a photo initiator and a thermal initiator was investigated. The first thermal initiator investigated was Luperox LP. This was chosen because of its use by Gupta A. et al [30] in a dual cure system, as mentioned in section 2.3.2. One issue that had arisen in Gupta A. et al. work and the current work is that Luperox LP is a solid at room temperature and would not completely dissolve in the base resin being used [30].

To attempt to overcome the solubility issues of the Luperox LP it was first dissolved in toluene, which was then mixed into the base resin. This addition of solvent to the resin lead to a large decrease in viscosity causing the carbon fibers to settle out of the resin quickly. To remove the toluene from the resin a vacuum chamber was used to evaporate the toluene and remove it from the resin. To verify that the toluene was removed from the resin, the weight of the resin and

thermal initiator being added was recorded along with the weight of the toluene being added. The mixture was then kept under vacuum, and the weight checked until the weight of the toluene was removed from the mixture. The other thermal initiators that were investigated, shown in Table 4.5, were either liquid or would dissolve into the Moai resin on their own, and needed no additional steps to incorporate into the system.

The solubility and stability of the thermal initiators were tested as outlined in section 4.3.1 with a 1 wt.% of thermal initiator to 99 wt.% of the Moai resin. The results of the solubility and stability testing are summarized in Table 5.2.

Table 5.2: Thermal initiator solubility and stability testing.

Thermal Initiator	Solubility	Stability
Luperox LP	Yes, with additional steps	Yes
Luperox P	Yes	Yes
Dicumyl Peroxide	Yes	Yes
Cumene Hydroperoxide	Yes	Yes
Luperox A98	Yes	No, gelled after 24 hours

Due to Luperox A98 gelling the system within 24 hours of mixing it was removed for consideration as a suitable thermal initiator.

5.2.1.2. DSC

The DSC testing was carried out as outlined in section 4.3.1 for the Moai resin and all thermal initiators but Luperox A98 and Luperox LP. The Luperox A98 was removed from the study due to gelling, and the onset temperature for the Luperox LP (93.35 °C) was available from Gupta A. et al paper [30]. The results of the DSC testing are shown in Appendix A, Figure A.1 thru Figure A.4, and are summarized below in Table 5.3.

Table 5.3: Thermal initiator onset temperature from DSC curves.

Thermal Initiator	Onset Temperature (°C)	10 Hour Half-life (ºC) [59]
Luperox P	115.99	104
Dicumyl Peroxide	116.83	114
Cumene Hydroperoxide	104.01	135

Based off of the results from the thermal initiator testing Luperox P was chosen as the first thermal initiator to be evaluated for the dual cure resin system. Luperox is a liquid at room temperature therefore it does not require additional processes to incorporate into the resin.

5.2.1.3. Resin Viscosity

To determine the effect of the incorporation of the different constituents on the viscosity of the resin it was evaluated as outlined in section 4.3.2., and tested at a room temperature of 24.5 ºC. The samples that were tested and their viscosities are shown in Table 5.4.

Table 5.4: Viscosity of composite resins.

Sample	Viscosity (Pa s)
Moai Resin	0.517
Moai Resin + 0.5% wt. Luperox P	0.497
Moai Resin + 5% Vf Carbon Fiber	0.815
Moai Resin + 5% Vf Carbon Fiber + 0.5% wt. Luperox P	0.649

With representative graphs for the testing done for a shear rate of 1 s^{-1} to 25 s^{-1} in Figure 5.2 , and for rates of 1 s^{-1} to 100 s^{-1} Figure 5.3, with the individual graphs with fitted curves in APPENDIX A, Figure A.5 thru Figure A.12.

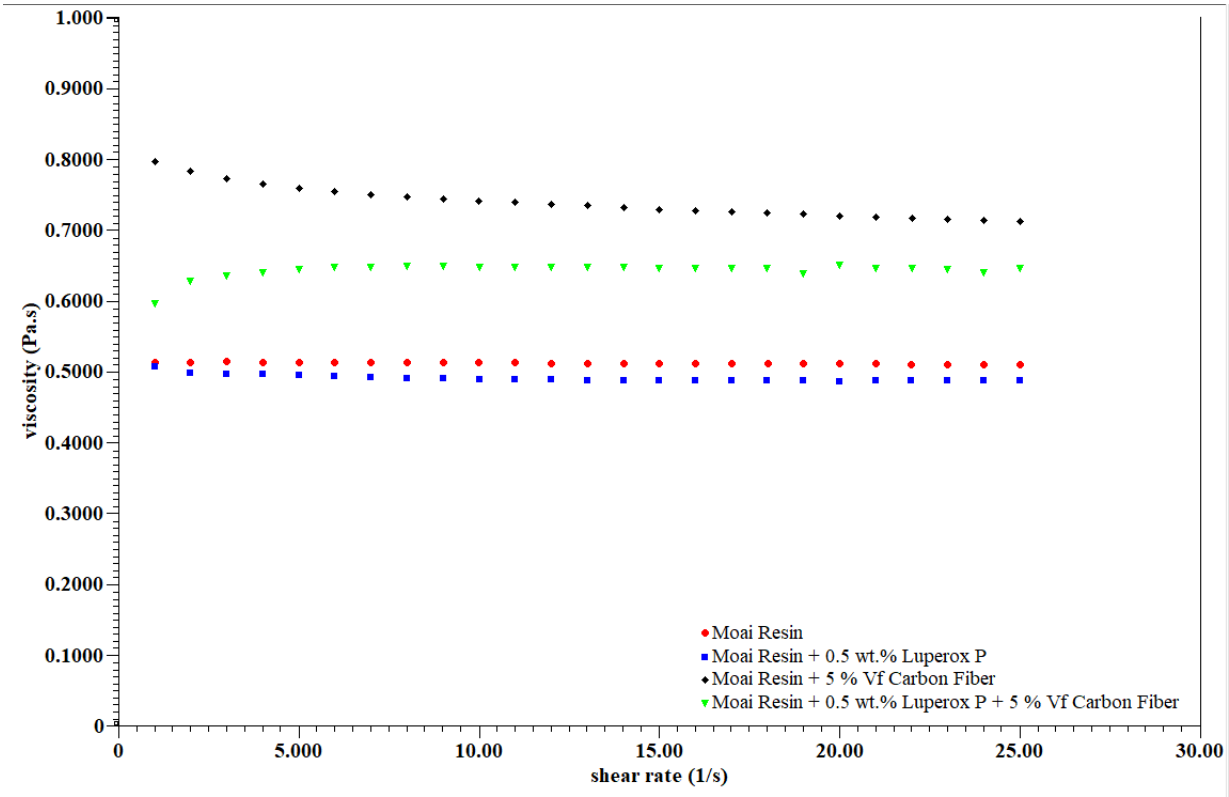

Figure 5.2: Viscosity testing with for shear rate from 1 s^{-1} to 25 s^{-1}.

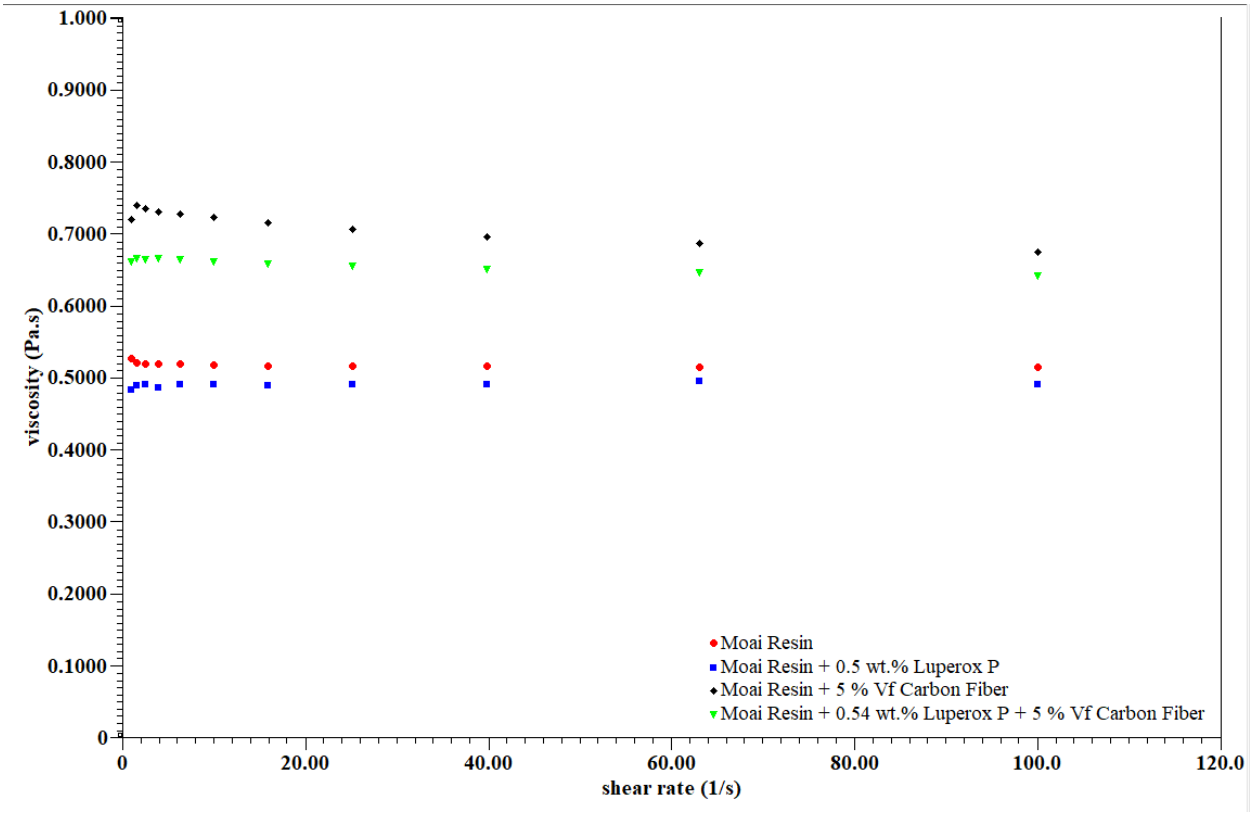

Figure 5.3: Viscosity testing with for shear rate from 1 s^{-1} to 100 s^{-1}.

From Figure 5.2, at lower shear rates both the Moai resin + Luperox P and the Moai resin + carbon fiber exhibit shear thinning behavior [47]. While the Moai resin is near Newtonian in its behavior the Moai resin + carbon fiber + Luperox P exhibits shear thickening behavior [47]. The shear thickening behavior could prove to be an advantage by limiting flow induced fiber orientation while the part is being lowered into the vat during the printing process. Although the addition of the carbon fiber increases the viscosity of the resin system, the lowering of the viscosity caused by the addition of the thermal initiator helps to bring it back down closer to that of the original resin. This aids in ensuring that the vat is able to recoat itself in-between layers during printing, where as if this was unable to happen voids could form in the part being printed. This could become more of an issue if the fiber volume is increased, and could require the addition of a viscosity modifier.

5.2.2. Carbon Fiber Evaluation

Two sources of carbon fiber were evaluated during this research as fiber reinforcement, the Carbiso MF SM45R-100 and Toray T-700 3mm chopped carbon fiber, as discussed in section 4.1.3. The following two sections evaluate their use in SLA printing of short-fiber composites.

5.2.2.1. Processing Effects

The Carbiso fiber were used as received, but the Toray fibers were used after being milled and sorted, as per section 4.1.3. The distribution of the length of 300 fibers of the milled Toray fibers were measured as outlined in section 4.1.3. The fiber had an average length 74.1 ± 40.2 µm, and the distribution of the measured lengths are shown in Figure 5.4.

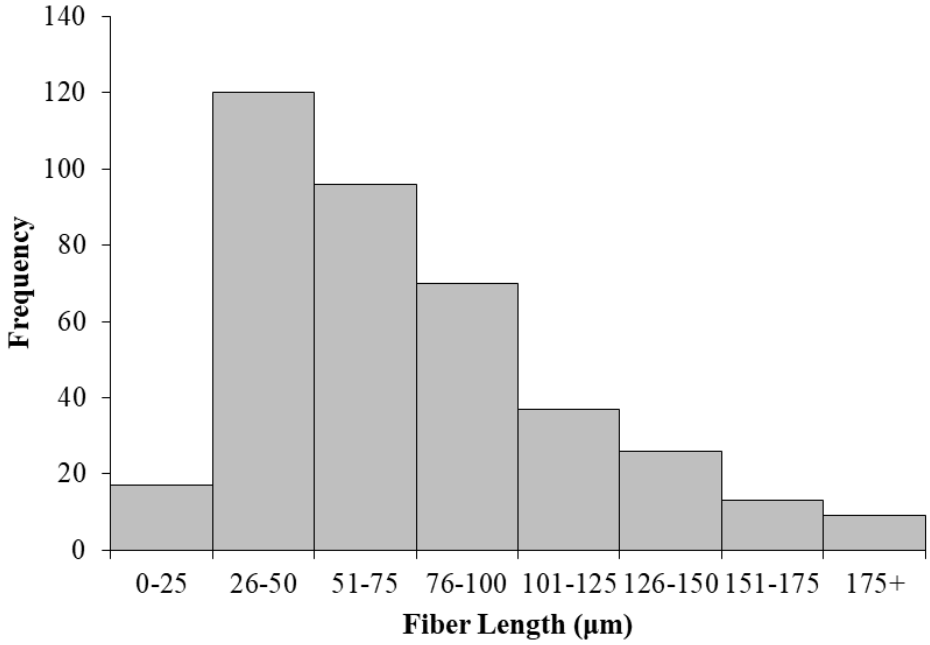

Figure 5.4: Milled Toray T-700 fiber length distribution.

The average length of 74.1 µm was less than the desired length of 100 µm even thought a screen of 120 µm was used. This is mainly due to the large number of fibers below the 76 µm

sieve screen size used being present. The fibers were sieved for 10 minutes through the entire stack up outlined in section 4.1.3 and then collected. The difficulty in extracting fibers within a particular range was due to the small diameter of the fibers (7 μm) allowing for them to easily tilt and slip through the sieve screens. The 10 minute cycle time allowed for the removal of most of the large fibers, but was unable to efficiently separate the smaller fibers (less than 76 μm). Longer cycle times resulted in all fibers passing though the final 76 μm screen in the sieve.

5.2.2.2. Carbiso MF SM45R-100 Carbon Fiber

A short-fiber composite resin consisting of Carbiso MF SM45R-100 carbon fiber, Luperox P, and Moai resin, at a fiber volume of 5%, was prepared as detailed in section 4.2.1. Tensile samples were prepared as per sections 4.2.2 and 4.2.3 with a layer height of 100 μm. The tensile testing was carried out as described in section 4.3.3, with the exception that only 2 specimens were tested per sample in order to decrease the time needed to identify the correct processing parameters in order to manufacture samples. The processing parameters that had to be changed from the default values (used for neat Moai resin) are, laser speed, Z motor speed, PM motor speed, and PM reset position. The parameters that were changed from default settings for that of the samples that produced the highest tensile strength and Young's modulus are shown in Table 5.5.

Table 5.5: Printer settings changed for printing with carbon fiber resin.

Printer Setting	Original Setting	New Setting
Laser Power	55	75
Z Motor Speed	8	6
PM Motor Speed	30	12
PM Reset Position	40	50

The increase in laser power was need due to the opaqueness of the carbon fiber [2, 4, 29] not allowing for the transmission of the energy delivered by the UV laser to be at the same levels seen when using neat Moai resin which is need for activation of the photo initiator [5]. At laser

power settings lower then what was used parts would fail to print or become detached from the print bed. The Z motor speed and PM motor speed control how fast the z-axis and vat tilting moves when going through the peel step of the printing process. By lowering the PM motor speed the force applied to the part during the peel step can be decreased, but at the cost of increasing the print time. The lower Z motor speed and PM reset position allow for more time for the resin to rewet the surface of the vat in between layers due to the increased viscosity of the fiber reinforced resin.

The maximum tensile strength and Young's modulus was found a specified in ASTM D638 section 11.2 and 11.4 respectively with the results summarized in Table 5.6.

Table 5.6: Tensile testing results for Carbiso carbon fiber.

Fiber Volume (%)	**Print Orientation**	**Layer Height (µm)**	**Tensile Strength (MPa)**	**Young's Modulus (GPa)**
5	0°	100	53.8 ± 4.9	2.94 ± 0.222

The Young's modulus of the composite made with the Carbiso MF carbon fiber showed an increase of the Young's modulus of 8% when compared to the neat Moai resin of the same print orientation and layer height. While this is an increase it is still lower than the predicted value of 4.27 GPa. This was thought to be due to weak interfacial properties between the matrix and the fiber [13]. To investigate these possibilities SEM imaging was carried out of a fracture surface of one of the tensile specimens, as outlined in section 4.3.9. The results of the SEM imaging is shown in Figure 5.5.

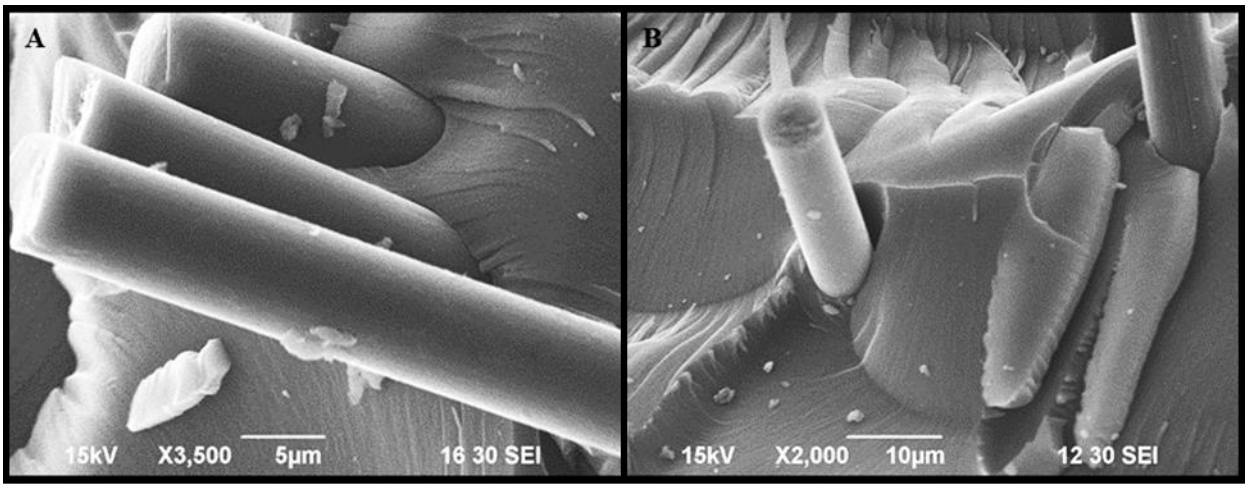

Figure 5.5: SEM imaging of fracture surface of Carbiso fiber composite.

From Figure 5.5, it can be seen that the fiber surface is relatively smooth, and there are locations where the fiber has become debonded from the matrix resulting in fiber pull-out. This indicates weak interfacial properties that result in failure at the interface instead of the load being transferred to the fiber to support the stress within the part [13, 60].

5.2.2.3. Toray T-700 Carbon Fiber

To try and improve the interfacial properties of the composite a different carbon fiber was evaluated. The Toray T-700 comes from the manufacture with an epoxy sizing on the fiber. The sizing on the fiber is used to improve the bonding between the fiber and matrix material, and is used in most composite applications [13]. The shortest available fiber length was 3 mm, and resulted in the fiber having to be processed as specified in section 4.1.3. A short-fiber composite resin consisting of the milled and sieved Toray T-700 carbon fiber at a fiber volume of 5%, Luperox P at 1 wt.%, and Moai resin was prepared as detailed in section 4.2.1. Tensile samples were manufactured and prepared as per sections 4.2.2, 4.2.3, and 4.3.3.1. The tensile testing was carried out as described in section 4.3.3.1, with the exception that only 2 test specimens made per

sample. The settings changed from default for the Moai printer are the same that were used in Table 5.5.

The maximum tensile strength and Young's modulus was found a specified in ASTM D638 section 11.2 and 11.4 respectively with the results summarized in Table 5.7.

Table 5.7: Tensile testing results for Toray T-700 carbon fiber.

Fiber Volume (%)	Print Orientation	Layer Height (µm)	Tensile Strength (MPa)	Young's Modulus (GPa)
5	0°	100	47.1 ± 4.6	3.32 ± 0.067

The Young's modulus of the composite made with the Toray T-700 carbon fiber showed an increase of the Young's modulus of 22% when compared to the neat Moai resin of the same print orientation and layer height, and a 13% increase when compared to the sample made with the Carbiso carbon fiber. With the Toray T-700 fiber showing better results it was used for the remainder of this research. To find the optimal curing schedule for the composite, tensile testing was carried out for samples cured at different times, temperatures, and thermal initiator amount. The Young's modulus was used for comparison, and the results are summarized in Table 5.8.

Table 5.8: Post-curing study for carbon fiber composite (Luperox P).

Temperature (ºC)	Thermal Initiator Amount (wt.%)	Time (hours)	Young's Modulus (GPa)
125	1	2	2.82 ± 0.221
135	1	4	3.12 ± 0.079
135	1	6	3.23 ± 0.293
135	0.5	6	3.33 ± 0.093

There was some improvement between the 4 and 6 hour curing time, and the use of only 0.5 wt.% of thermal initiator (Luperox P) was found to be just as effective. The use of only 0.5 wt.% and a curing schedule of 135 ºC for 6 hours was used to insure the optimum results for the remainder of this research. Due to the difference in some of the specimen geometry for the different characterization testing that will be carried out the longer cure time will insure complete heating of the samples.

To further evaluate the effectiveness of the Luperox P as a thermal initiator, and to attempt to further increase material properties another thermal initiator was also evaluated, cumene hydroperoxide. A short-fiber composite resin consisting of the milled and sieved Toray T-700 carbon fiber at a fiber volume of 5%, cumene hydroperoxide at 0.5 wt.%, and Moai resin was prepared as detailed in section 4.2.1. Tensile samples were manufactured and prepared as per sections 4.2.2, 4.2.3, and 4.3.3.1. The tensile testing was carried out as described in section 4.3.3.1, with the exception that only 2 test specimens made per sample. The settings changed from default for the Moai printer are the same that were used in Table 5.5.

To find the optimal curing schedule for the composite, tensile testing was carried out for samples cured at different temperatures and times. The Young's modulus was used for comparison, and the results are summarized in Table 5.9.

Table 5.9: Post-curing study for carbon fiber composite (Cumene Hydroperoxide).

Temperature (ºC)	**Time (hours)**	**Young's Modulus (GPa)**
90	12	0.36 ± 0.025
100	8	0.45 ± 0.001
135	6	2.1 ± 0.252

The use of cumene hydroperoxide was looked at or a wide temperature region and times due to the cracking that would appear after post-curing at 135 ºC, with examples of this shown in Figure 5.6.

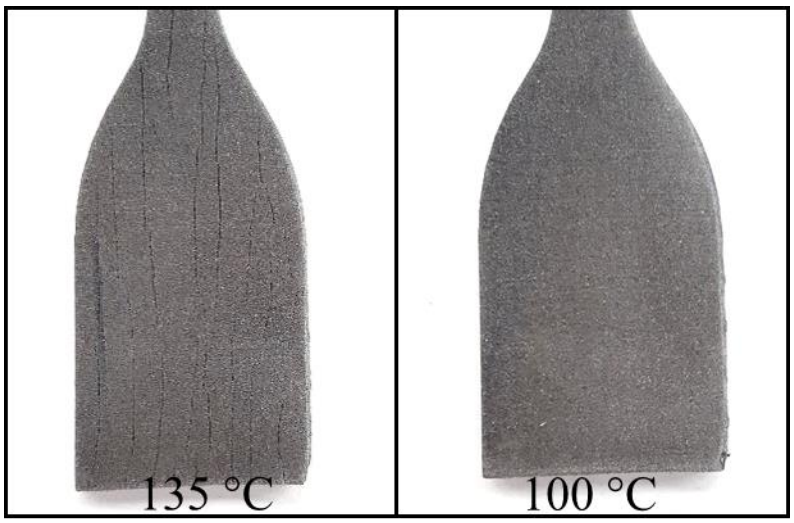

Figure 5.6: Cracks in cumene hydroperoxide post-cured specimens.

The cracks would run both parallel (front of specimen) and perpendicular (side of specimen) to the loading direction of the tensile testing. This resulted in the low modulus seen due to system compliance [44]. At lower temperatures the thermal initiator would not activate and fully cure the sample. This can be seen in Table 5.9 from the low results of the Young's modulus.

5.2.3. Fiber Volume Consistency and Porosity

5.2.3.1. Fiber Volume Consistency

The fiber volume consistency was evaluated as outlined in section 4.3.6. The results summarized in Table 5.10, with the full results in APPENDIX A, Table A.1 and Table A.2.

Table 5.10: Summarized fiber volume consistency results for flexural samples.

Layer Height (µm)	Print Time (hours)	Top (% V_f)	Middle (% V_f)	Bottom (% V_f)
100	3.0	5.23 ± 0.02	4.84 ± 0.10	3.57 ± 0.27
50	5.25	5.45 ± 0.15	4.50 ± 0.13	3.88 ± 0.01

From Table 5.10 it can be seen that a fiber volume gradient is present with in the samples. The top section of the samples have a higher fiber volume then what the resin mixture was designed to have (5% V_f). This is due to the lowering of the bed plate into the vat trapping

more fibers in-between the sample and bottom of the vat then desired. The reason believed for the samples to have lower and similar fiber volume gradients despite the different print times, is that the area around the sample being printed becomes depleted of fibers as the sample is printed. This slowly lowers the fiber volume of the sample as it is going through the printing process. The possible effects of this fiber volume gradients effect on the material properties will be discussed in the following Material Characterization section 5.2.4.

Because the flexural specimens have a larger cross-section area throughout the entire specimen the fiber gradient appears more pronounced. Similar burn off testing was carried out with the tensile specimens (geometry shown in Figure 4.10) with the exception that only the two ends were tested. This was done early on in the manufacturing process to evaluate the consistence of the print process. The average difference in the fiber volume of the top and bottom portions of the tensile specimens change by on average of 0.8% for the specimens printed in the 90º orientation. This lower difference could be to the varying specimen geometry, or that due to their large size a less number of specimens were printed at the same time to keep the print time short. This allowed for more spacing between the specimens, and could have prevented the fiber from becoming depleted from around the specimens being printed.

The Moai printer has no built in mixing method such as a pump or wiper arm that can be found in some other manufactures printers. To facilitate mix of the resin the setting for the distance the vat tilts (PM Reset Position) when the peel step occurs was increased from the default setting of 40 to 50. While this did aid in recoating the vat surface, the gradient in the fiber volume was still present in the samples. Increasing this value can also had the negative effect of increasing the peel force on the parts therefore limiting the amount it can be increased. During the course of this research attempts were made to incorporate a pump into the resin vat were

made, but the effort was unsuccessful. This was mainly due to the limited amount of space to incorporate the necessary equipment. Recommendations for a solution to the problem of fiber volume consistency are presented in the Future Recommendations section 6.2.

5.2.3.2. Composite Porosity

The results of the void content testing along with the densities, outlined in section 4.3.7, are summarized in Table 5.11, with the full results for the testing in APPENDIX A, Table A.4.

Table 5.11: Density and void content of composite samples.

Layer Height	Sample	Density (g/cm3)	Void Content (%)
100 μm	5% Vf Carbon Fiber + 0.5 wt.% Luperox P	1.25	1.32
50 μm	5%Vf Carbon Fiber + 0.5 wt.% Luperox P	1.25	0.70
100 μm	0.5 wt.% Luperox P	1.24	-

The voids present in the composite samples can originate both during the manufacturing of the fiber reinforced resin used for printing and during the printing of the samples. Although the resin was degassed in a vacuum chamber before using there could still be air trapped in the resin and to the fibers themselves. Voids can be introduced during the peel step between every layer when the sample is raised up from the vat. During the photo polymerization process the volume of the liquid resin is reduced when going to a solid. This leaves behind a negative space that can then form bubbles that are trapped in the liquid resin, and then be incorporated into the sample. This was observed in some of the Moai resin samples before parameters were adjusted by allowing the vat and bed to separate more in-between layers. The Moai resin parts are transparent so any samples with visible voids could be removed from testing and reprinted. For the samples made with carbon fiber, they are not transparent and therefore it could be possible for samples with voids formed due to this manufacturing defect to still be used as testing specimens.

The voids could also be due to the thermal initiator producing gas byproducts during the post-curing process [61]. With the 100 μm layer height having more unreacted resin from the photo polymerization process then the 50 μm layer height, with this being elaborated on more in the following section 5.2.4.1. This could be why the 100 μm layer height was seen to have a higher void content than that of the 50 μm layer height samples. The presence of voids within the composite will act as stress concentrators, but a 1% void content is considered good whereas around 5% would be considered poor for traditional laminate composites [13].

5.2.4. Material Characterization

5.2.4.1. Tensile Testing

A short-fiber composite resin consisting of the milled and sieved Toray T-700 carbon fiber at a fiber volume of 5%, Luperox P at 0.5 wt.%, and Moai resin was prepared as detailed in section 4.2.1. Tensile samples were manufactured and prepared as per sections 4.2.2, 4.2.3, and 4.3.3.1. The tensile testing was carried out as described in section 4.3.3.1, with the exception the test numbers 4,8,12, and 16 from Table 4.7 were left out. The test omitted represent the samples made with carbon fiber and no thermal initiator, which was shown as ineffective in section 5.1.1. The settings changed from default for the Moai printer are the same that were used in Table 5.5, unless otherwise stated.

It was found the by applying a thin layer of neat Moai resin to the print bed before starting the print aided in keeping the part fixed to the bed during the printing process. The thin layer of neat resin was able to cure more during the over exposer processes during the first few layers. When no neat resin was applied to the bed before printing some specimens would become unattached from the bed during the peel step, resulting in print failure. The success rate of prints

with the thin layer of neat resin applied to the bed was greatly increased, and would be recommend for any future research with this style of SLA printer to aid in part success.

To aid in sample identification the follow naming scheme will be implemented for the remainder of this paper. It will consist of the main material parameter being looked at along with the layer height and print orientation, shown in Table 5.12.

Table 5.12: Sample identification guide.

Abbreviation	Sample Components	Layer Height	Print Orientation
M100-0	Moai Resin	100	0º
M100-90	Moai Resin	100	90º
M50-0	Moai Resin	50	0º
M50-90	Moai Resin	50	90º
LP100-0	Moai Resin + 0.5 wt.% Luperox P	100	0º
LP100-90	Moai Resin + 0.5 wt.% Luperox P	100	90º
LP50-0	Moai Resin + 0.5 wt.% Luperox P	50	0º
LP50-90	Moai Resin + 0.5 wt.% Luperox P	50	90º
CF100-0	Moai Resin + 0.5 wt.% Luperox P + 5% V_f Carbon Fiber	100	0º
CF100-90	Moai Resin + 0.5 wt.% Luperox P + 5% V_f Carbon Fiber	100	90º
CF50-0	Moai Resin + 0.5 wt.% Luperox P + 5% V_f Carbon Fiber	50	0º
CF50-90	Moai Resin + 0.5 wt.% Luperox P + 5% V_f Carbon Fiber	50	90º

The maximum tensile strength and Young's modulus was found as specified in ASTM D638 section 11.2 and 11.4 respectively, and the results are shown in Figure 5.7, Figure 5.8, Figure 5.9, Figure 5.10, and summarized in Table 5.13 [48]. The results for the samples printed in the 0º orientation are shown in Figure 5.7 and Figure 5.8., and the samples printed in the 90º orientation are shown in Figure 5.9 and Figure 5.10.

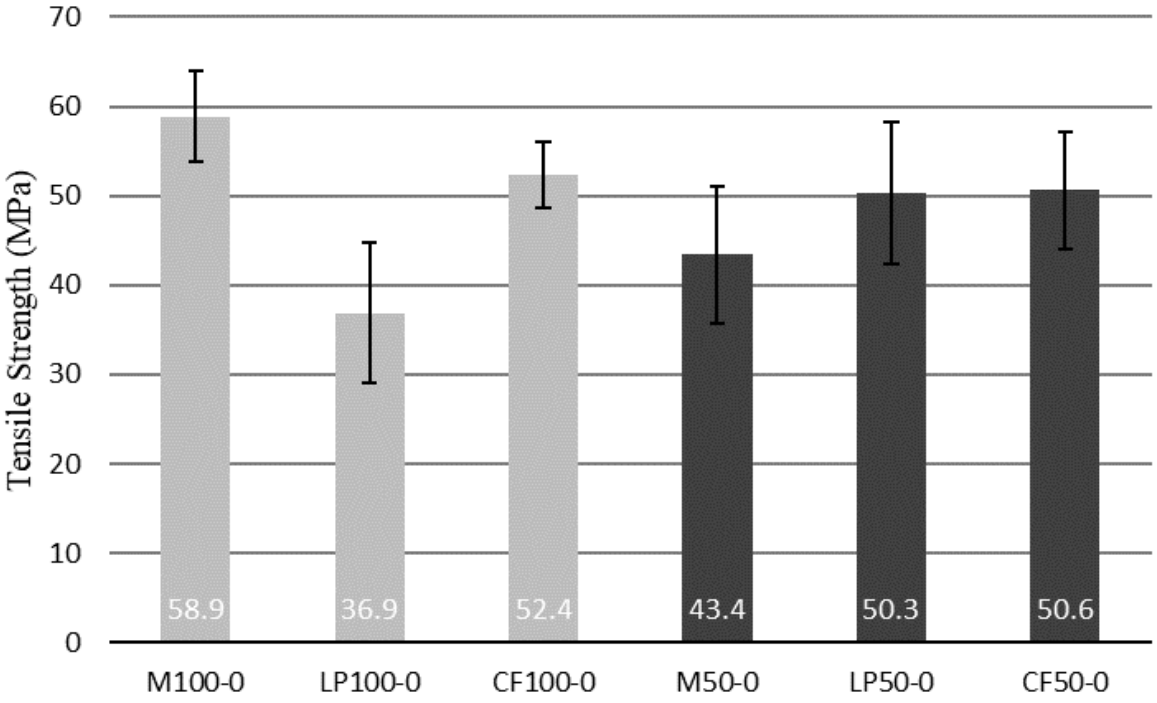

Figure 5.7: Tensile strength results for 0º print orientation.

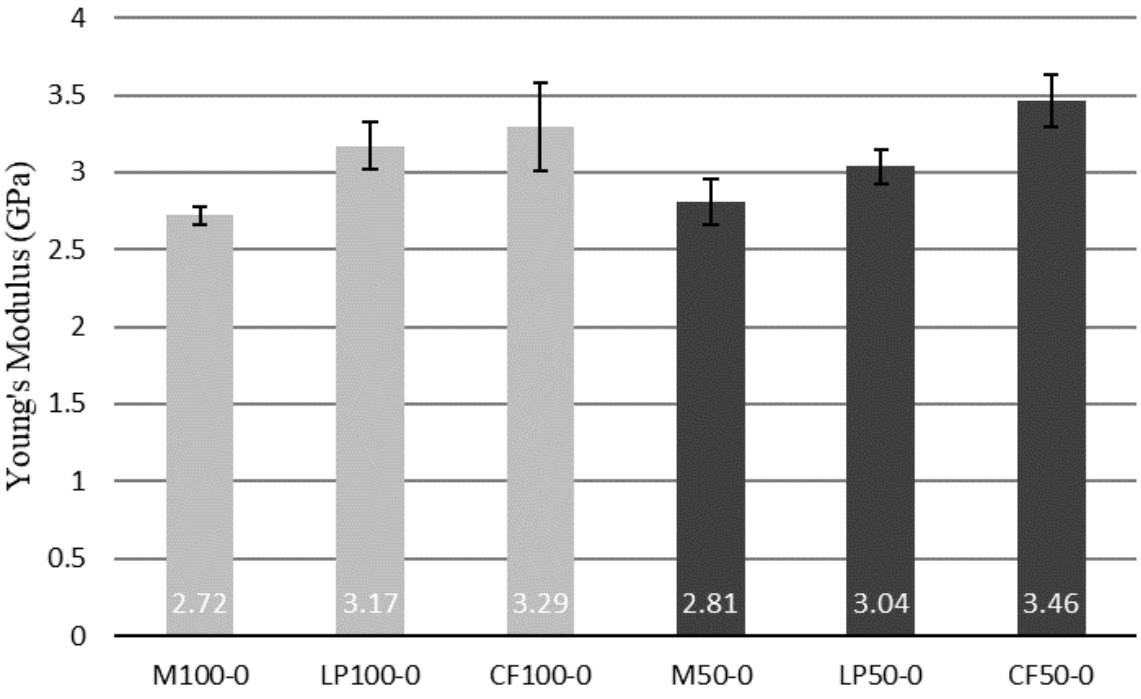

Figure 5.8: Young's modulus results for 0º print orientation.

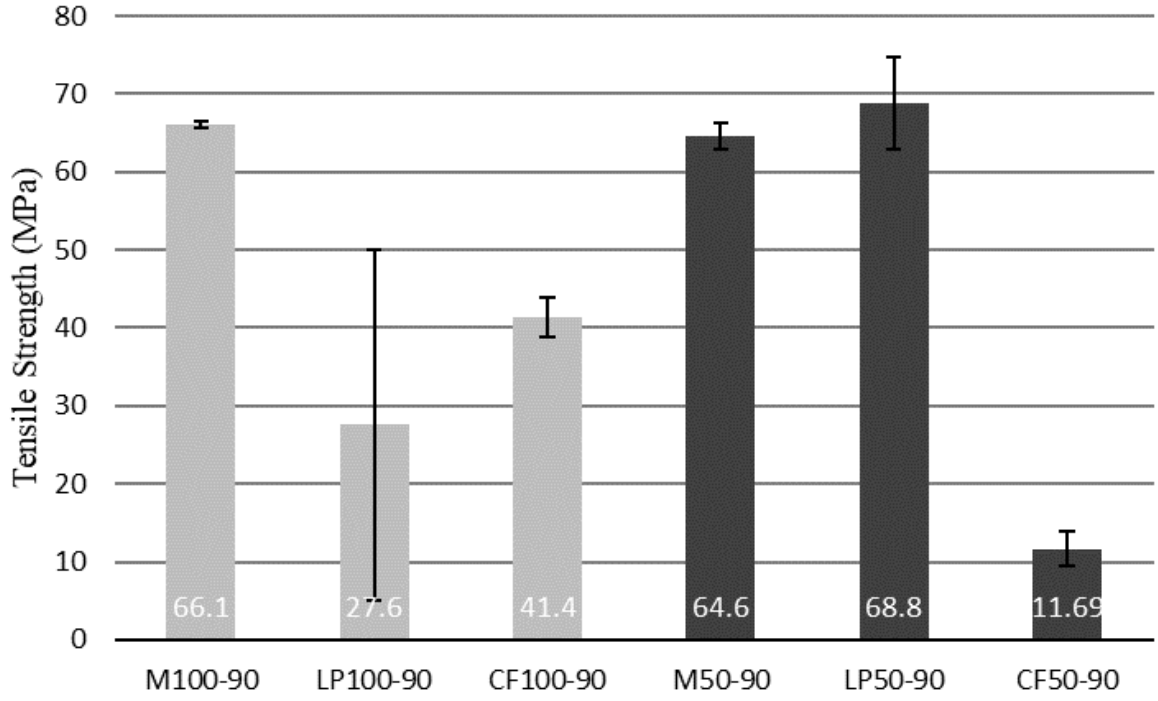

Figure 5.9: Tensile stregnth results for 90º print orientation.

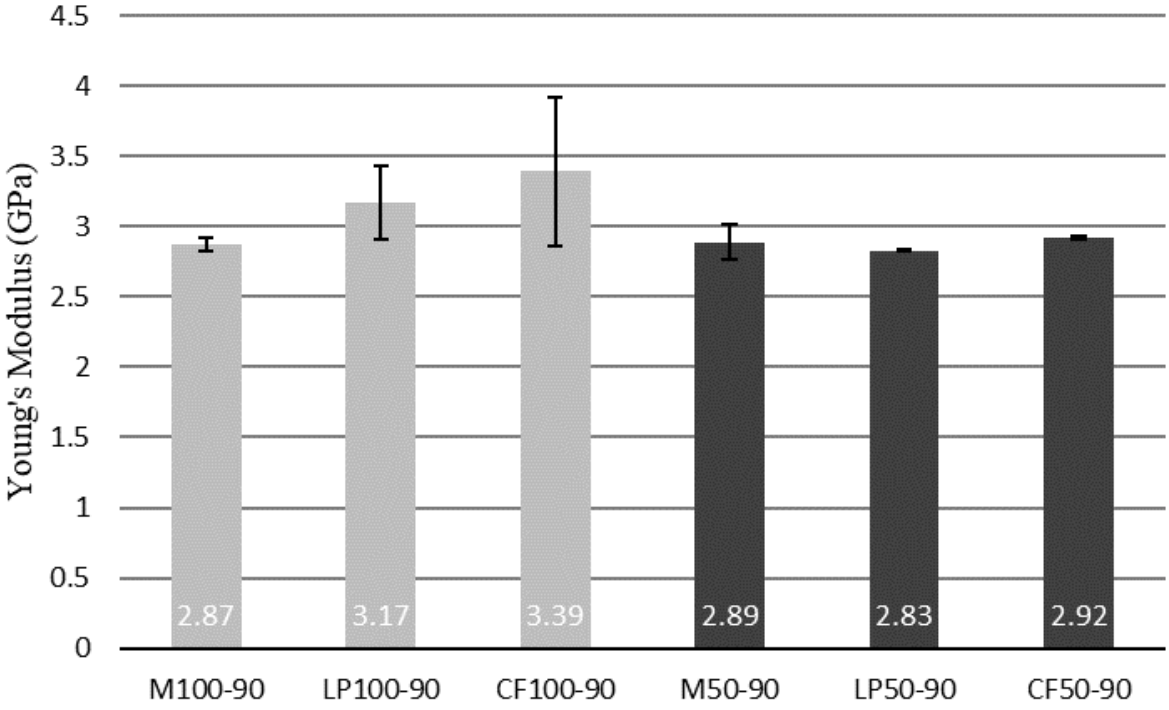

Figure 5.10: Young's modulus results for 90º print orientation.

Table 5.13: Summarized tensile testing results.

Sample	Layer Height (μm)	Print Orientation	Fiber Volume (%)	Tensile Strength (MPa)	Young's Modulus (GPa)
M100-0	100	0°	0	58.9 ± 5.0	2.72 ± 0.06
M100-90	100	90º	0	66.1 ± 0.4	2.87 ± 0.05
M50-0	50	0°	0	43.4 ± 7.7	2.81 ± 0.15
M50-90	50	90º	0	64.6 ± 1.6	2.89 ± 0.12
LP100-0	100	0°	0	36.9 ± 7.9	3.17 ± 0.15
LP100-90	100	90º	0	22.5 ± 22.5	3.17 ± 0.26
LP50-0	50	0°	0	50.3 ± 7.7	3.04 ± 0.11
LP50-90	50	90º	0	68.8 ± 5.9	2.83 ± 0.01
CF100-0	100	0°	5	52.4 ± 3.7	3.29 ± 0.29
CF100-90	100	90º	5	41.4 ± 2.6	3.39 ± 0.52
CF50-0	50	0°	5	50.6 ± 6.6	3.46 ± 0.17
CF50-90	50	90º	5	11.69 ± 2.28	2.92 ± 0.01

When comparing the Young's modulus of the samples there was an increase of 21% between the M100-0 and CF100-0 samples, and an increase of 27% for the M50-0 and the CF50-0. With an increase in Young's modulus for the CF50-0 samples when compared to the CF100-0 of 5%. While showing only 4% increase between the LP100-0 and CF100-0 samples, and 13% increase for the LP50-0 and CF50-0. These increase in the Young's modulus are not as high as what would be predicted theoretically using Equations 2.2 thru 2.6 for a randomly distributed short-fiber composite (CF100 samples). Using the average fiber length, found in section 5.2.2.1, of 76 μm the theoretical modulus for a randomly distributed composite would be 4.05 GPa, and for a unidirectional composite it would be 5.42 GPa.

The theoretical modulus for the randomly distributed composite is 23% higher than that of the CF100-0 sample. This is in part due to the distribution of the shorter fiber lengths within the sample, but also that the theoretical model also assumes perfect bonding between the fiber and matrix along with an absents of voids [13]. Evidence of the weak interfacial properties of the short-fiber composite samples can be seen in Figure 5.11.

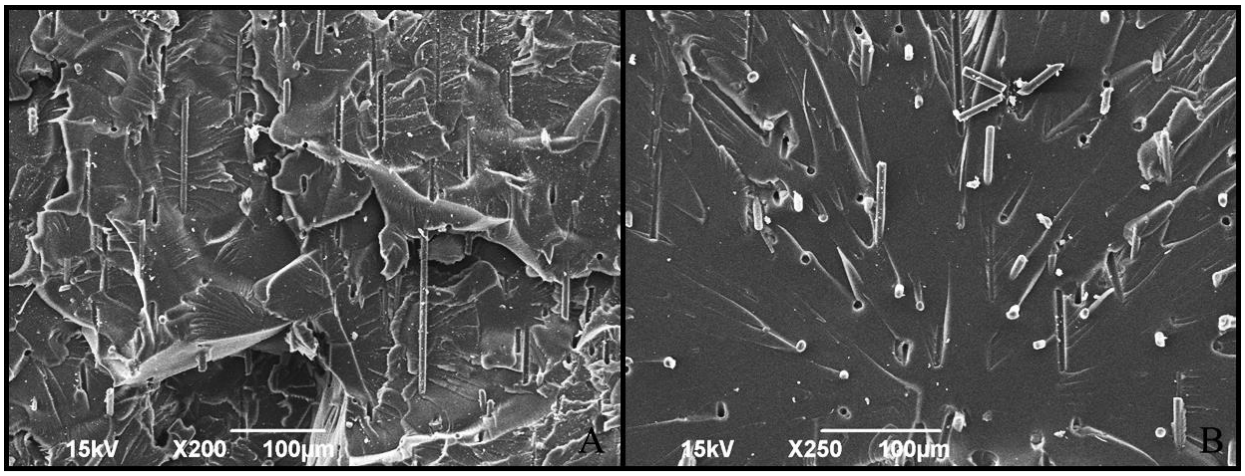

Figure 5.11: Fracture surface of CF50-0 (A) X200 and (B) X250 magnification.

In Figure 5.11, the smooth channels left behind from the carbon fiber in A, the clean (lack of bonded matrix material) fibers present in B, and the smooth holes in B are all signs of weak interfacial properties due to poor bonding between the matrix and fiber [13, 60]. This limits the ability for the matrix to transfer stress to the fibers and therefore reducing its overall properties [13]. If the composite had better interfacial properties there would have been evidence of fiber breakage, which was not present in any of the SEM Images taken [13, 60]. The results of the fiber volume consistence (section 5.2.3.1) showed that a fiber volume gradient existed in the samples produced, but the gage section of the tensile sample is in the middle of the print were the fiber volume should be more uniform, due to the lower difference found between the top and bottom of the tensile specimen fiber volume content (0.8%).

When comparing the modulus of the carbon fiber samples printed at different layer heights (100 µm and 50 µm) the increase in modulus of 5% can be attributed to the partial alignment of the fibers in the loading direction. While the CF100-90 has a higher modulus than the CF50-90 samples. While this would be expected if the material was going from isotropic material to a special orthotropic material due to fiber alignment, it is not the case for these

samples due to cracks being present in the CF50-90 samples [13]. The cracks presence and their effect in the CF50-90 samples will be discussed in greater detail later in this section. The alignment of the fibers via layer height is demonstrated in Figure 5.12 with the yellow arrows highlighting the various fiber orientations.

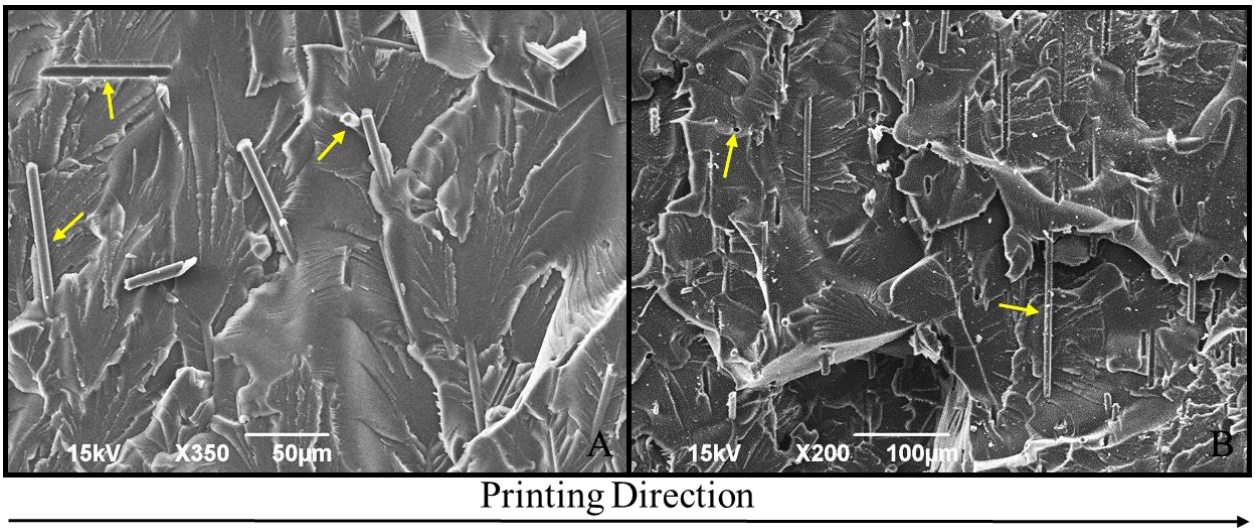

Figure 5.12: Fracture surface of (A) CF100-90 and (B) CF50-90 specimens.

When comparing the strength of the Moai resin samples, the samples printed in the 90º print orientation for the Moai resin have a higher strength when compared to the same samples printed in the 0º print orientation. This is due to the effects of the support material being removed and leaving behind notches in the specimen, examples of this can be seen in Figure 4.7 in section 4.2.3. These notches then act as small stress concentrators resulting in lower strength of the sample [44]. Due to these effects the Moai resin samples tested at a print orientation of 90º are a better representation of the actual ultimate tensile strength of the neat resin material.

The samples tested with just the thermal initiator (Luperox P) added also showed flaws the contributed to a lower tensile strength result. These are from cracks there were present on the

surface of the samples that originated during the curing process, with an example of these defects shown in Figure 5.13.

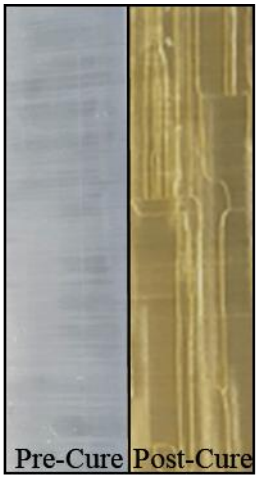

Figure 5.13: Surface cracking from thermal curing.

The cracks originate from the volumetric shrinkage that occurs during the post-curing process as the degree of conversation within the system increases [62]. A slower curing schedule might be able to produce samples without cracks, but it was keep the same as the carbon fiber samples for comparison purposes. The volumetric shrinkage due to post-curing was found for the different samples as outlined in section 4.3.8. The results for the volumetric change in the samples from post-curing are summarized in Table 5.14, with the full results in APPENDIX A, Table A.5 thru Table A.10.

Table 5.14: Volumetric shrinkage (%) of post-cured samples.

Sample	**Volume Shrinkage (%)**
M100	1.4 ± 0.6
LP100	3.5 ± 0.6
CF100	1.1 ± 0.8
M50	0.8 ± 0.5
LP50	1.0 ± 0.7
CF50	0.4 ± 0.3

The largest change in volume can be seen in the LP-100 sample, and the largest decrease in strength can be seen in the LP100-0 and LP100-90 samples. The LP-100 tension samples also showed the largest number of cracks when compared to the LP50-0 and LP50-90 samples. This is due to the dual-cure system working against itself. When the samples are first cured rapidly using the photo initiator the polymer quickly becomes fixed in place at a low degree of conversation [62]. During the post-curing process the thermal initiator then reacts with remaining function groups increasing the shrinkage and therefore stress within the sample causing cracks to develop [62]. This is more pronounced in the samples at a 100 μm layer height due to there being more unreacted material for the thermal initiator to react with, due to the lower degree of conversion from less energy being delivered to the photo initiator [32, 62]. This can also be seen in SEM images taken from the fracture surfaces of the tensile specimens. Figure 5.14 is of the fracture surface of a M100-90 specimen.

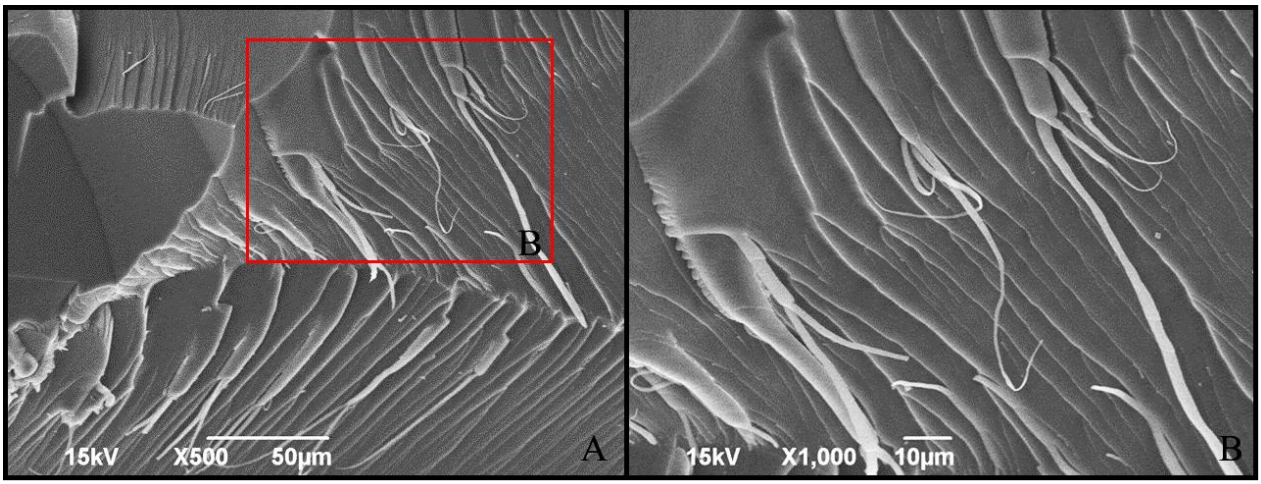

Figure 5.14: M100-90 fracture surface at (A) X500 and (B) X1000 magnification.

From Figure 5.14 the fracture appears as brittle until increasing the magnification and then areas of plastic deformation can be seen, and indicating more of a ductile failure on a

smaller level [60]. Looking at a M50-90 specimen, in Figure 5.15, the fracture pattern is completely brittle with the ribbon features seen in Figure 5.14 not present [60].

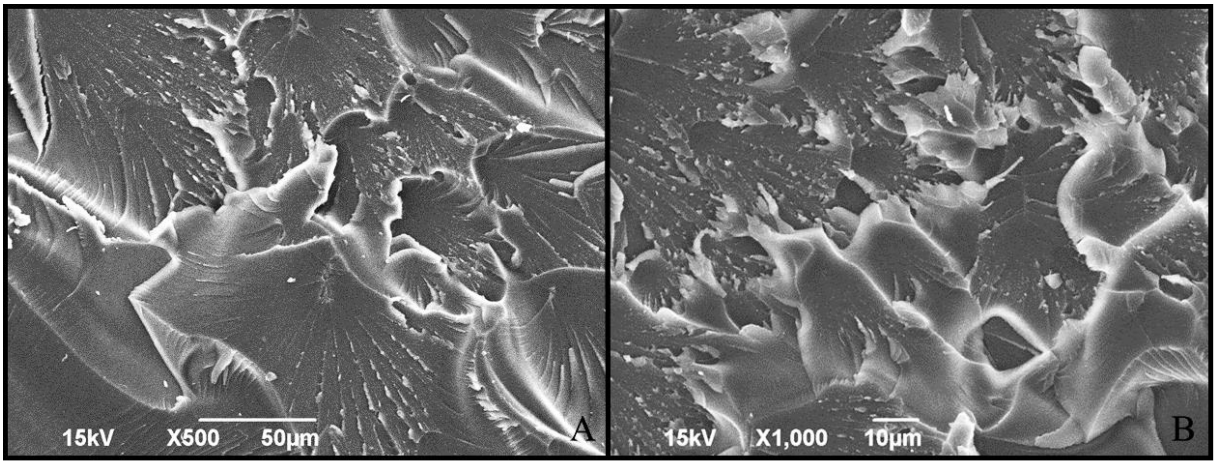

Figure 5.15: M50-90 fracture surface at (A) X500 and (B) X1000 magnification.

The thinner layer when printing allows for a higher degree of cure in the 50 µm layer height samples when compared to the 100 µm layer height sample, due to the higher amount of energy being delivered to the photo initiator during the printing process [32]. This is also evident in Table 5.14 with the volumetric post-cure percent shrinkage of the M100 being nearly twice that of the M50 sample. The SEM images for a LP100-0 specimen, Figure 5.16, show only the brittle failure features that are as seen in the M50 samples [60].

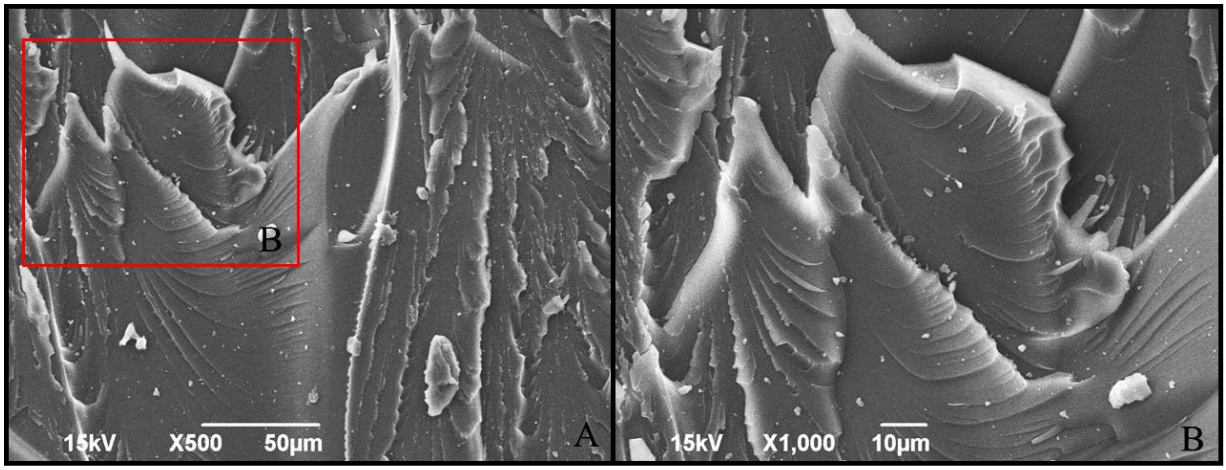

Figure 5.16: LP100-0 fracture surface at (A) X500 and (B) X1000 magnification.

The samples with carbon fiber on the other hand, show similar shrinkage as the Moai resin samples even though there would be unreacted resin due to the shadowing of the carbon fiber from the UV light source. The lower shrinkage of the carbon fiber samples is due to the carbon fiber providing dimensional stability to the samples during the curing process by limiting their thermal expansion, and the volume of the carbon fiber displacing some of the volume of the resin when compare to the original volume of resin in neat Moai samples [13, 32].

The lower strength of the carbon fiber samples is due in part by the end effects of the fiber reinforcement acting as stress concentrators within the composite [13]. This is caused by the large number of very short fibers (much less than the critical length) in the distribution of the lengths, seen in Figure 5.4, being present in the sample [13]. The presence of voids with in the carbon fiber samples can also act as stress concentrators and farther weaken the samples, but the low void content found (section 5.2.3.2) for the samples should help minimize the effect [63].

The cracks seen on the surface of the LP100 and LP50 samples were not seen in the carbon fiber samples, but the CF50-90 sample did have cracks present before post-curing from the printing processes itself, examples of these cracks are shown in Figure 5.17.

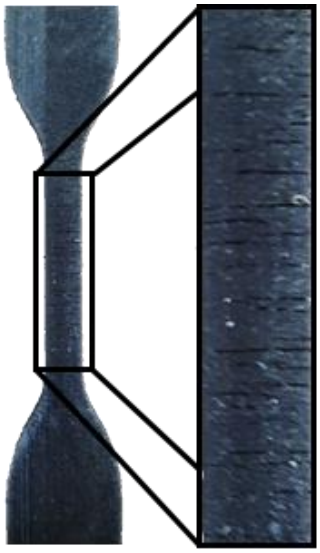

Figure 5.17: Cracks in CF50-90 sample from printing.

This was caused due to the smaller layer height not having as much matrix material available for holding one layer to the next. During the peel step of the printing process, when the part would be separated from the silicon layer on the bottom of the vat, it would generate enough stress to separate previous layers. Multiple attempts to print the CF50-90 specimens resulted in failures due to the layers sticking to the bottom of the vat instead of the printed part itself. Examples of these failures shown in Figure 5.18.

Figure 5.18: Examples of CF50-90 print failures.

From Figure 5.18, the cone shaped failures in the print are from a small piece of a layer separating from the part and sticking to the vat, as the subsequent layers are printed this small piece sticking to the vat slowly increase in size until causing printing failure. To overcome this and manufacture specimens that could be tested the PM motor speed was lowered until part failure no longer occurred, this was found to be a value of 6 for the Moai printer settings. By lowering the speed of the PM motor it deceased the force generated of the part during the peel step, but could not completely remove it resulting in the cracks seen in the specimens. The cracks being present in the specimens caused a large decrease in the strength of the CF50-90 samples due to the cracks decreasing in the actual cross-sectional area and acting as stress concentrators [44]. While also decreasing the Young's modulus by increasing the compliance of the specimens [44].

The strength of the short-fiber composites were also affected by the length of the carbon fiber being used. To get the maximum amount of reinforcement from the carbon fiber the fiber needs to be over a critical length, l_c, to maximize the load transfer between the fiber and matrix [13]. This can be found for the current composite system by solving Equation 2.1, with the fiber properties given in Table 4.3, and assuming a shear yield stress of the matrix to be half of the tensile strength of the matrix with the critical fiber length for this system being 434 μm [13]. The shorter length of the fibers (76 μm) being used means that the load is not being fully transferred to the fiber, and limiting the composites performance [13].

The statistical analysis for the tensile testing results for the Young's modulus and ultimate tensile strength of the evaluated materials is examined in the following two sections, as outlined in section 4.3.3.2

5.2.4.1.1. Young's Modulus

The results for the Young's modulus for the samples tested were evaluated using ANOVA and if needed a post-hoc Tukey HSD test, as outlined in section 4.3.3.2. The samples were compared across 4 different groups these were, 0º and 90º print orientation and 100 µm and 50 µm layer heights. The groups analyzed are shown in Table 5.15.

Table 5.15: Statistical analysis groups.

Group Parameter	Groups					
0º Print Orientation	M100-0	LP100-0	CF100-0	M50-0	LP50-0	CF50-0
90º Print Orientation	M100-90	LP100-90	CF100-90	M50-90	LP50-90	CF50-90
100 µm Layer Height	M100-0	LP100-0	CF100-0	M100-90	LP100-90	CF100-90
50 µm Layer Height	M50-0	LP50-0	CF50-0	M50-90	LP50-90	CF50-90

The results for the ANOVA analysis when comparing samples in the 0º print orientation are summarized in Table 5.16, with the full ANOVA results in Table B.1 in APPENDIX B.

Table 5.16: ANOVA summary for Young's modulus in 0º print orientation.

Source of Variation	Sum of Squares	Degrees of Freedom	Mean Square	F-Statistic	P-value	F-Critical
Between Groups	1.99	5	0.398	13.84	$2.05*10^{-6}$	2.62
Within Groups	0.691	24	0.0288	-	-	-

The ANOVA result were also plotted in MatLab as notched box plots for visual examination of the data, and is shown in Figure 5.19.

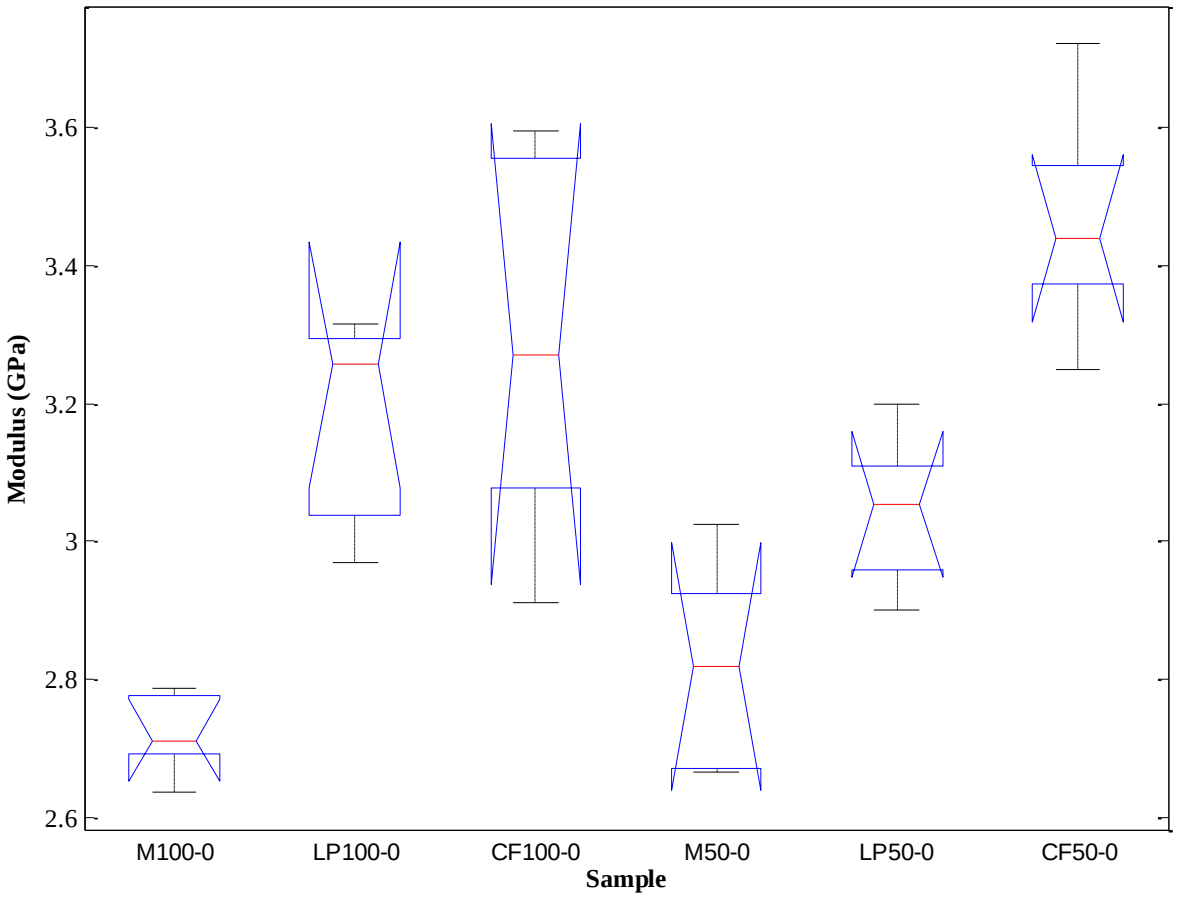

Figure 5.19: Box plot of ANOVA results for Young's modulus in 0º print orientation.

From the results of the ANOVA testing the p-value of $2.05*10^{-6}$ is less than that of 0.05 for the 95% confidence level chosen. This indicates that there is significant differences between at least two of the means in the sample groups tested [50]. From Figure 5.19 a visual determination can be made to determine which groups differ, and it can be seen that there is some separation between the notches in the box plots of the samples. The summarized results of the Tukey test for the 0º sample groups that showed significant differences are shown in Table 5.17, with the full Tukey results in APPENDIX B, Table B.2.

Table 5.17: Tukey HSD results for Young's modulus in 0º print orientation.

Compared Pairs	Tukey HSD Q statistic	Tukey HSD p-value	Tukey HSD inference
M100-0 vs LP100-0	5.9817	0.0035542	p<0.01
M100-0 vs CF100-0	7.4633	0.0010053	p<0.01
M100-0 vs CF50-0	9.7304	0.0010053	p<0.01
LP100-0 vs M50-0	4.7848	0.0262724	p<0.05
CF100-0 vs M50-0	6.2664	0.0021738	p<0.01
M50-0 vs CF50-0	8.5336	0.0010053	p<0.01
LP50-0 vs CF50-0	5.5414	0.0075388	p<0.01

From Table 5.17, both CF100-0 and CF50-0 differ statistically and have higher moduli then the M100-0 and M50-0 moduli, respectively. The results also show that the LP100-0 does not differ from the CF100-0 or the CF50-0. This is in part due to the large deviation with in the CF100-0 sample. This indicates that somewhere within the processing parameters something is causing a deviation with in the manufacturing of the samples [50]. This could be due to things such as fiber distribution, voids, or other unseen imperfections in the sample, with solutions for these issues proposed in later sections. This can be seen with the CF50-0 being statistical different than the LP50-0, due to the smaller deviation within the confidence interval of the CF50-0 samples when compared to the CF100-0 samples.

The results for the ANOVA analysis when comparing samples in the 90º print orientation are summarized in Table 5.18, with the full ANOVA results in Table B.3 in APPENDIX B.

Table 5.18: ANOVA summary for Young's modulus in 90º print orientation.

Source of Variation	Sum of Squares	Degrees of Freedom	Mean Square	F-Statistic	P-value	F-Critical
Between Groups	1.25	5	0.251	2.02	0.112	2.62
Within Groups	2.98	24	0.124	-	-	-

The ANOVA result were also plotted in MatLab as notched box plots for visual examination of the data, and is shown in Figure 5.20.

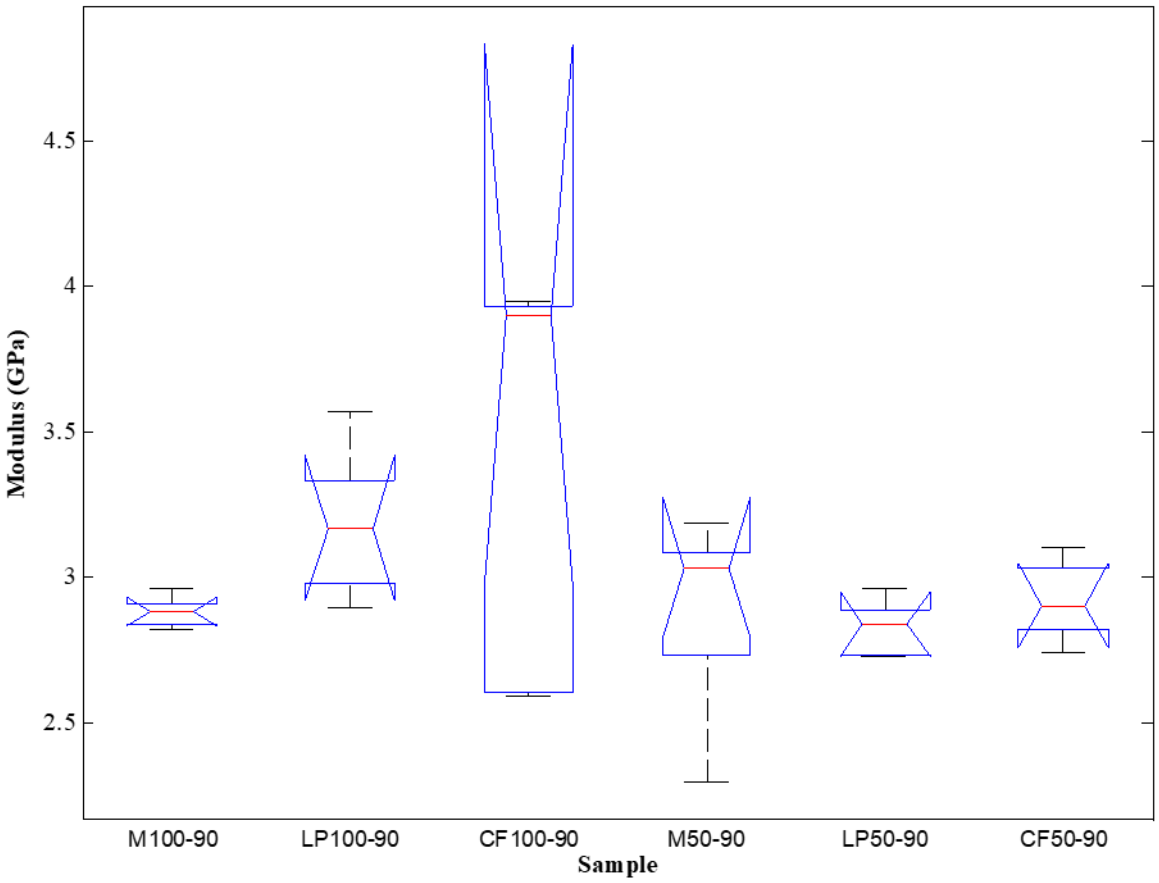

Figure 5.20: Box plot of ANOVA results for Young's modulus in 90º print orientation.

From the results of the ANOVA testing the p-value of 0.112 is greater than that of 0.05 for the 95% confidence level chosen. This indicates that there is not a significant difference

between the sample groups tested [50]. From Figure 5.20, a visual determination can be made to confirm that the groups do not differ, and it can be seen that there is overlap between all of the samples within the 95% confidence level, represented by the ends of the notches. This is in part due to the large deviation with in the CF100-90 sample. As was mentioned before with the CF100-0, this is due to inconsistences within the printing process. If this deviation could be corrected for more consistent samples then the CF100-90 would be statistical different than the other samples tested. This is seen in the box plots median value (3.90 GPa) for the CF100-90 being higher than its mean value (3.39 GPa), and highlights the potential for improvement in the material properties. For completeness, the Tukey HSD test was still carried out with none of the results indicating any significant differences. The results of the Tukey test for the 90º sample groups can be found in APPENDIX B, Table B.4.

The results for the ANOVA analysis when comparing samples printed at a 100 μm layer height are summarized in Table 5.19, with the full ANOVA results in Table B.5 in APPENDIX B.

Table 5.19: ANOVA summary for Young's modulus printed at 100 μm layer height.

Source of Variation	Sum of Squares	Degrees of Freedom	Mean Square	F-Statistic	P-value	F-Critical
Between Groups	1.63	5	0.326	2.78	0.0404	2.62
Within Groups	2.81	24	0.117	-	-	-

The ANOVA result were also plotted in MatLab as notched box plots for visual examination of the data, and is shown in Figure 5.21.

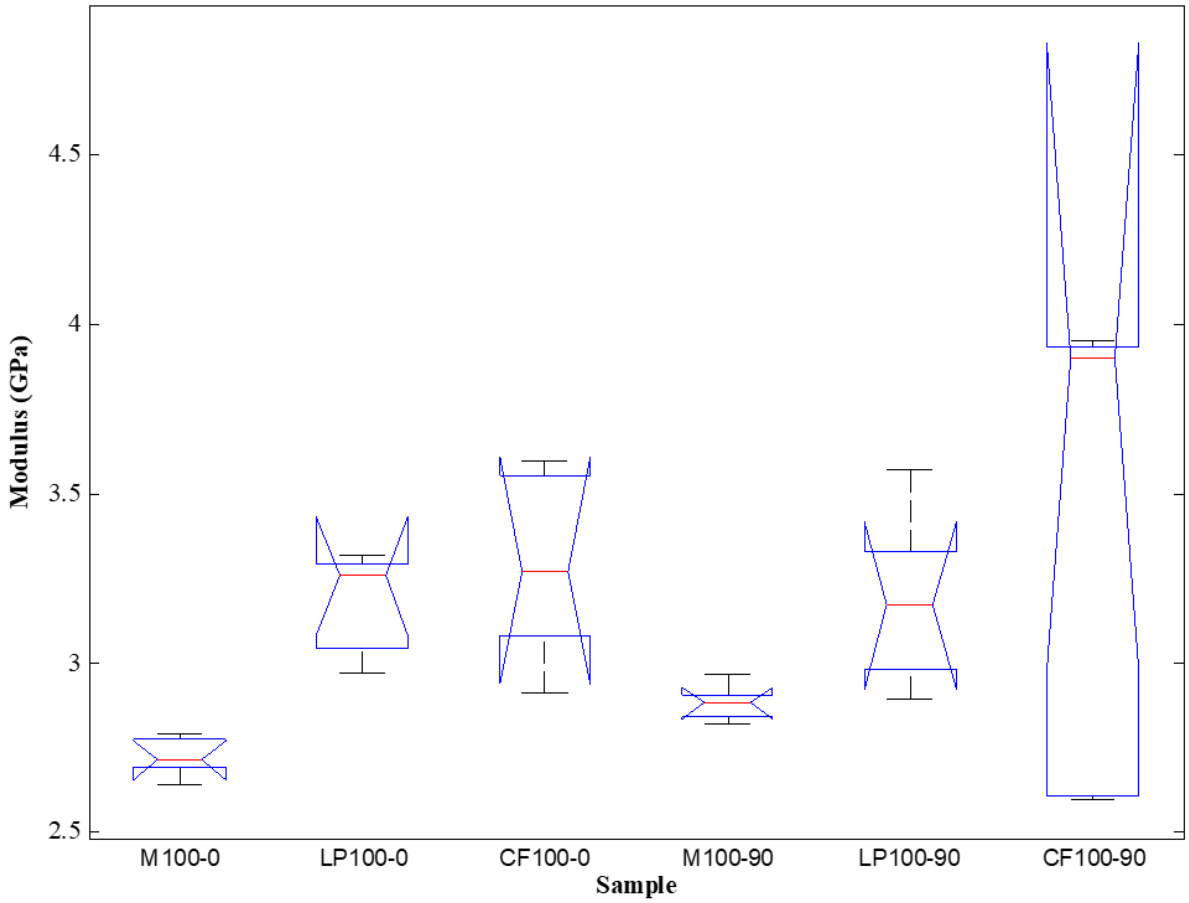

Figure 5.21: Box plot of ANOVA results for Young's modulus printed at 100 µm layer height.

From the results of the ANOVA testing the p-value of 0.0404 is less than that of 0.05 for the 95% confidence level chosen. This indicates that there is significant differences between at least two the sample groups tested [50]. From Figure 5.21, a visual determination can be made to determine which groups differ, and that there is some separation between the means of the samples, but with most of the notches overlapping. This is again due to the large standard of deviation, and therefore large spread in data of the CF100-90 samples. The summarized results of the Tukey test for the 100 µm layer height sample groups that showed significant differences are shown in Table 5.20, with the full Tukey results in APPENDIX B, Table B.6.

Table 5.20: Tukey HSD results for Young's modulus printed at 100 μm layer height.

Compared Pairs	Tukey HSD Q statistic	Tukey HSD p-value	Tukey HSD inference
M100-0 vs CF100-90	4.3934	0.0484687	$p<0.05$

While the Tukey results only should a difference between the M100-0 and CF 100-90, if the deviation of the CF 100-90 sample could be reduced it might have showed a difference between all of the other groups. The higher median of the CF100-90 than that of the CF 100-0 also shows that at layer heights larger than the average fiber length isotropic parts possibly could be produced. If fiber was being aligned more in plane with the printing surface it would be expected that the properties would have been lower than the CF 100-0 results [13].

The results for the ANOVA analysis when comparing samples printed at a 100 μm layer height are summarized in Table 5.21, with the full ANOVA results in Table B.7 in APPENDIX B.

Table 5.21: ANOVA summary for Young's modulus printed at 50 μm layer height.

Source of Variation	Sum of Squares	Degrees of Freedom	Mean Square	F-Statistic	P-value	F-Critical
Between Groups	1.49	5	0.298	8.31	$1.13*10^{-4}$	2.62
Within Groups	0.86	24	0.0358	-	-	-

The ANOVA result were also plotted in MatLab as notched box plots for visual examination of the data, and is shown in Figure 5.22.

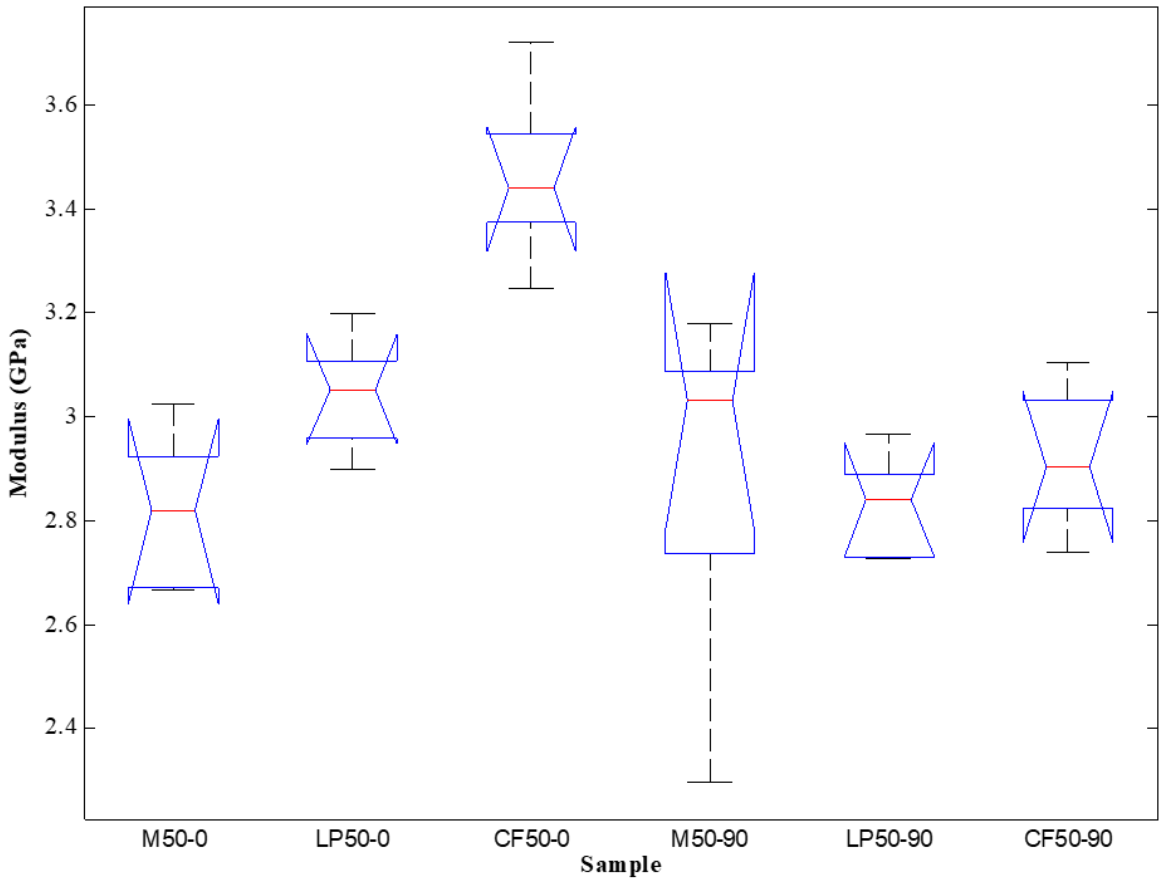

Figure 5.22: Box plot of ANOVA results for Young's modulus printed at 50 μm layer height.

From the results of the ANOVA testing the p-value of $1.13*10^{-4}$ is less than that of 0.05 for the 95% confidence level chosen. This indicates that there is significant differences between at least two of the sample groups tested [50]. From Figure 5.22, there is some separation between the means of the samples, but most of the notches overlap with CF50-0 showing the greatest difference. The summarized results of the Tukey test for the 50 μm layer height sample groups that showed significant differences are shown in Table 5.22, with the full Tukey results in APPENDIX B, Table B.8.

Table 5.22: Tukey HSD results for Young's modulus printed at 50 μm layer height.

Treatments Pair	Tukey HSD Q Statistic	Tukey HSD p-value	Tukey HSD Inference
M50-0 vs CF50-0	7.6447	0.0010053	p<0.01
LP50-0 vs CF50-0	4.9642	0.0196729	p<0.05
CF50-0 vs M50-90	6.752	0.0010053	p<0.01
CF50-0 vs LP50-90	7.5148	0.0010053	p<0.01
CF50-0 vs CF50-90	6.3954	0.001736	p<0.01
M50-0 vs CF50-0	7.6447	0.0010053	p<0.01

The CF50-0 shows the greatest difference between the different samples, which is a good indicator that the carbon fiber is working as a reinforcement for the resin. The CF50-90 would be predicted to be lower than the CF50-0 if fiber alignment was as such that the load was being applied out of plane of a special orthotropic composite, it is more likely due to the cracks that were present in the sample as discussed in the previous section [13].

5.2.4.1.2. Tensile Strength

The results for the ultimate tensile strength for the samples were evaluated using ANOVA and if needed a post-hoc Tukey HSD test, as outlined in section 4.3.3.2. The samples were compared across 4 different groups, 0º and 90º print orientation and 100 μm and 50 μm layer heights. The groups analyzed are the same that were used in the statistical analysis for the Young's modulus, and are shown in Table 5.15.

The results for the ANOVA analysis when comparing samples in the 0º print orientation are summarized in Table 5.23, with the full ANOVA results in Table B.9 in APPENDIX B.

Table 5.23: ANOVA summary for tensile strength in 0º print orientation.

Source of Variation	Sum of Squares	Degrees of Freedom	Mean Square	F-Statistic	P-value	F-Critical
Between Groups	1465.0	5	293.0	6.58	$5.515*10^{-4}$	2.62
Within Groups	1069.4	24	44.6	-	-	-

The ANOVA result were also plotted in MatLab as notched box plots for visual examination of the data, and is shown in Figure 5.23.

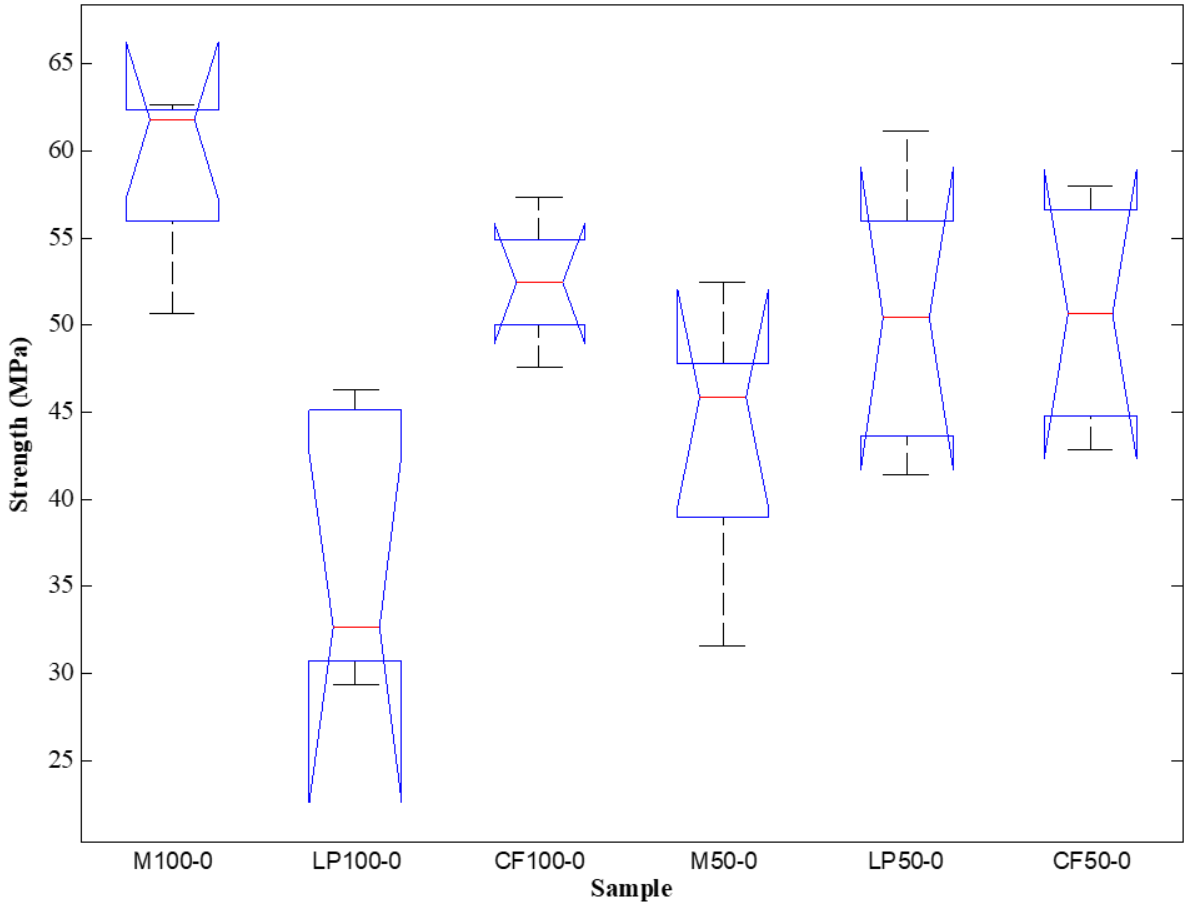

Figure 5.23: Box plot of ANOVA results for tensile strength in 0º print orientation.

From the results of the ANOVA testing the p-value of $5.515*10^{-4}$ is less than that of 0.05 for the 95% confidence level chosen. This indicates that there is significant differences between

the sample groups tested [50]. From Figure 5.23, a visual determination can be made to determine which groups differ, and from these box plots it can be seen that there is some separation between the means of the samples. The summarized results of the Tukey test for the 0º sample groups that showed significant differences are shown in Table 5.24, with the full Tukey results in APPENDIX B, Table B.10.

Table 5.24: Tukey HSD results for tensile strength in 0º print orientation.

Compared Pairs	Tukey HSD Q statistic	Tukey HSD p-value	Tukey HSD inference
M100-0 vs LP100-0	7.4069	0.0010053	p<0.01
M100-0 vs M50-0	5.1935	0.0135044	p<0.05
LP100-0 vs CF100-0	5.2144	0.0130433	p<0.05
LP100-0 vs LP50-0	4.5001	0.0411466	p<0.05
LP100-0 vs CF50-0	4.5967	0.0353984	p<0.05

As discussed in section 5.2.4.1, the samples printed in the 0º orientation strengths are lowered by the defects left from removal of the support material, and the cracks present in the LP100 and LP50 samples. The samples printed in the 90º print orientation are better representations of the neat Moai resin strength.

The results for the ANOVA analysis when comparing samples in the 90º print orientation are summarized in Table 5.25, with the full ANOVA results in Table B.11 in APPENDIX B.

Table 5.25: ANOVA summary for tensile strength in 90º print orientation.

Source of Variation	Sum of Squares	Degrees of Freedom	Mean Square	F-Statistic	P-value	F-Critical
Between Groups	14521.5	5	2904.3	31.17	$9.49*10^{-10}$	2.62
Within Groups	2236.1	24	93.2	-	-	-

The ANOVA result were also plotted in MatLab as box plots for visual examination of the data, and is shown in Figure 5.24.

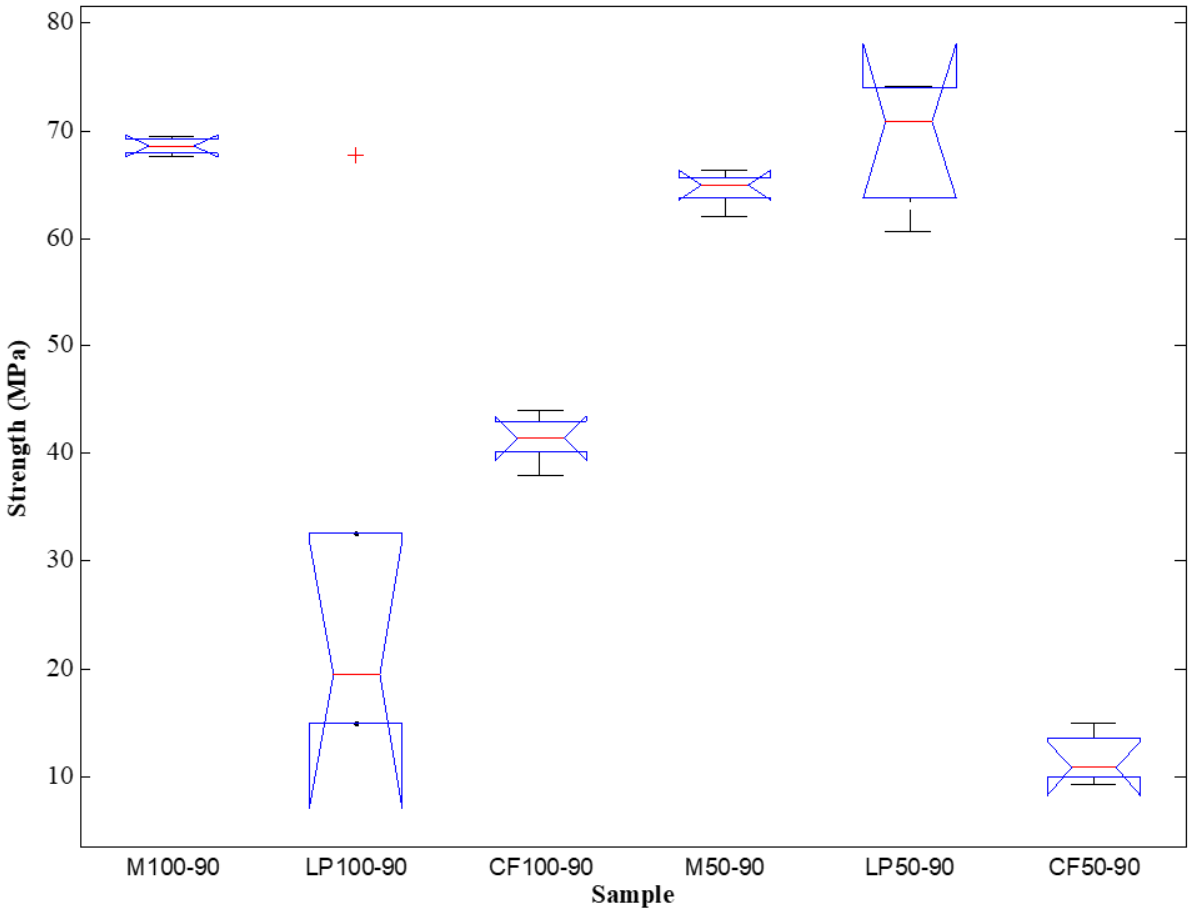

Figure 5.24: Box plot of ANOVA results for tensile strength in 90º print orientation.

From the results of the ANOVA testing the p-value of $9.49*10^{-10}$ is less than that of 0.05 for the 95% confidence level chosen. This indicates that there is significant difference between the sample groups tested [50]. From Figure 5.24, many of the sample means do not overlap, but the red cross present above LP100-90 is an indication of an outlier. Although it is an outlier it is most likely a better reflation of the strength of the LP-100 sample. This is due to all the cracks that were present in the samples with just Luperox P added, but was not as prevalent in the specimen that produced that data point. In Figure 5.24, the size of the confidence interval (notches) are smaller than what is seen in Figure 5.23 due to the defects of the supports not being present on the specimens. The summarized results of the Tukey test for the 90º sample groups

that showed significant differences are shown in Table 5.26, with the full Tukey results in APPENDIX B, Table B.12.

Table 5.26: Tukey HSD results for tensile strength in 90º print orientation.

Treatments Pair	Tukey HSD Q Statistic	Tukey HSD p-value	Tukey HSD Inference
M100-90 vs LP100-90	9.473	0.0010053	p<0.01
M100-90 vs CF100-90	6.2817	0.0021166	p<0.01
M100-90 vs CF50-90	13.1663	0.0010053	p<0.01
LP100-90 vs M50-90	8.5619	0.0010053	p<0.01
LP100-90 vs LP50-90	9.5533	0.0010053	p<0.01
CF100-90 vs M50-90	5.3706	0.0100509	p<0.05
CF100-90 vs LP50-90	6.362	0.0018398	p<0.01
CF100-90 vs CF50-90	6.8846	0.0010053	p<0.01
M50-90 vs CF50-90	12.2552	0.0010053	p<0.01
LP50-90 vs CF50-90	13.2466	0.0010053	p<0.01

The lower strength of the carbon fiber and Luperox samples when compared to the Moai resin have been discussed in the previous section 5.2.4.1, and are a result of poor interface strength and stress concentration effects.

The results for the ANOVA analysis when comparing samples printed at a 100 μm layer height are summarized in Table 5.27, with the full ANOVA results in Table B.13, in APPENDIX B.

Table 5.27: ANOVA summary for tensile strength printed at 100 μm layer height.

Source of Variation	Sum of Squares	Degrees of Freedom	Mean Square	F-Statistic	P-value	F-Critical
Between Groups	5714.6	5	1142.9	11.08	$1.29*10^{-5}$	2.62
Within Groups	2474.7	24	103.1	-	-	-

The ANOVA result were also plotted in MatLab as notched box plots for visual examination of the data, and is shown in Figure 5.25.

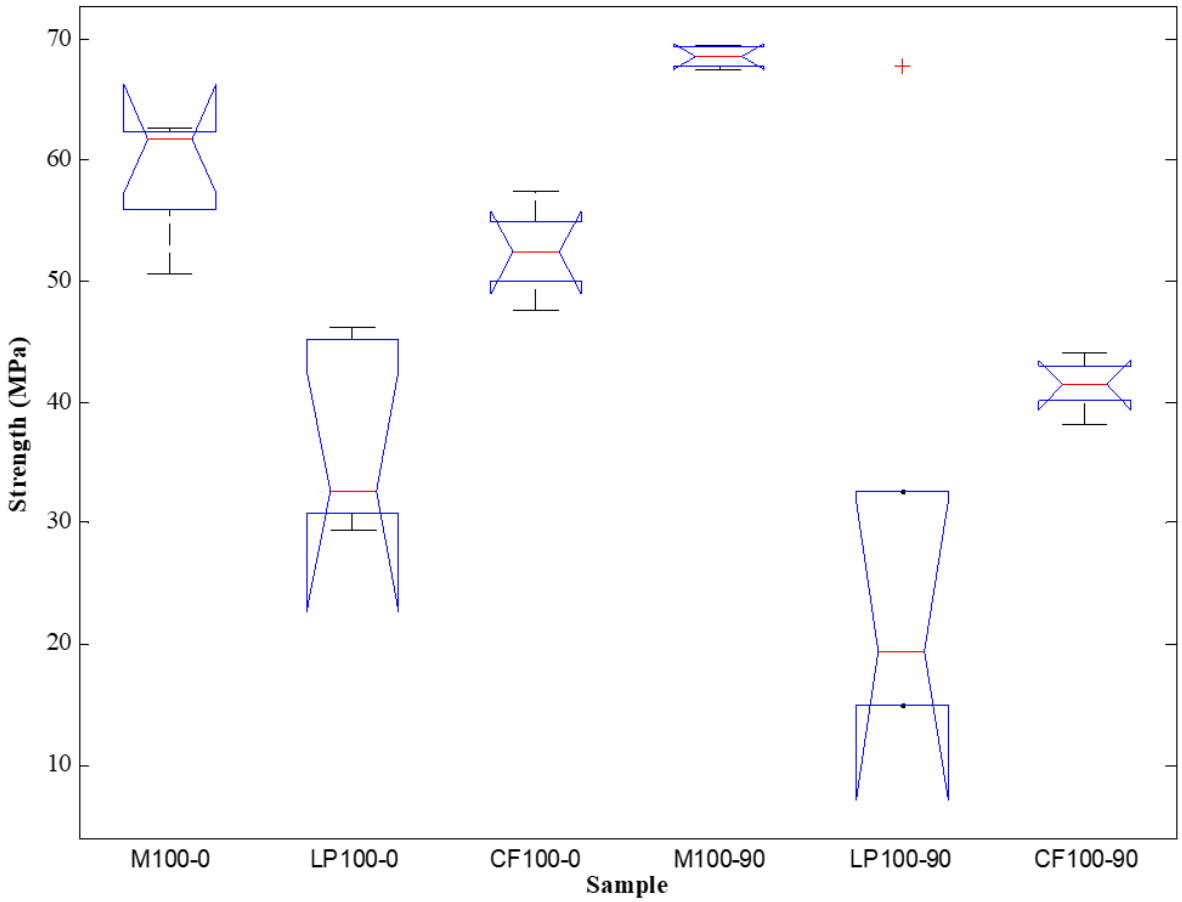

Figure 5.25: Box plot of ANOVA results for tensile strength printed at 100 μm layer height.

From the results of the ANOVA testing the p-value of $1.29*10^{-5}$ is less than that of 0.05 for the 95% confidence level chosen. This indicates that there is significant differences between at least two of the sample groups tested [50]. From Figure 5.25, there is separation between the many of the means of the samples, with the outlier from LP50-90 present again. The summarized results of the Tukey test for the 100 μm layer height sample groups that showed significant differences are shown in Table 5.28, with the full Tukey results in APPENDIX B, Table B.14.

Table 5.28: Tukey HSD results for tensile strength printed at 100 μm layer height.

Compared Pairs	Tukey HSD Q statistic	Tukey HSD p-value	Tukey HSD inference
M100-0 vs LP100-0	4.8691	0.0229462	p<0.05
M100-0 vs LP100-90	6.9028	0.0010053	p<0.01
LP100-0 vs M100-90	6.9711	0.0010053	p<0.01
CF100-0 vs LP100-90	5.4615	0.0086307	p<0.01
M100-90 vs LP100-90	9.0048	0.0010053	p<0.01
M100-90 vs CF100-90	5.9712	0.0036196	p<0.01

Again the Moai resin samples have a higher strength, but the carbon fiber reinforced samples for both the 0º and 90º print orientation are not statistically different. This helps demonstrates that for a layer height larger than the length of the fiber an isotropic part could be manufactured.

The results for the ANOVA analysis when comparing samples printed at a 50 μm layer height are summarized in Table 5.29, with the full ANOVA results in Table B.15 in APPENDIX B.

Table 5.29: ANOVA summary for tensile strength at 50 μm layer height.

Source of Variation	Sum of Squares	Degrees of Freedom	Mean Square	F-Statistic	P-value	F-Critical
Between Groups	10307.4	5	2061.5	59.55	$9.67*10^{-13}$	2.62
Within Groups	830.8	24	34.6	-	-	-

The ANOVA result were also plotted in MatLab as notched box plots for visual examination of the data, and is shown in Figure 5.26.

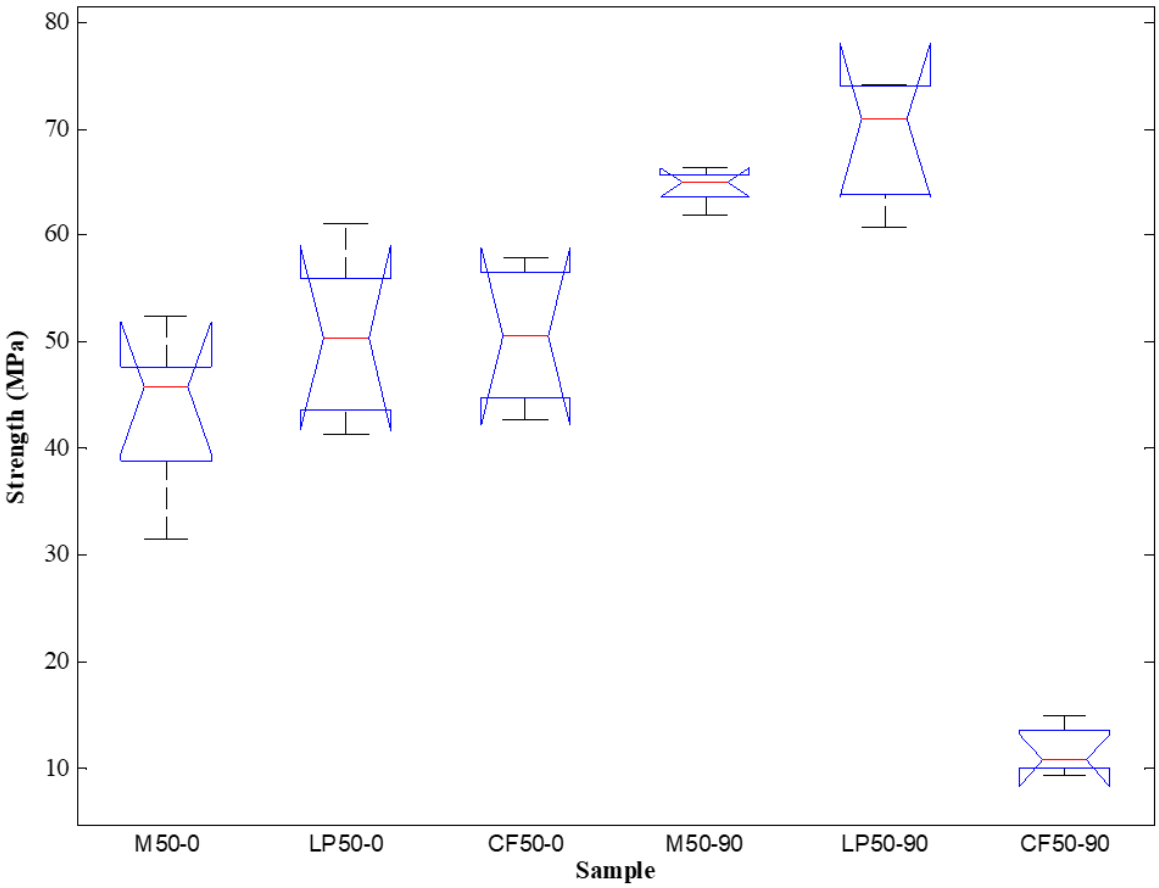

Figure 5.26: Box plot of ANOVA results for tensile strength printed at 50 µm layer height.

From the results of the ANOVA testing the p-value of $9.67*10^{-13}$ is less than that of 0.05 for the 95% confidence level chosen. This indicates that there is significant differences between the sample groups compared [50]. From Figure 5.26, while the CF50-0 looks to be of the same strength as the M50-0, but the values could be affected due to the support material defects being present in the specimens. The summarized results of the Tukey test for the 50 µm layer height sample groups that showed significant differences are shown in Table 5.30, with the full Tukey results in APPENDIX B, Table B.16.

Table 5.30: Tukey HSD results for tensile strength printed at 50 μm layer height.

Treatments Pair	Tukey HSD Q Statistic	Tukey HSD p-value	Tukey HSD Inference
M50-0 vs M50-90	8.0251	0.0010053	p<0.01
M50-0 vs LP50-90	9.6515	0.0010053	p<0.01
M50-0 vs CF50-90	12.0803	0.0010053	p<0.01
LP50-0 vs M50-90	5.4311	0.0090823	p<0.01
LP50-0 vs LP50-90	7.0574	0.0010053	p<0.01
LP50-0 vs CF50-90	14.6744	0.0010053	p<0.01
CF50-0 vs M50-90	5.3215	0.0109131	p<0.05
CF50-0 vs LP50-90	6.9478	0.0010053	p<0.01
CF50-0 vs CF50-90	14.784	0.0010053	p<0.01
M50-0 vs LP50-0	20.1054	0.0010053	p<0.01
M50-0 vs CF50-0	21.7318	0.0010053	p<0.01

The poor results from the CF50-90 causes a larger difference between the groups then would otherwise be present, but the trend of the 90º oriented parts having higher strengths is still present for the other samples, from the support material not being present in the gage section.

5.2.4.2. Flexural Testing

A short-fiber composite resin consisting of the milled and sieved Toray T-700 carbon fiber at a fiber volume of 5%, Luperox P at 0.5 wt.%, and Moai resin was prepared as detailed in section 4.2.1. Flexural samples were manufactured and prepared as per sections 4.2.2, 4.2.3, and 4.3.4.1. The flexural testing was carried out as described in section 4.3.4.1, with the exception the test numbers 4,8,12, and 16 from Table 4.10 were left out. The test numbers omitted represent the samples made with carbon fiber and no thermal initiator which was shown as ineffective in section 5.1.1. The settings changed from default for the Moai printer are the same that were used in Table 5.5 unless otherwise stated. As in section 5.2.4.1, a thin layer of neat Moai resin to the print bed before starting the print aided in keeping the part fixed to the bed during the printing process. With the same naming convention used for the samples as shown in Table 5.12.

The maximum flexural strength and flexural modulus was found as specified in ASTM D790 section 12.2 and 12.5 respectively, and the results are shown in Figure 5.27, Figure 5.28, Figure 5.29, and Figure 5.30, and summarized in Table 5.31 [53]. The results for the samples printed in the 0º orientation are shown in Figure 5.27 and Figure 5.28, for the flexural strength and flexural modulus respectively, and for the samples printed in the 90º shown in Figure 5.29 and Figure 5.30, for the flexural strength and flexural modulus respectively.

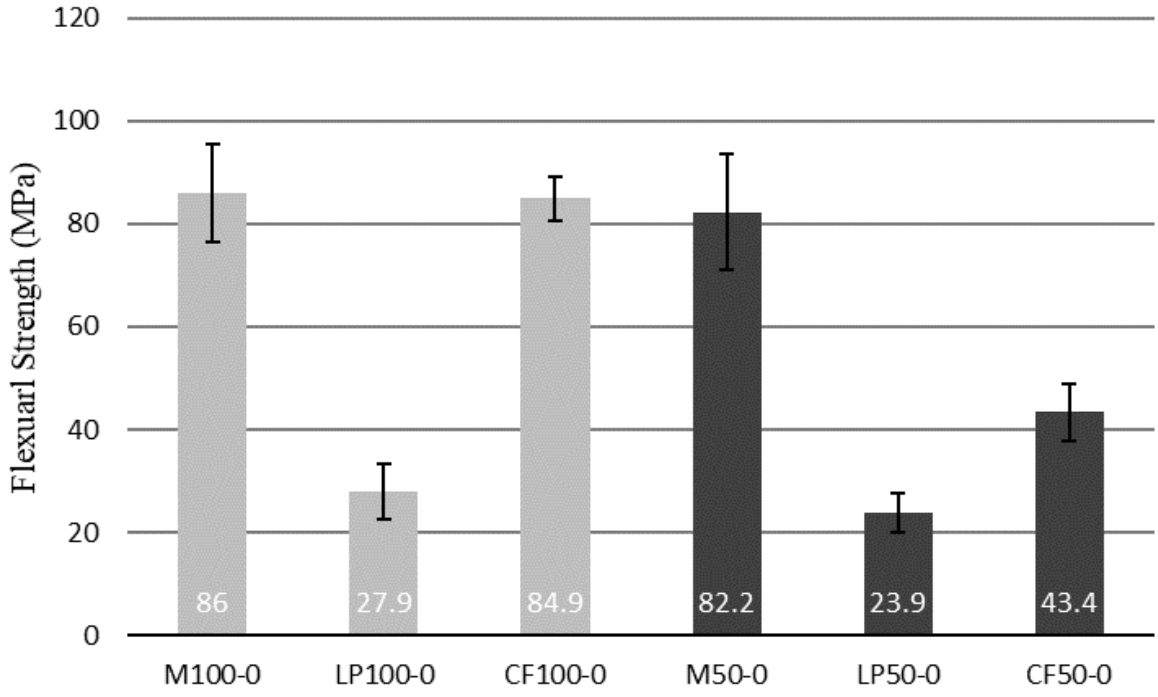

Figure 5.27: Flexural strength results for 0º print orientation.

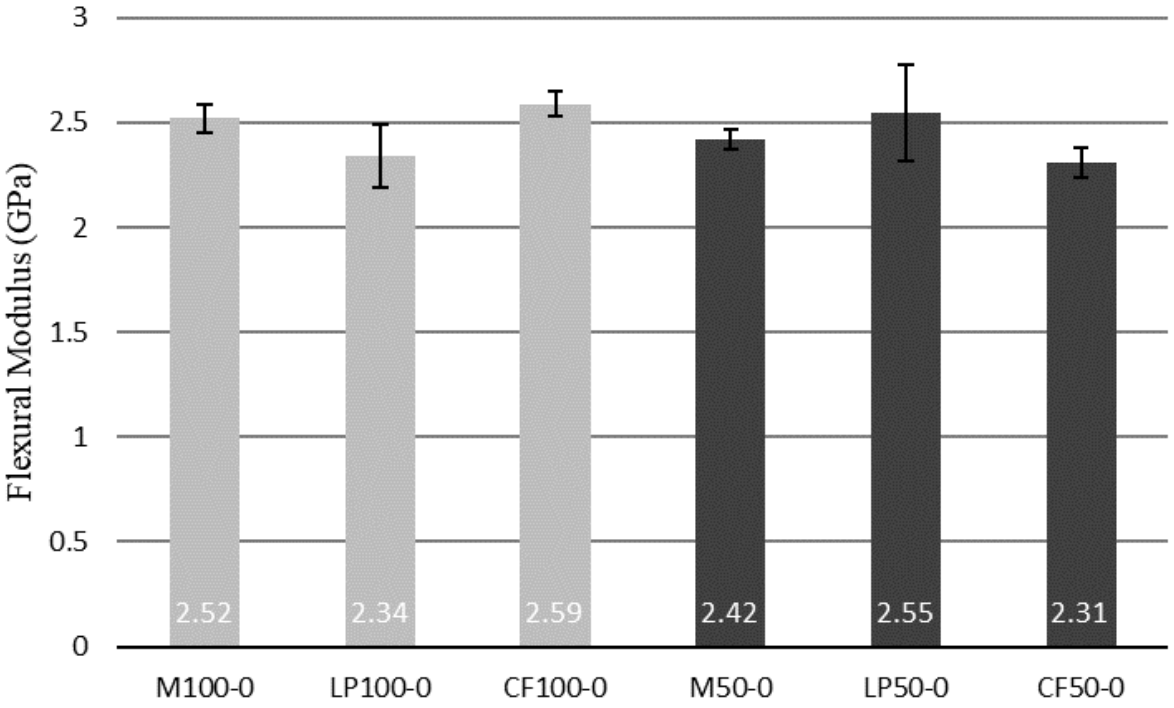

Figure 5.28: Flexural modulus results for 0º print orientation.

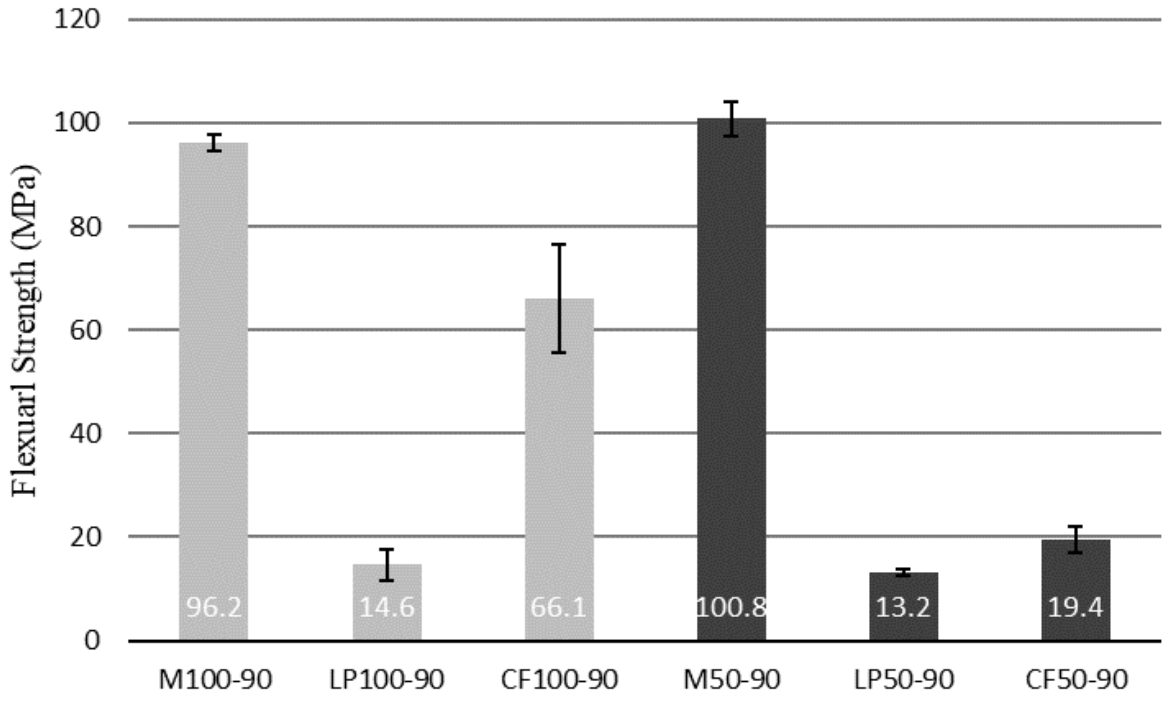

Figure 5.29: Flexural stregnth results for 90º print orientation.

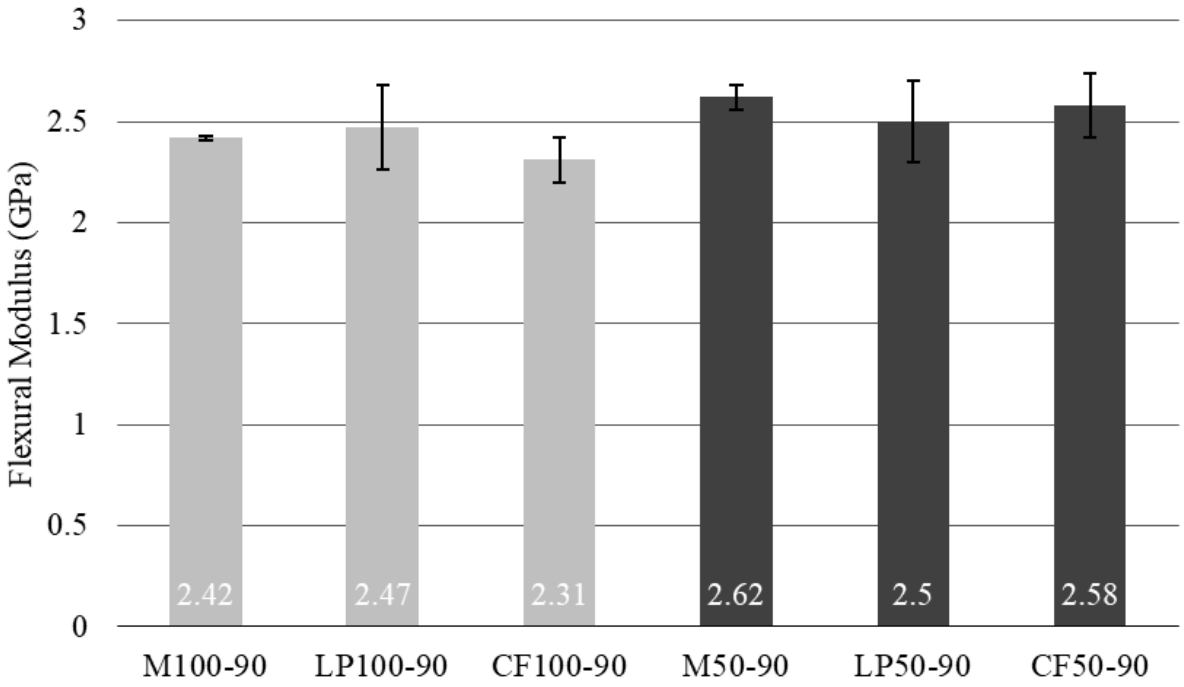

Figure 5.30: Flexural modulus results for 90º print orientation.

Table 5.31: Summarized flexural testing results.

Sample	Layer Height (µm)	Print Orientation	Fiber Volume (%)	Flexural Strength (MPa)	Flexural Modulus (GPa)
M100-0	100	0°	0	86.0 ± 9.5	2.52 ± 0.07
M100-90	100	90º	0	96.2 ± 1.7	2.42 ± 0.01
M50-0	50	0°	0	82.2 ± 11.2	2.42 ± 0.05
M50-90	50	90º	0	100.8 ± 3.4	2.62 ± 0.06
LP100-0	100	0°	0	27.9 ± 5.4	2.34 ± 0.15
LP100-90	100	90º	0	14.6 ± 3.0	2.47 ± 0.21
LP50-0	50	0°	0	23.9 ± 3.7	2.55 ± 0.23
LP50-90	50	90º	0	13.2 ± 0.6	2.50 ± 0.20
CF100-0	100	0°	5	84.9 ± 4.3	2.59 ± 0.06
CF100-90	100	90º	5	66.1 ± 10.5	2.31 ± 0.11
CF50-0	50	0°	5	43.4 ± 5.5	2.64 ± 0.12
CF50-90	50	90º	5	19.4 ± 2.5	2.58 ± 0.16

Overall the flexural modulus of the samples were not improved by the addition of the carbon fiber. This could be primarily due to the lower fiber volume (5%) of the samples, causing them to have results similar to that of the neat resin samples. During the flexural testing the specimens are subjected to the more complex stress state (compressive, tensile, and shear) when

compared to the previous tensile stress state from the axial testing in section 5.2.4.1 [63, 64]. This is even more pronounced due to the fiber volume gradient that was found (section 5.2.3.1) to be present with in the flexural testing. With the tensile specimens, the gage section where the extensometer was attached, and reading the strain during testing, had similar fiber volume amount within the measured section. While with the flexural specimens, almost the whole specimen (with in the span length) is subjected to testing at the same time, with the lower fiber volume on one end of the specimen having a stiffness similar to that of the neat Moai resin samples.

For the flexural testing the samples are subjected to compressive, tensile, and shear stresses that lead to the multiple failure mechanisms effecting the flexural properties of material [64]. The tensile stresses can lead to fiber breakage and debonding, while compressive stresses can lead to fiber shear and/or buckling and kinking [64]. As was discussed before in section 5.2.4.1 the fibers exhibited characteristics indicating poor interfacial strength between the fiber and matrix. This along with the low fiber content and weak shear properties of carbon fiber would lead the failure of the flexural testing to coincide more with that of the compressive type failures, which are governed more by the matrix properties [13, 63, 64].

The samples made with just Luperox P added showed the same type of surface cracking after post-curing as was seen in the tensile samples. This lead to them have the weakened flexural strength as was seen in the tensile samples made of the same constituents. The carbon fiber samples exhibited poorer flexural strength than the neat Moai resin samples due to the effects of the fiber ends acting as stress concentration, weak interfacial properties, low fiber content, and the presents of voids [13]. The CF50-90 samples also had the same cracking

between layers as was seen in the same sample group from the tensile testing (Figure 5.17) from the printing process, but was not as sever in terms of the depth of the cracks.

The statistical analysis for the flexural testing results for the flexural modulus and flexural strength of the evaluated materials is looked at in the following two sections, as outlined in section 4.3.4.2.

5.2.4.2.1. Flexural Modulus

The results for the Flexural modulus for the samples tested were evaluated using ANOVA and if needed a post-hoc Tukey HSD test, as outlined in section 4.3.4.2. They were compared across 4 different groups these were, 0º and 90º print orientation and 100 μm and 50 μm layer heights. The groups analyzed are the same that were used for the analysis of the Young's modulus from the tensile testing, and are shown in Table 5.15.

The results for the ANOVA analysis when comparing samples in the 0º print orientation are summarized in Table 5.32, with the full ANOVA results in Table B.17 in APPENDIX B.

Table 5.32: ANOVA summary for flexural modulus in 0º print orientation.

Source of Variation	Sum of Squares	Degrees of Freedom	Mean Square	F-Statistic	P-value	F-Critical
Between Groups	0.647	5	0.129	8.76	$7.78*10^{-5}$	2.62
Within Groups	0.355	24	0.0148			

The ANOVA result were also plotted in MatLab as notched box plots for visual examination of the data, and is shown in Figure 5.31.

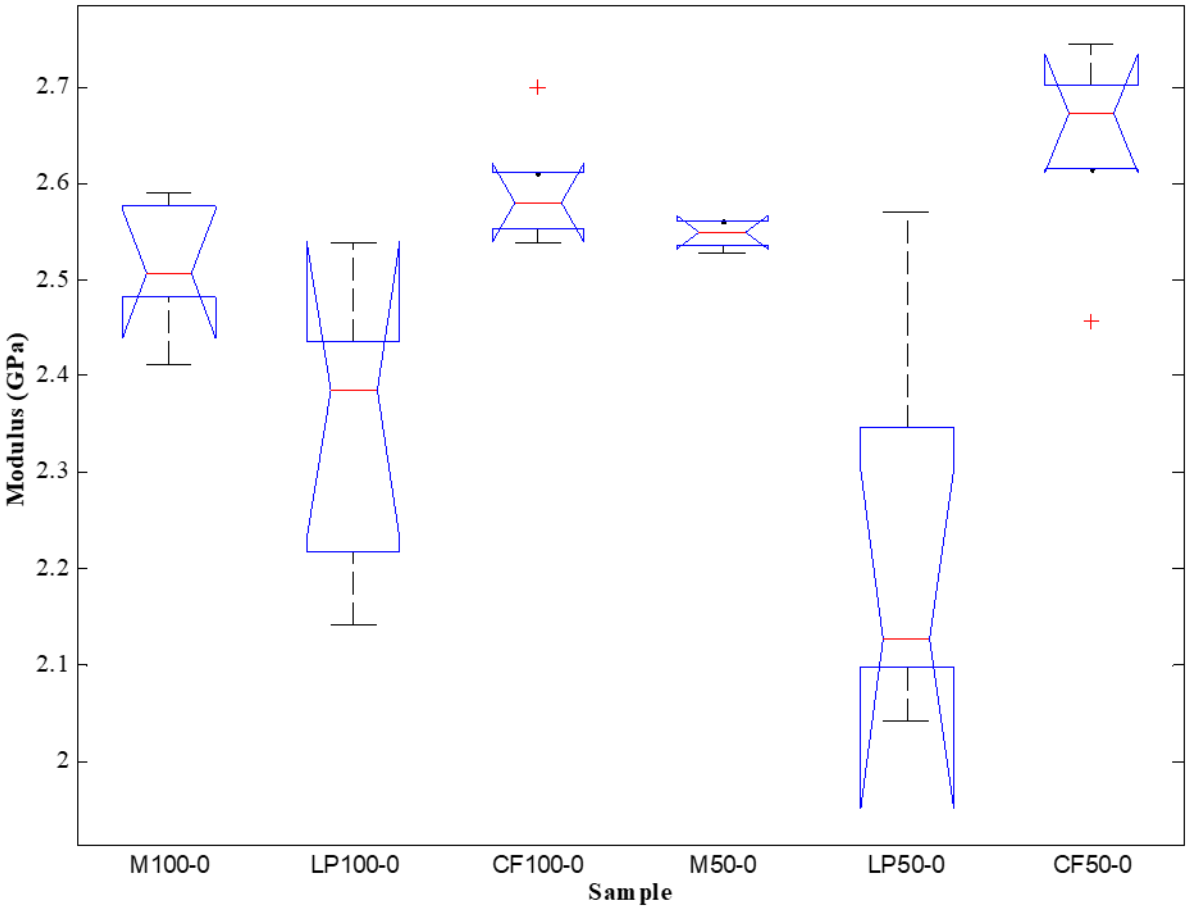

Figure 5.31: Box plot of ANOVA results for flexural modulus in 0º print orientation.

From the results of the ANOVA testing the p-value of $7.78*10^{-5}$ is less than that of 0.05 for the 95% confidence level chosen. This indicates that there is significant differences between at least two of the sample groups tested [50]. From Figure 5.31, a visual determination can be made to determine which groups differ, and can be seen that there is some separation between the means of the samples. The summarized results of the Tukey test for the 0º sample groups that showed significant differences are shown in Table 5.33, with the full Tukey results in APPENDIX B, Table B.18.

Table 5.33: Tukey HSD results for flexural modulus in 0º print orientation.

Compared Pairs	Tukey HSD Q statistic	Tukey HSD p-value	Tukey HSD inference
M100-0 vs LP50-0	5.3509	0.010389	p<0.05
LP100-0 vs CF100-0	4.5896	0.0357898	p<0.05
LP100-0 vs CF50-0	5.5862	0.0069875	p<0.01
CF100-0 vs LP50-0	6.7263	0.0010053	p<0.01
M50-0 vs LP50-0	5.9136	0.0039968	p<0.01
LP50-0 vs CF50-0	7.7229	0.0010053	p<0.01

The LP samples had a lower modulus due to the increased compliance of the specimens from the cracks being present [44]. While the CF50-0 sample did not show any significant difference when compared to the neat Moai resin samples, the higher median and mean value when compared to the CF100-0 in the box plot indicates that the smaller layer height is aligning some fibers. There was also outliers present in both the CF100-0 and CF50-0 samples indicating that the sample manufacturing process could be improved for better consistency [50].

The results for the ANOVA analysis when comparing samples in the 90º print orientation are summarized in Table 5.34, with the full ANOVA results in Table B.27 in APPENDIX B.

Table 5.34: ANOVA summary for flexural modulus in 90º print orientation.

Source of Variation	Sum of Squares	Degrees of Freedom	Mean Square	F-Statistic	P-value	F-Critical
Between Groups	0.326	5	0.0652	4.52	$4.82*10^{-3}$	2.62
Within Groups	0.347	24	0.0144			

The ANOVA result were also plotted in MatLab as notched box plots for visual examination of the data, and is shown in Figure 5.32.

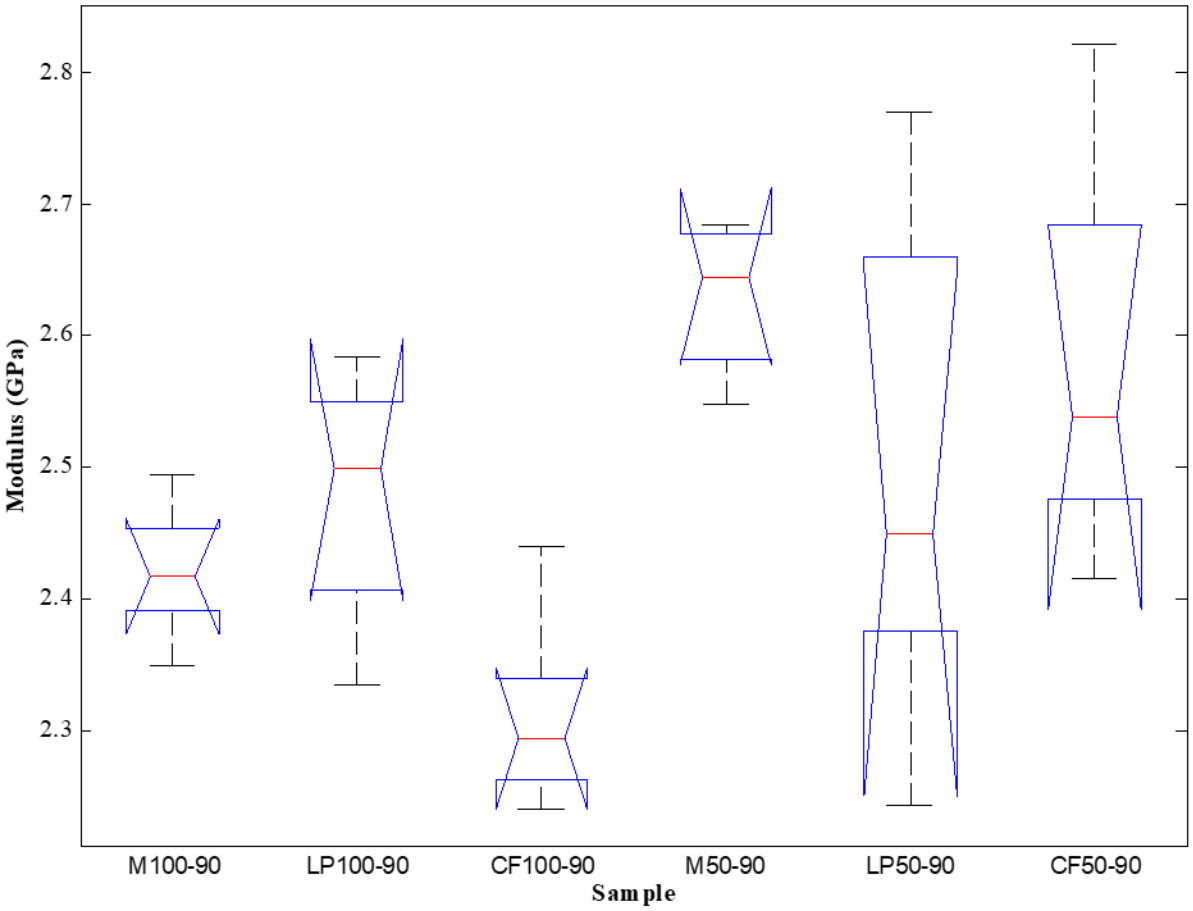

Figure 5.32: Box plot of ANOVA results for flexural modulus in 90º print orientation.

From the results of the ANOVA testing the p-value of $4.82*10^{-3}$ is less than that of 0.05 for the 95% confidence level chosen. This indicates that there is significant differences between at least two of the sample groups tested [50]. From Figure 5.31, a visual determination can be made to determine which groups differ, and can be seen that there is some separation between the means of the samples of the CF100-90. The summarized results of the Tukey test for the 0º sample groups that showed significant differences are shown in Table 5.35, with the full Tukey results in APPENDIX B, Table B.20.

Table 5.35: Tukey HSD results for flexural modulus in 90º print orientation.

Treatments Pair	Tukey HSD Q Statistic	Tukey HSD p-value	Tukey HSD Inference
CF100-90 vs M50-90	5.9428	0.0037998	$p<0.01$
CF100-90 vs CF50-90	5.0608	0.0168014	$p<0.05$

The Tukey HSD results showed only a difference for the CF100-90 specimen due to their lower flexural modulus. The flexural modulus would be expected to be similar to that of the CF100-0 sample, but showed a 13% decrease. This could be due to the inconsistency in the fiber distribution, or due to some fiber alignment occurring and causing the sample to have a decreased modulus.

The results for the ANOVA analysis when comparing samples printed at a 100 μm layer height are summarized in Table 5.36, with the full ANOVA results in Table B.21 in APPENDIX B.

Table 5.36: ANOVA summary for flexural modulus printed at 100 μm layer height.

Source of Variation	Sum of Squares	Degrees of Freedom	Mean Square	F-Statistic	P-value	F-Critical
Between Groups	0.331	5	0.0661	4.18	$7.09*10^{-3}$	2.62
Within Groups	0.379	24	0.0158			

The ANOVA result were also plotted in MatLab as notched box plots for visual examination of the data, and is shown in Figure 5.33.

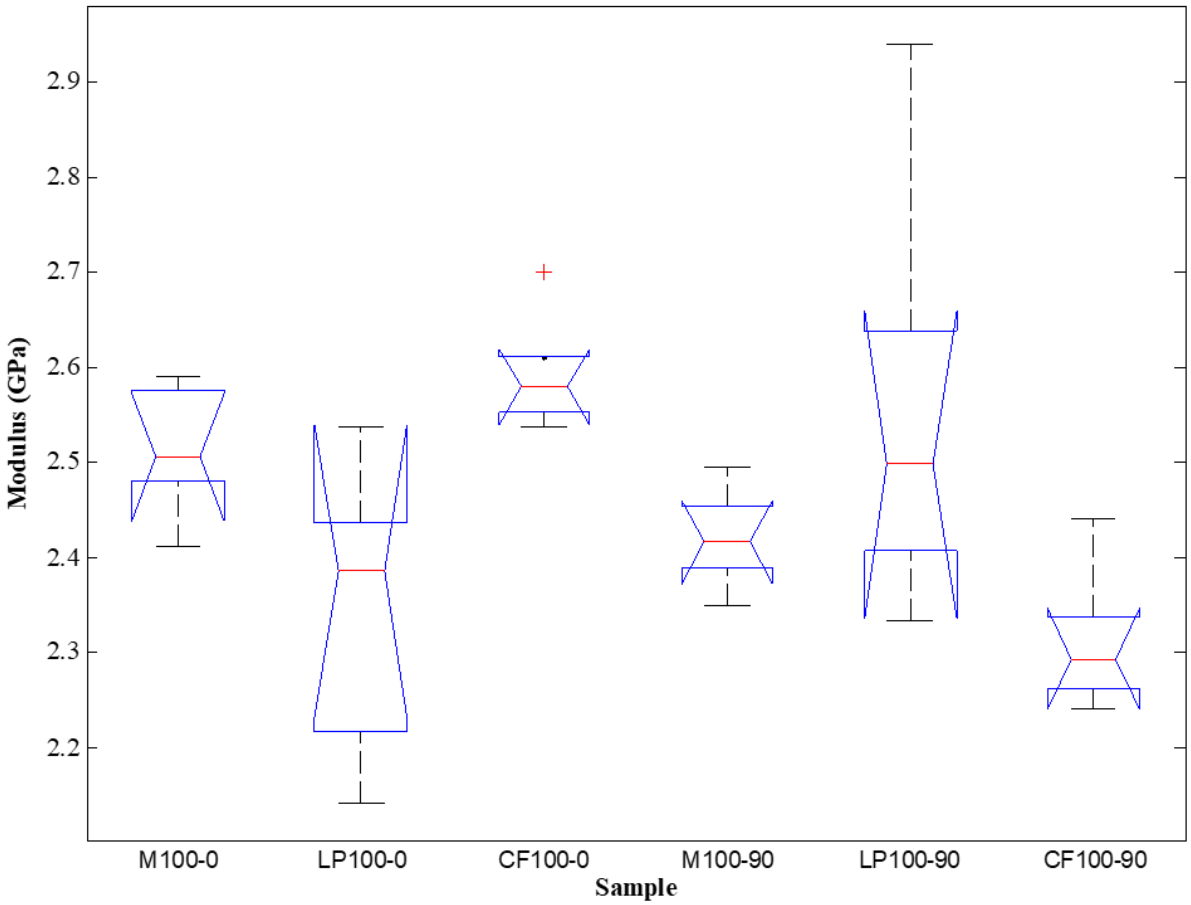

Figure 5.33: Box plot of ANOVA results for flexural modulus printed at 100 μm layer height.

From the results of the ANOVA testing the p-value of $7.09*10^{-3}$ is less than that of 0.05 for the 95% confidence level chosen. This indicates that there is significant differences between at least two of the sample groups tested [50]. From Figure 5.33 a visual determination can be made to determine which groups differ, and that there is some separation between the samples, but most of the notches overlap. This is impart due to the lager standard of deviation, and therefore large spread in data, of the CF100-90 samples. The summarized results of the Tukey test for the 100 μm layer height sample groups that showed significant differences are shown in Table 5.37, with the full Tukey results in APPENDIX B, Table B.22.

Table 5.37: Tukey HSD results for flexural modulus printed at 100 μm layer height.

Compared Pairs	Tukey HSD Q statistic	Tukey HSD p-value	Tukey HSD inference
LP100-0 vs CF100-0	4.4395	0.0451671	$p<0.05$
CF100-0 vs CF100-90	5.0123	0.0181893	$p<0.05$

The flexural modulus of CF100-0 showed higher stiffness than the CF100-90 although it would be expected that they would show close to the same value, due to the 100 μm layer height. This could be due to the fiber volume gradient being more pronounced in the 90º printed samples when compared to the 0º printed samples. The 90º printed samples would have a gradient that runs long ways across the span from support to support, whereas the 0º printed samples would have a gradient going perpendicular to this, allowing the fiber to have more of an effect increase the stiffness.

The results for the ANOVA analysis when comparing samples printed at a 100 μm layer height are summarized in Table 5.38, with the full ANOVA results in Table B.23 in APPENDIX B.

Table 5.38: ANOVA summary for flexural modulus printed at 50 μm layer height.

Source of Variation	Sum of Squares	Degrees of Freedom	Mean Square	F-Statistic	P-value	F-Critical
Between Groups	0.596	5	0.119	5.73	$1.29*10^{-3}$	2.62
Within Groups	0.499	24	0.0208			

The ANOVA result were also plotted in MatLab as notched box plots for visual examination of the data, and is shown in Figure 5.34.

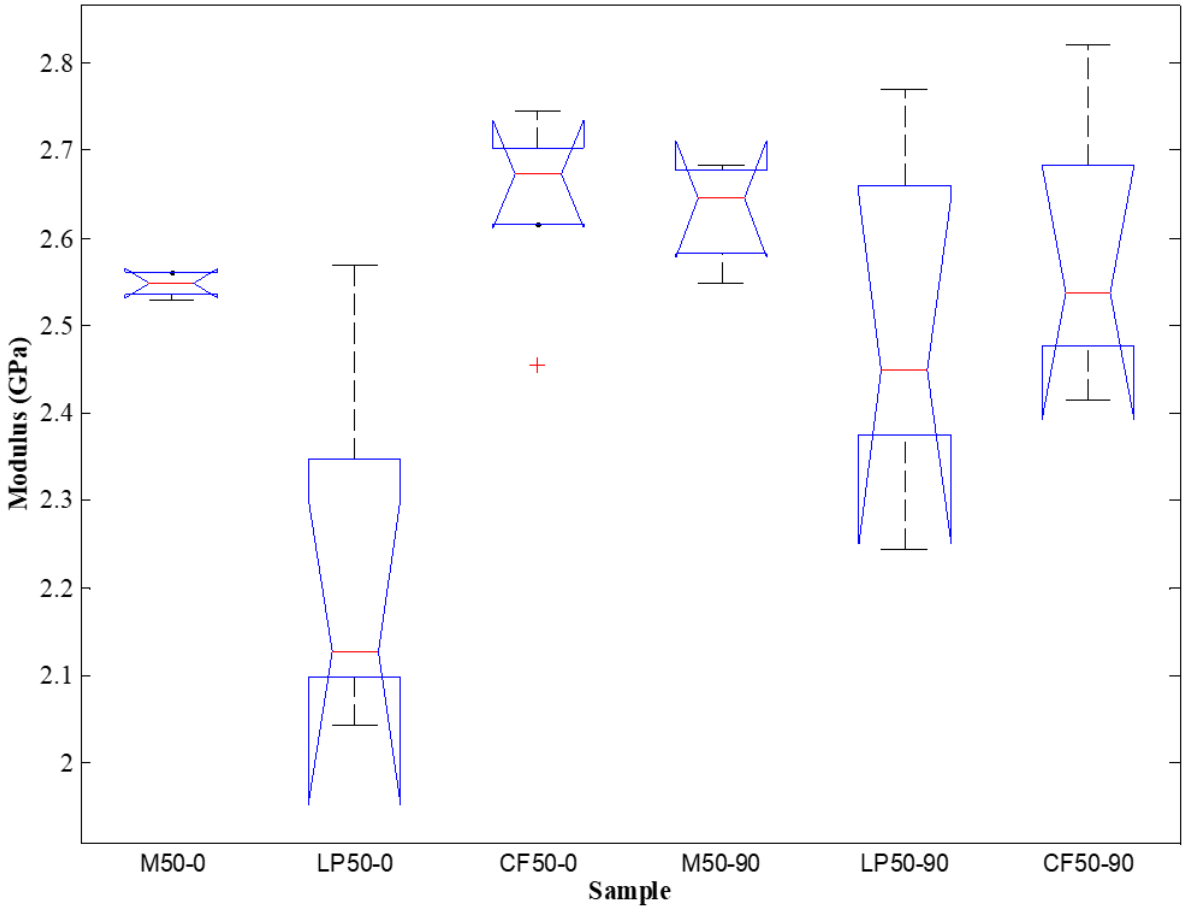

Figure 5.34: Box plot of ANOVA results for flexural modulus printed at 50 μm layer height.

From the results of the ANOVA testing the p-value of $1.29*10^{-3}$ is less than that of 0.05 for the 95% confidence level chosen. This indicates that there is significant differences between at least two of the sample groups tested [50]. From Figure 5.34, a visual determination can be made to determine which groups differ. From these box plots it can be seen that there is some separation between the means of the samples, but most of the notches overlap. The summarized results of the Tukey test for the 50 μm layer height sample groups that showed significant differences are shown in Table 5.39, with the full Tukey results in APPENDIX B, Table B.24.

Table 5.39: Tukey HSD results for flexural modulus printed at 50 μm layer height.

Treatments Pair	Tukey HSD Q Statistic	Tukey HSD p-value	Tukey HSD Inference
M50-0 vs LP50-0	4.986	0.0189857	$p<0.05$
LP50-0 vs CF50-0	6.5116	0.0014191	$p<0.01$
LP50-0 vs M50-90	6.2542	0.0022196	$p<0.01$
LP50-0 vs CF50-90	5.5193	0.0078275	$p<0.01$

From the Tukey HSD results the only groups showing significance difference are the LP50-0 and LP50-90 groups, due to the cracks with in the specimens increasing compliance and therefore decreasing the modulus [44].

5.2.4.2.2. Flexural Strength

The results for the flexural strength for the samples were evaluated using ANOVA and if needed a post-hoc Tukey HSD test, as outlined in section 4.3.4.2. The samples were compared across 4 different groups; 0º and 90º print orientation, and 100 μm and 50 μm layer heights. The groups analyzed are the same that were used in the statistical analysis for the Young's modulus from the tensile testing, and are shown in Table 5.15.

The results for the ANOVA analysis when comparing samples in the 0º print orientation are summarized in Table 5.40, with the full ANOVA results in Table B.25 in APPENDIX B.

Table 5.40: ANOVA summary for flexural strength in 0º print orientation.

Source of Variation	Sum of Squares	Degrees of Freedom	Mean Square	F-Statistic	P-value	F-Critical
Between Groups	2191	5	4382	86.2	$1.57*10^{-14}$	2.62
Within Groups	1220	24	50.9	-	-	-

The ANOVA result were also plotted in MatLab as notched box plots for visual examination of the data, and is shown in Figure 5.35.

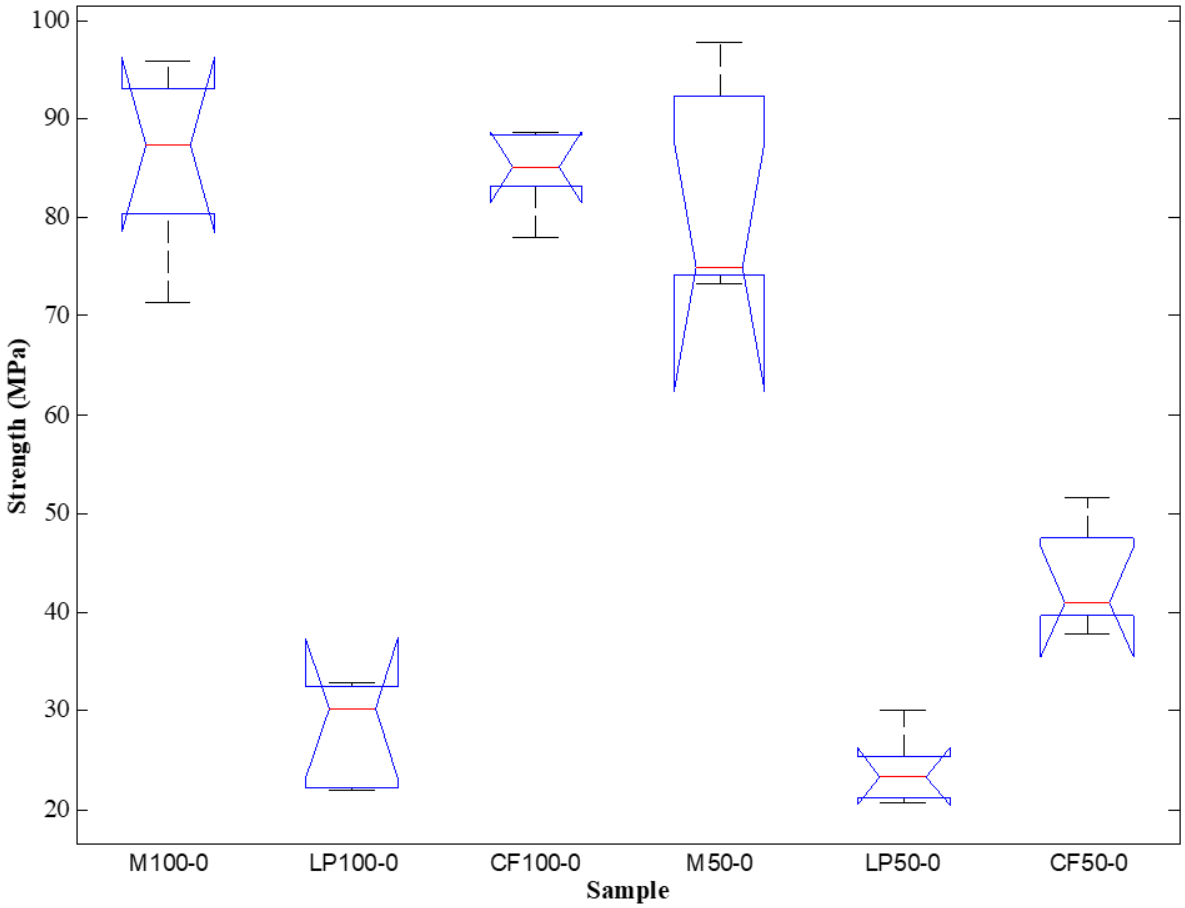

Figure 5.35: Box plot of ANOVA results for flexural strength in 0º print orientation.

From the results of the ANOVA testing the p-value of $1.57*10^{-14}$ is less than that of 0.05 for the 95% confidence level chosen. This indicates that there is significant differences between the sample groups tested [50]. From Figure 5.35, a visual determination can be made to determine which groups differ, and from these box plots it can be seen that there is some separation between the samples. The summarized results of the Tukey test for the 0º sample groups that showed significant differences are shown in Table 5.41, with the full Tukey results in APPENDIX B, Table B.26.

Table 5.41: Tukey HSD results for flexural strength in 0º print orientation.

Compared Pairs	Tukey HSD Q statistic	Tukey HSD p-value	Tukey HSD inference
M100-0 vs LP100-0	18.2173	0.0010053	p<0.01
M100-0 vs LP50-0	19.4936	0.0010053	p<0.01
M100-0 vs CF50-0	13.3789	0.0010053	p<0.01
LP100-0 vs CF100-0	17.8862	0.0010053	p<0.01
LP100-0 vs M50-0	17.0132	0.0010053	p<0.01
LP100-0 vs CF50-0	4.8384	0.0241039	p<0.05
CF100-0 vs LP50-0	19.1624	0.0010053	p<0.01
CF100-0 vs CF50-0	13.0478	0.0010053	p<0.01
M50-0 vs LP50-0	18.2894	0.0010053	p<0.01
M50-0 vs CF50-0	12.1748	0.0010053	p<0.01
LP50-0 vs CF50-0	6.1147	0.002827	p<0.01

While the CF100-0 showed no statistical difference between the neat Moai resin samples, the CF50-0 showed poorer flexural strength when compared to both the CF100-0 and neat Moai resin samples. Ideally there would be alignment of the fibers that should increase the strength, but the presence of voids in the sample, stress concentration due to fiber ends, the fiber volume gradient, or other unseen internal/surface defects could cause the drop in strength seen in the samples [13, 63]. All of the LP samples showed significant difference due to the surface cracking from the post-curing process causing a decrease the strength.

The results for the ANOVA analysis when comparing samples in the 90º print orientation are summarized in Table 5.42, with the full ANOVA results in Table B.27 in APPENDIX B.

Table 5.42: ANOVA summary for flexural strength in 90º print orientation.

Source of Variation	Sum of Squares	Degrees of Freedom	Mean Square	F-Statistic	P-value	F-Critical
Between Groups	42490	5	8497	362	$8.89*10^{-22}$	2.62
Within Groups	563	24	23.5	-	-	-

The ANOVA result were also plotted in MatLab as notched box plots for visual examination of the data, and is shown in Figure 5.36.

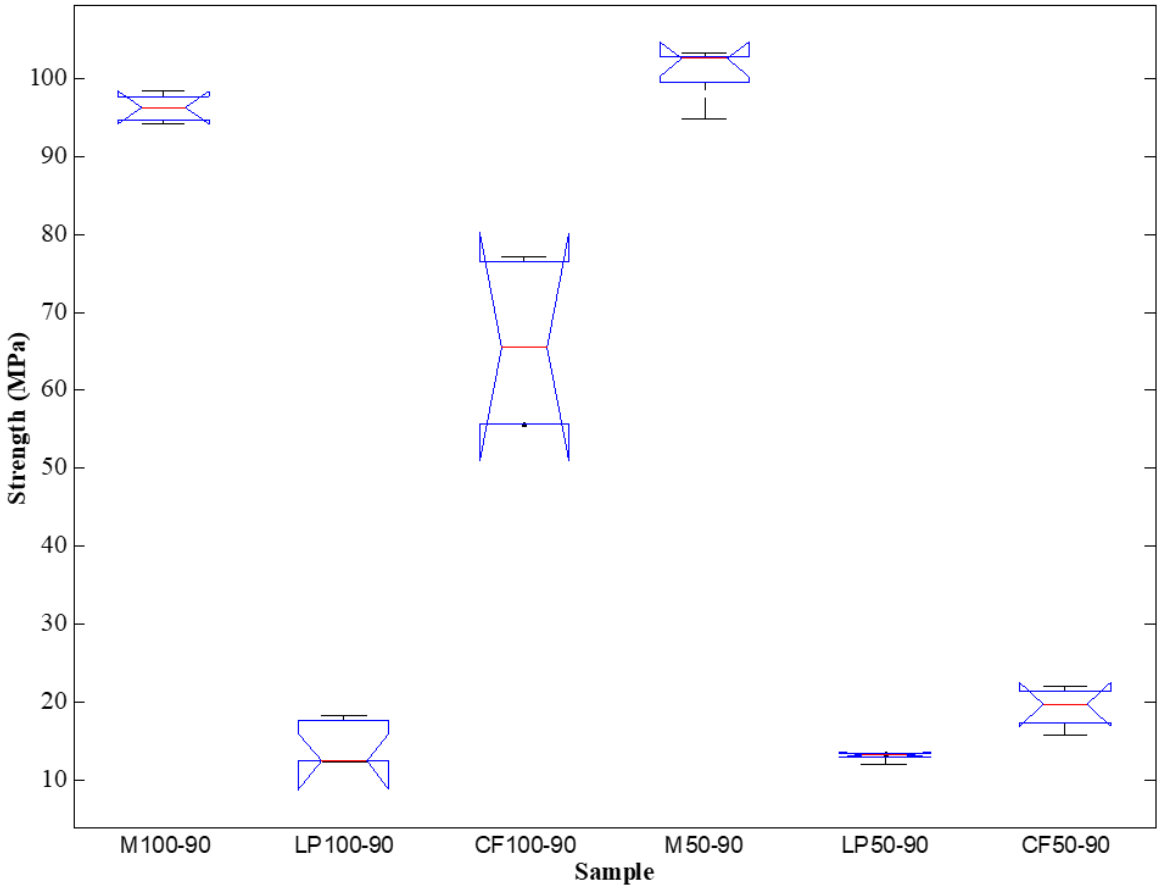

Figure 5.36: Box plot of ANOVA results for flexural strength in 90º print orientation.

From the results of the ANOVA testing the p-value of $8.89*10^{-22}$ is less than that of 0.05 for the 95% confidence level chosen. This indicates that there is significant difference between

the sample groups tested [50]. From Figure 5.36, many of the samples do not overlap indicating differences between the groups. The summarized results of the Tukey test for the 90º sample groups that showed significant differences are shown in Table 5.43, with the full Tukey results in APPENDIX B, Table B.28.

Table 5.43: Tukey HSD results for flexural strength in 90º print orientation.

Treatments Pair	Tukey HSD Q Statistic	Tukey HSD p-value	Tukey HSD Inference
M100-90 vs LP100-90	37.6398	0.0010053	p<0.01
M100-90 vs CF100-90	13.8998	0.0010053	p<0.01
M100-90 vs LP50-90	38.3222	0.0010053	p<0.01
M100-90 vs CF50-90	35.43	0.0010053	p<0.01
LP100-90 vs CF100-90	23.74	0.0010053	p<0.01
LP100-90 vs M50-90	39.7961	0.0010053	p<0.01
CF100-90 vs M50-90	16.056	0.0010053	p<0.01
CF100-90 vs LP50-90	24.4225	0.0010053	p<0.01
CF100-90 vs CF50-90	21.5302	0.0010053	p<0.01
M50-90 vs LP50-90	40.4785	0.0010053	p<0.01
M50-90 vs CF50-90	37.5862	0.0010053	p<0.01

For the samples printed in the 90º orientation, there is a large amount of difference between the groups, impart due to the cracks that were present in the LP100-90, LP50-90, and the CF50-0 decreasing the flexural strength results. The CF100-90 and CF50-90 again showed weaker flexural strength then the neat Moai resin samples.

The results for the ANOVA analysis when comparing samples printed at a 100 μm layer height are summarized in Table 5.44, with the full ANOVA results in Table B.29 in APPENDIX B.

Table 5.44: ANOVA summary for flexural strength printed at 100 µm layer height.

Source of Variation	Sum of Squares	Degrees of Freedom	Mean Square	F-Statistic	P-value	F-Critical
Between Groups	28450	5	5690	132	$1.19*10^{-16}$	2.62
Within Groups	1030	24	43.1	-	-	-

The ANOVA result were also plotted in MatLab as box plots for visual examination of the data, and is shown in Figure 5.37.

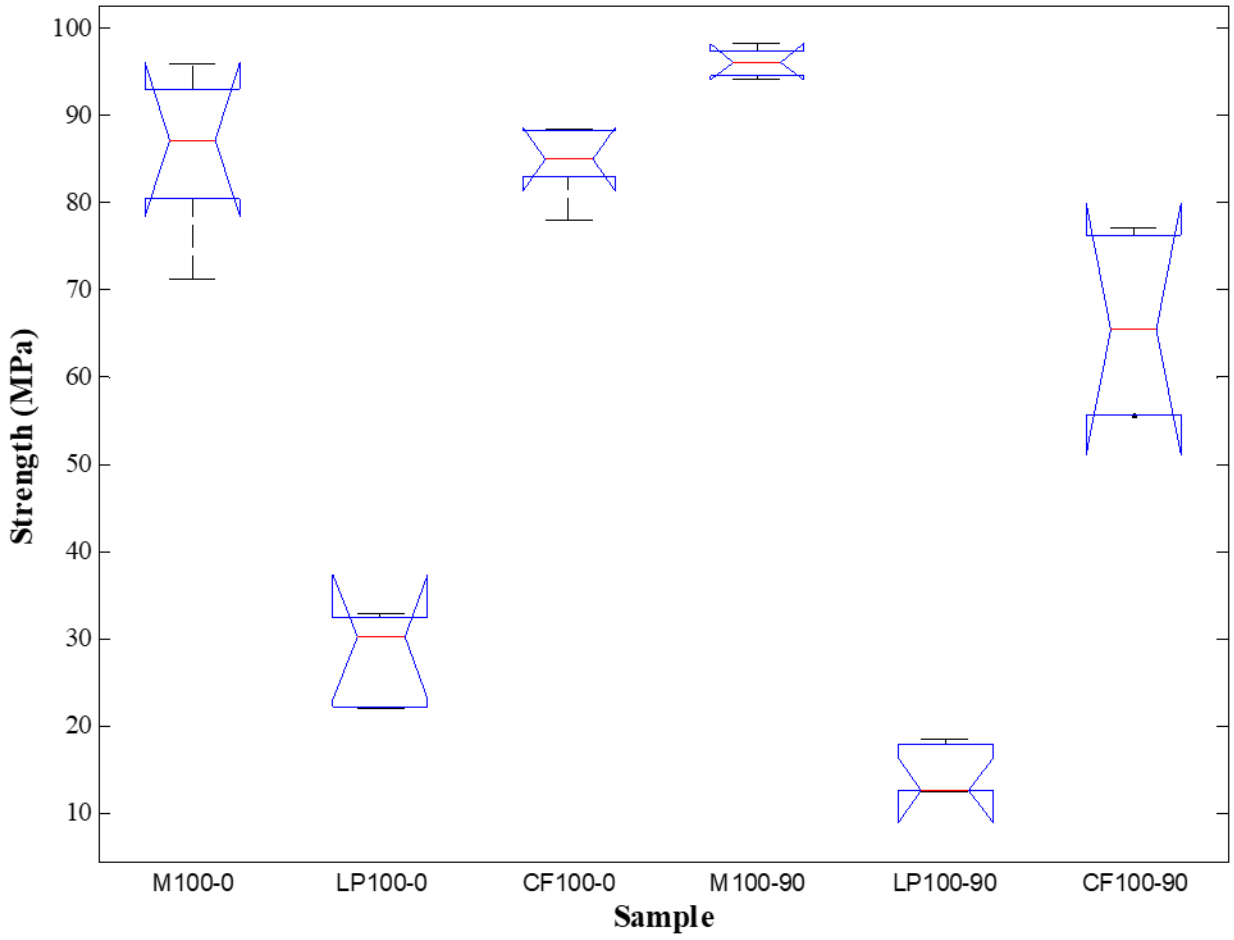

Figure 5.37: Box plot of ANOVA results for flexural strength printed at 100 µm layer height.

From the results of the ANOVA testing the p-value of $1.19*10^{-16}$ is less than that of 0.05 for the 95% confidence level chosen. This indicates that there is significant differences between the sample groups tested [50]. From Figure 5.37, a visual determination can be made to determine which groups differ, and from these box plots it can be seen that there is some separation between a few of the samples. The summarized results of the Tukey test for the 100 μm layer height sample groups that showed significant differences are shown in Table 5.45, with the full Tukey results in APPENDIX B, Table B.30.

Table 5.45: Tukey HSD results for flexural strength printed at 100 μm layer height.

Compared Pairs	Tukey HSD Q statistic	Tukey HSD p-value	Tukey HSD inference
M100-0 vs LP100-0	19.7968	0.0010053	p<0.01
M100-0 vs LP100-90	24.3289	0.0010053	p<0.01
M100-0 vs CF100-90	6.8084	0.0010053	p<0.01
LP100-0 vs CF100-0	19.437	0.0010053	p<0.01
LP100-0 vs M100-90	23.2466	0.0010053	p<0.01
LP100-0 vs LP100-90	4.5321	0.0391507	p<0.05
LP100-0 vs CF100-90	12.9884	0.0010053	p<0.01
CF100-0 vs LP100-90	23.9691	0.0010053	p<0.01
CF100-0 vs CF100-90	6.4485	0.0015818	p<0.01
M100-90 vs LP100-90	27.7788	0.0010053	p<0.01
M100-90 vs CF100-90	10.2582	0.0010053	p<0.01
LP100-90 vs CF100-90	17.5205	0.0010053	p<0.01

While the lower strength of the LP samples is causing a lot of the difference seen in the analysis, the CF100-0 was found to not be statistically different from the M100-0 sample, but again the lower result of the CF100-90 is seen. When comparing the M100-0 and M100-90 results the higher strength seen in the M100-90 is due to the surface defects not being present in the tested area of the specimen. This is the same as was seen with the tensile specimens in section 5.2.4.1.

The results for the ANOVA analysis when comparing samples printed at a 50 μm layer height are summarized in Table 5.46, with the full ANOVA results in Table B.31 in APPENDIX B.

Table 5.46: ANOVA summary for flexural strength at 50 μm layer height.

Source of Variation	Sum of Squares	Degrees of Freedom	Mean Square	F-Statistic	P-value	F-Critical
Between Groups	32950	5	6590	211	$5.18*10^{-19}$	2.62
Within Groups	750	24	31.2	-	-	-

The ANOVA result were also plotted in MatLab as notched box plots for visual examination of the data, and is shown in Figure 5.38.

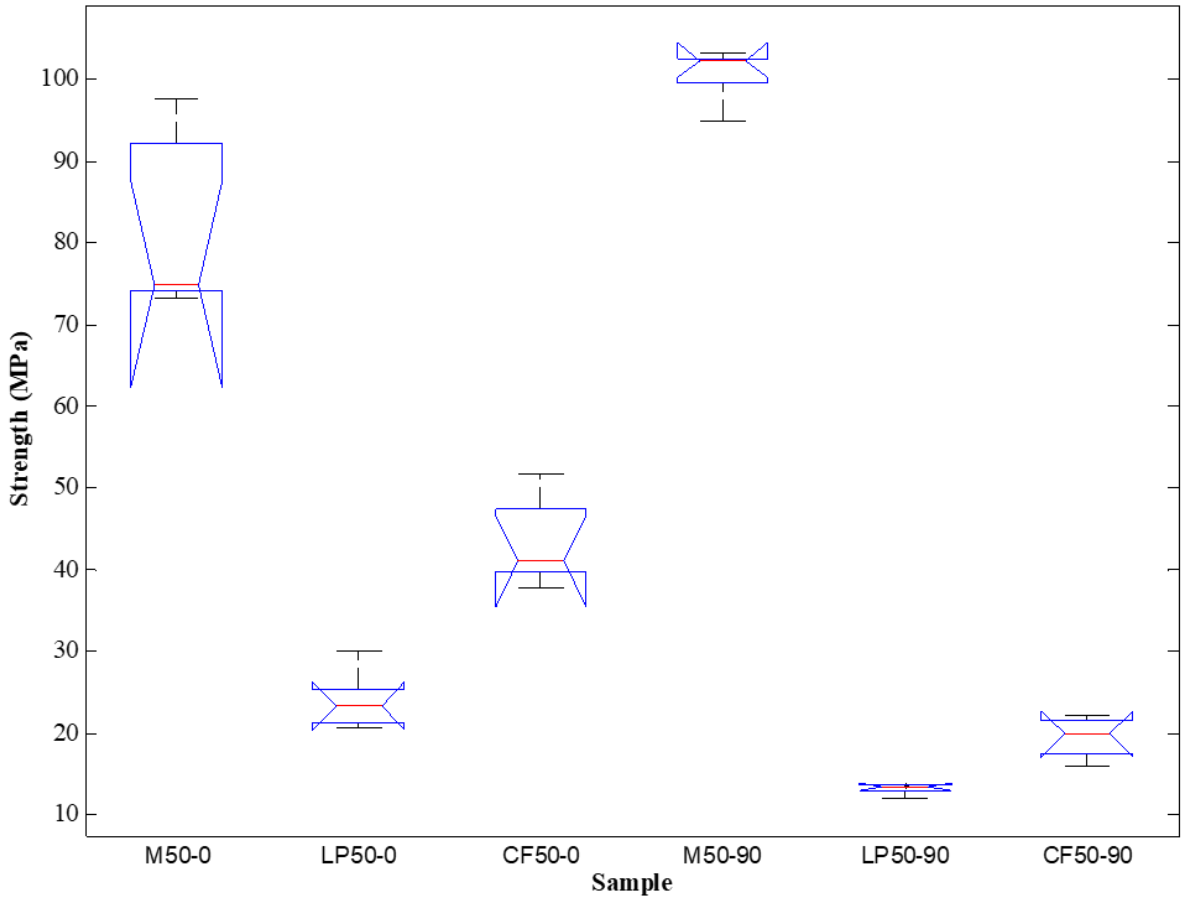

Figure 5.38: Box plot of ANOVA results for flexural strength printed at 50 µm layer height.

From the results of the ANOVA testing the p-value of $5.18*10^{-19}$ is less than that of 0.05 for the 95% confidence level chosen. This indicates that there is significant differences between the sample groups compared [50]. From Figure 5.38, there is separation between most of the samples. The summarized results of the Tukey test for the 50 µm layer height sample groups that showed significant differences are shown in Table 5.47, with the full Tukey results in APPENDIX B, Table B.32.

Table 5.47: Tukey HSD results for flexural strength printed at 50 μm layer height.

Treatments Pair	Tukey HSD Q Statistic	Tukey HSD p-value	Tukey HSD Inference
M50-0 vs LP50-0	23.3327	0.0010053	p<0.01
M50-0 vs CF50-0	15.532	0.0010053	p<0.01
M50-0 vs M50-90	7.4543	0.0010053	p<0.01
M50-0 vs LP50-90	27.6164	0.0010053	p<0.01
M50-0 vs CF50-90	25.1105	0.0010053	p<0.01
LP50-0 vs CF50-0	7.8008	0.0010053	p<0.01
LP50-0 vs M50-90	30.7871	0.0010053	p<0.01
CF50-0 vs M50-90	22.9863	0.0010053	p<0.01
CF50-0 vs LP50-90	12.0844	0.0010053	p<0.01
CF50-0 vs CF50-90	9.5786	0.0010053	p<0.01
M50-90 vs LP50-90	35.0707	0.0010053	p<0.01
M50-0 vs LP50-0	32.5649	0.0010053	p<0.01

Again the M50-90 sample had higher strength than the M50-0, due to the surface defects left behind on the M50-0 from the support material during printing. While the CF50-0 did have higher strength then the CF50-90, as would be expected if the fiber alignment was being influenced by the decreasing of the layer high, the cracks present from the printing process in the CF50-90 would be the main cause in the differences of the strengths. The LP samples again showed poor flexural strength due to the presence of surface cracks from the post-curing process.

5.2.4.3. Fracture Testing

A short-fiber composite resin consisting of the milled and sieved Toray T-700 carbon fiber at a fiber volume of 5%, Luperox P at 0.5 wt.%, and Moai resin was prepared as detailed in section 4.2.1. Fracture samples were manufactured and prepared as per sections 4.2.2, 4.2.3, and 4.3.5.1. The flexural testing was carried out as described in section 4.3.5.1, with the exception the test numbers 4,8,12, and 16 from Table 4.12 were left out. The test numbers omitted represent the samples made with carbon fiber and no thermal initiator which was shown as ineffective in section 5.1.1. The settings changed from default for the Moai printer are the same that were used in Table 5.5 unless otherwise stated. As in section 5.2.4.1, a thin layer of neat

Moai resin to the print bed before starting the print aided in keeping the part fixed to the bed during the printing process. With the same naming convention used for the samples as shown in Table 5.12.

From ASTM D5045 [54] the procedure to find the fracture toughness from the load-displacement curves involves verifying that plane-strain testing conditions were met. To verify this a conditional fracture toughness (K_Q) is first found using Equation 5.1,

$$K_Q = \left(\frac{P_{max}}{BW^{1/2}}\right) f(x), \tag{5.1}$$

where,

$$f(x) = 6x^{1/2}\frac{[1.99 - x(1-x)(2.15 - 3.93x + 2.7x^3)]}{(1+2x)(1-x)^{3/2}}, \text{ and } x = a/W, \tag{5.2}$$

where, B is thickness, W is width, and P_{max} is the peak load from the load-displacement curve. Once K_Q is found it has to be verified that the plastic zone is small enough for small scale yielding to be valid. This is checked by using the following inequality, Equation 5.3.

$$B,\ a,\ (W-a) > 2.5\left(K_Q/\sigma_y\right)^2 \text{ if true, } K_Q = K_{IC} \tag{5.3}$$

This inequality was found to be true for all specimens tested, and indicated that the specimen size could be reduced for future testing. This would aid in decreasing print times need to prepare the samples.

The fracture toughness was found as specified in ASTM D5045 section A1.4, and the results are shown for the samples printed in the 0º orientation in Figure 5.39, for the samples printed in the 90º orientation in Figure 5.40, and are summarized in Table 5.48 [54].

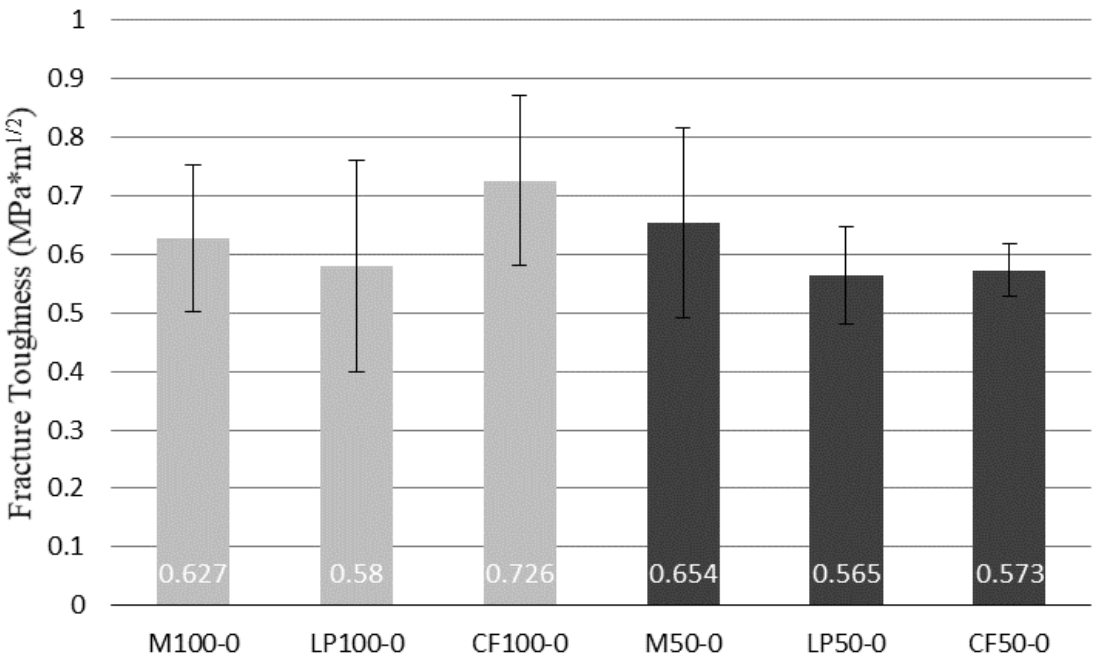

Figure 5.39: Fracture toughness for 0º print orientation.

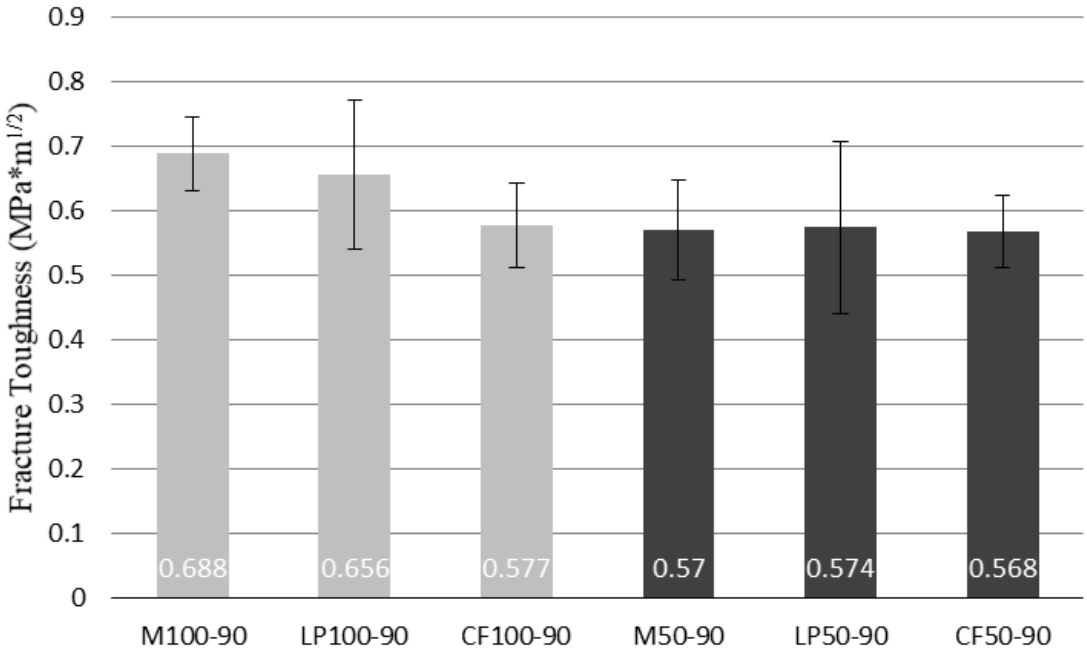

Figure 5.40: Fracture toughness for 90º print orientation.

Table 5.48: Summarized fracture testing results.

Sample	Layer Height (μm)	Print Orientation	Fiber Volume (%)	Fracture Toughness K_{IC} ($MPa\sqrt{m}$)
M100-0	100	0°	0	0.627 ± 0.126
M100-90	100	90º	0	0.688 ± 0.057
M50-0	50	0°	0	0.654 ± 0.162
M50-90	50	90º	0	0.570 ± 0.078
LP100-0	100	0°	0	0.580 ± 0.182
LP100-90	100	90º	0	0.656 ± 0.116
LP50-0	50	0°	0	0.565 ± 0.083
LP50-90	50	90º	0	0.574 ± 0.133
CF100-0	100	0°	5	0.726 ± 0.146
CF100-90	100	90º	5	0.577 ± 0.065
CF50-0	50	0°	5	0.573 ± 0.045
CF50-90	50	90º	5	0.568 ± 0.056

From the fracture testing carried out on the neat Moai resin, it can be observed that while the print orientation does not have an effect on the fracture toughness of the material, but the smaller 50 μm layer height does exhibit a decrease in 90º print orientation. From the specimens themselves, shown in Figure 5.41, it can be seen that the fracture is consistent with a mode I fracture regardless of the print orientation [44].

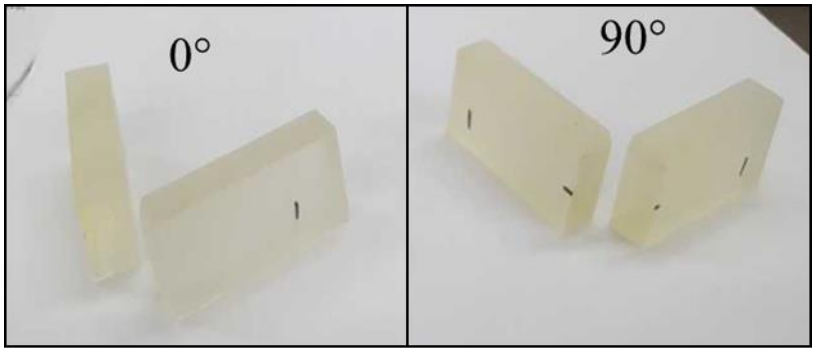

Figure 5.41: Fracture testing specimens.

The fracture toughness of the CF100-0 shows a 15.8% increase over the M00-0, but for all the other CF samples the results showed the same or lower fracture toughness. When

comparing the CF100-0 and CF100-90 the larger difference seen could be due to partial alignment of fibers parallel to the crack direction. While the LP samples showed the same surface cracking as seen previously in the tensile and flexural testing it does not appear to have had as large of an effect on the fracture toughness as it did on other material properties.

The incorporation of short-fibers can increase the fracture toughness by changing the failure modes associated with crack growth which can include fiber pull-out, bridging, failure, fiber/matrix debonding, and matrix cracking [44]. Ideally the change in the failure modes require more energy for crack initiation and propagation therefore increasing the fracture toughness, and would result in the composite having a higher fracture toughness then the matrix material [44]. From the tensile testing (section 5.2.4.1) it was shown that the composite had weak interfacial strength. The weak interfacial strength can cause the composite to have a weaker fracture toughness than the neat matrix, and the short-fiber lengths used in the CF samples can limit the energy need for fiber pull-out and crack bridging [44]. The incorporation of longer fiber lengths and/or increasing the fiber volume could help to increase the fracture toughness of the material in any future research [65].

Appling the statistical methods outlined in section 4.3.5.2 the results of the fracture toughness can be compared across the different layer heights and print orientations to help identify any trends within the data.

The results for the ANOVA analysis when comparing the fracture toughness of samples in the 0º print orientation are summarized in Table 5.49, with the full ANOVA results in Table B.33 in APPENDIX B.

Table 5.49: ANOVA summary for fracture toughness in the 0º print orientation.

Source of Variation	Sum of Squares	Degrees of Freedom	Mean Square	F-Statistic	P-value	F-Critical
Between Groups	0.0579	5	0.0116	0.6567	0.6627	3.1059
Within Groups	0.2116	12	0.0176	-	-	-

The ANOVA result were also plotted in MatLab as notched box plots for visual examination of the data, and is shown in Figure 5.42.

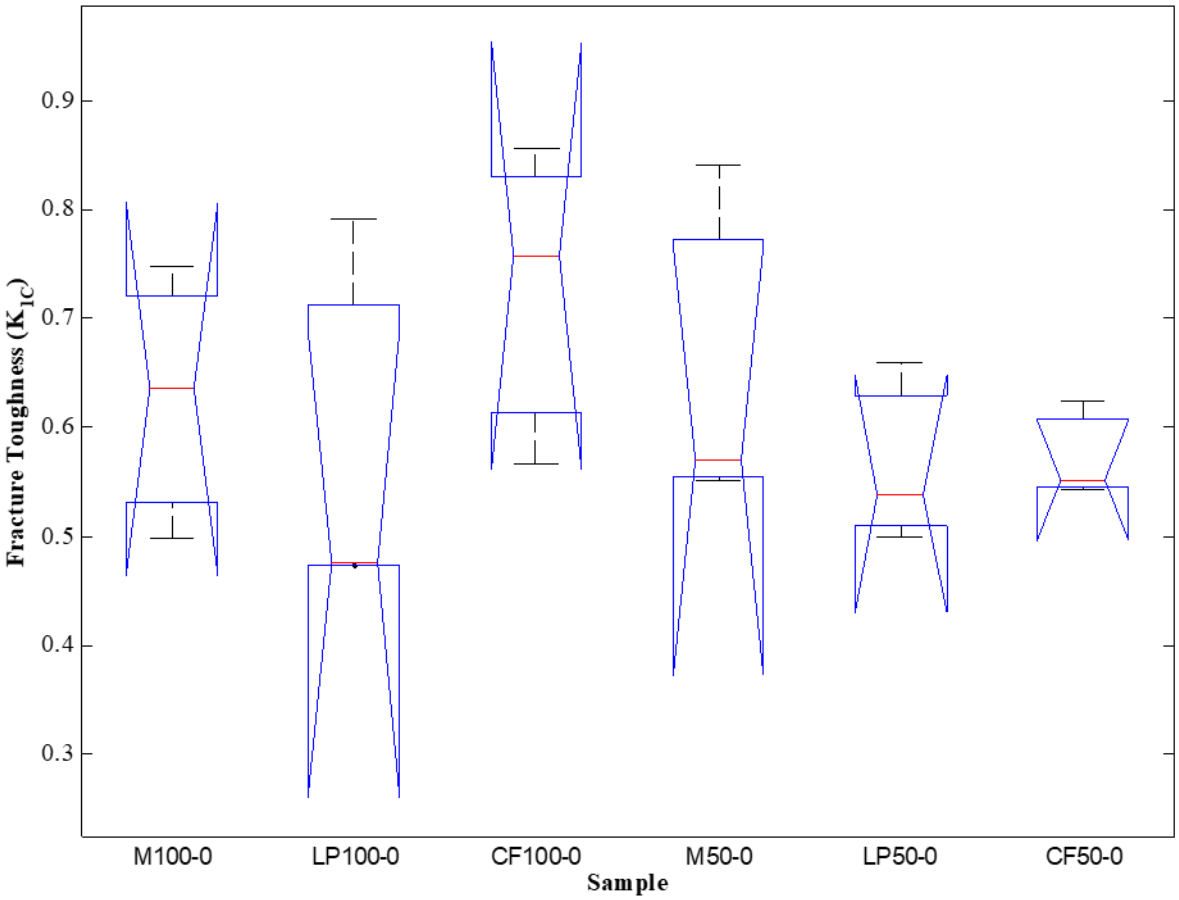

Figure 5.42: Box plot of ANOVA results for fracture toughness in the 0º print orientation.

From the results of the ANOVA testing the p-value of 0.663 is greater than that of 0.05 for the 95% confidence level chosen. This indicates that there is not a significant difference

between the sample groups tested [50]. From Figure 5.42, a visual determination can be made to confirm that the groups do not differ, and it can be seen that there is overlap between all of the samples within the 95% confidence level, represented by the ends of the notches. This is in part due to the large deviation with some of the tested samples. If this deviation could be corrected for more consistent samples then the CF100-0 could possibly be statistical different than the other samples tested. This is seen in the box plots median value (0.757 K_{1C}) for the CF100-0 being higher than its mean value (0.726 K1C) and that of the M100-0 sample. This could indicate that the potential for improvement in the fracture toughness is possible. For completeness, the Tukey HSD test was still carried out with none of the results indicating any significant differences. The results of the Tukey test for the 0º sample groups can be found in APPENDIX B, Table B.34.

The results for the ANOVA analysis when comparing the fracture toughness of samples in the 90º print orientation are summarized in Table 5.50, with the full ANOVA results in Table B.35 in APPENDIX B.

Table 5.50: ANOVA summary for fracture toughness in the 90º print orientation.

Source of Variation	Sum of Squares	Degrees of Freedom	Mean Square	F-Statistic	P-value	F-Critical
Between Groups	0.0418	5	0.0084	1.05	0.435	3.11
Within Groups	0.0957	12	0.0080	-	-	-

The ANOVA result were also plotted in MatLab as notched box plots for visual examination of the data, and is shown in Figure 5.43.

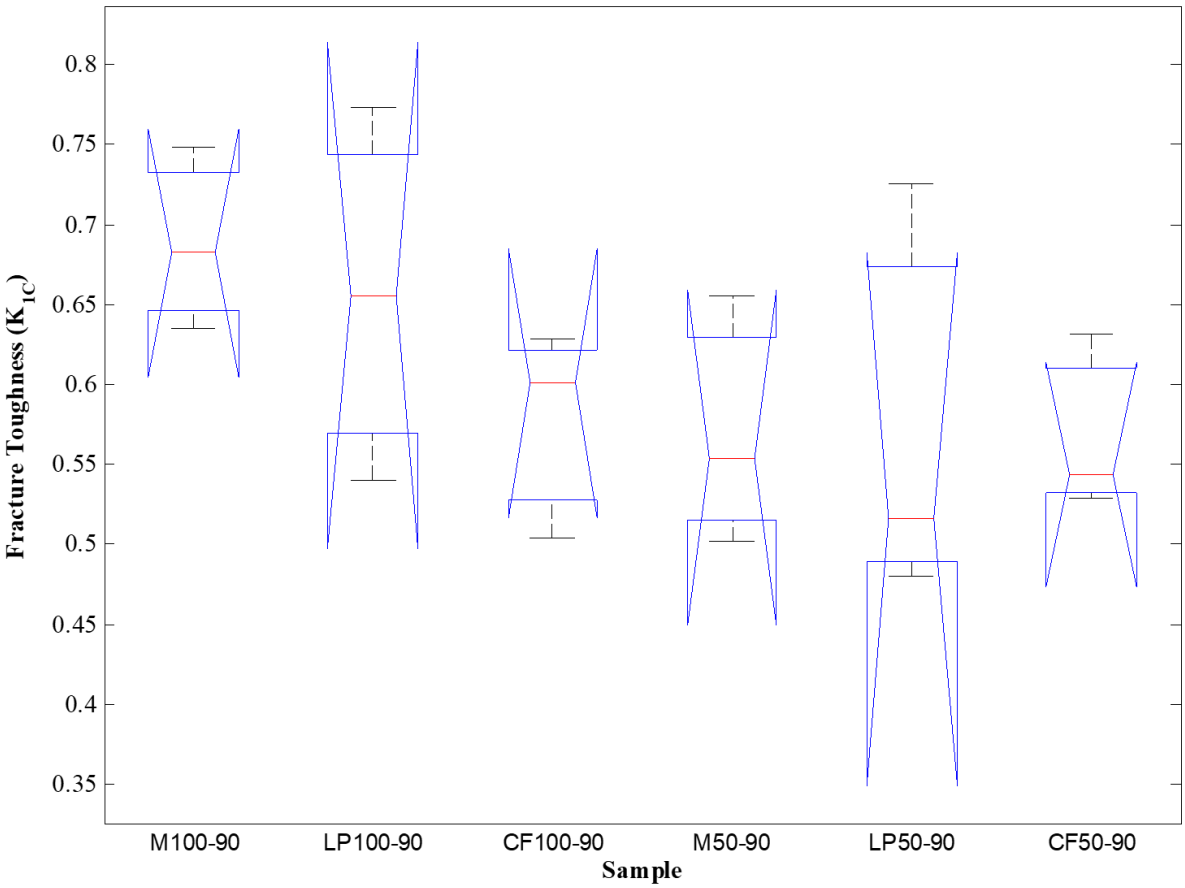

Figure 5.43: Box plot of ANOVA results for fracture toughness in the 90º print orientation.

From the results of the ANOVA testing the p-value of 0.435 is greater than that of 0.05 for the 95% confidence level chosen. This indicates that there is not a significant difference between the sample groups tested [50]. From Figure 5.43, a visual determination can be made to confirm that the groups do not differ, and it can be seen that there is overlap between all of the samples within the 95% confidence level, represented by the ends of the notches. This is again due to the large deviation with some of the tested samples. It can also be seen that the 100 µm layer height samples have a higher median value than the 50 µm layer height samples, but without smaller deviation of the samples conclusions that can be drawn are limited. For completeness, the Tukey HSD test was still carried out with none of the results indicating any

significant differences. The results of the Tukey test for the 90º sample groups can be found in APPENDIX B, Table B.36.

The results for the ANOVA analysis when comparing the fracture toughness of samples printed at a 100 μm layer height are summarized in Table 5.51, with the full ANOVA results in Table B.37 in APPENDIX B.

Table 5.51: ANOVA summary for fracture toughness of 100 μm layer height.

Source of Variation	Sum of Squares	Degrees of Freedom	Mean Square	F-Statistic	P-value	F-Critical
Between Groups	0.0533	5	0.0107	0.6972	0.6358	3.10588
Within Groups	0.1834	12	0.0153	-	-	-

The ANOVA result were also plotted in MatLab as notched box plots for visual examination of the data, and is shown in Figure 5.44.

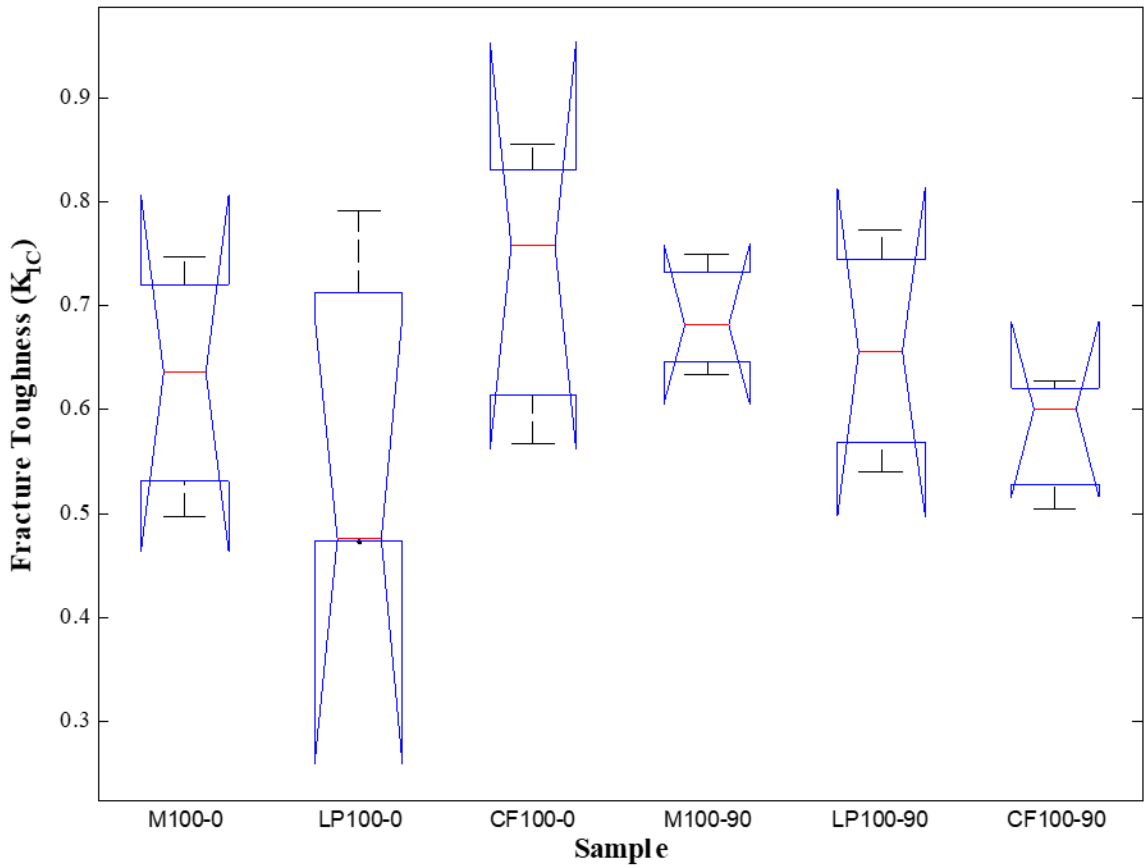

Figure 5.44: Box plot of ANOVA results for fracture toughness of 100 μm layer height.

From the results of the ANOVA testing the p-value of 0.636 is greater than that of 0.05 for the 95% confidence level chosen. This indicates that there is not a significant difference between the sample groups tested [50]. From Figure 5.44, a visual determination can be made to confirm that the groups do not differ, and it can be seen that there is overlap between all of the samples within the 95% confidence level, represented by the ends of the notches. These results demonstrate that the print orientation is not having an effect on the fracture toughness of the samples. For completeness, the Tukey HSD test was still carried out with none of the results indicating any significant differences. The results of the Tukey test for the 90º sample groups can be found in APPENDIX B, Table B.38.

The results for the ANOVA analysis when comparing the fracture toughness of samples printed at a 50 µm layer height are summarized in Table 5.52, with the full ANOVA results in Table B.39 in APPENDIX B.

Table 5.52: ANOVA summary for fracture toughness of 50 µm layer height.

Source of Variation	Sum of Squares	Degrees of Freedom	Mean Square	F-Statistic	P-value	F-Critical
Between Groups	0.0176	5	0.0035	0.3416	0.8780	3.10588
Within Groups	0.1240	12	0.0103	-	-	-

The ANOVA result were also plotted in MatLab as notched box plots for visual examination of the data, and is shown in Figure 5.45.

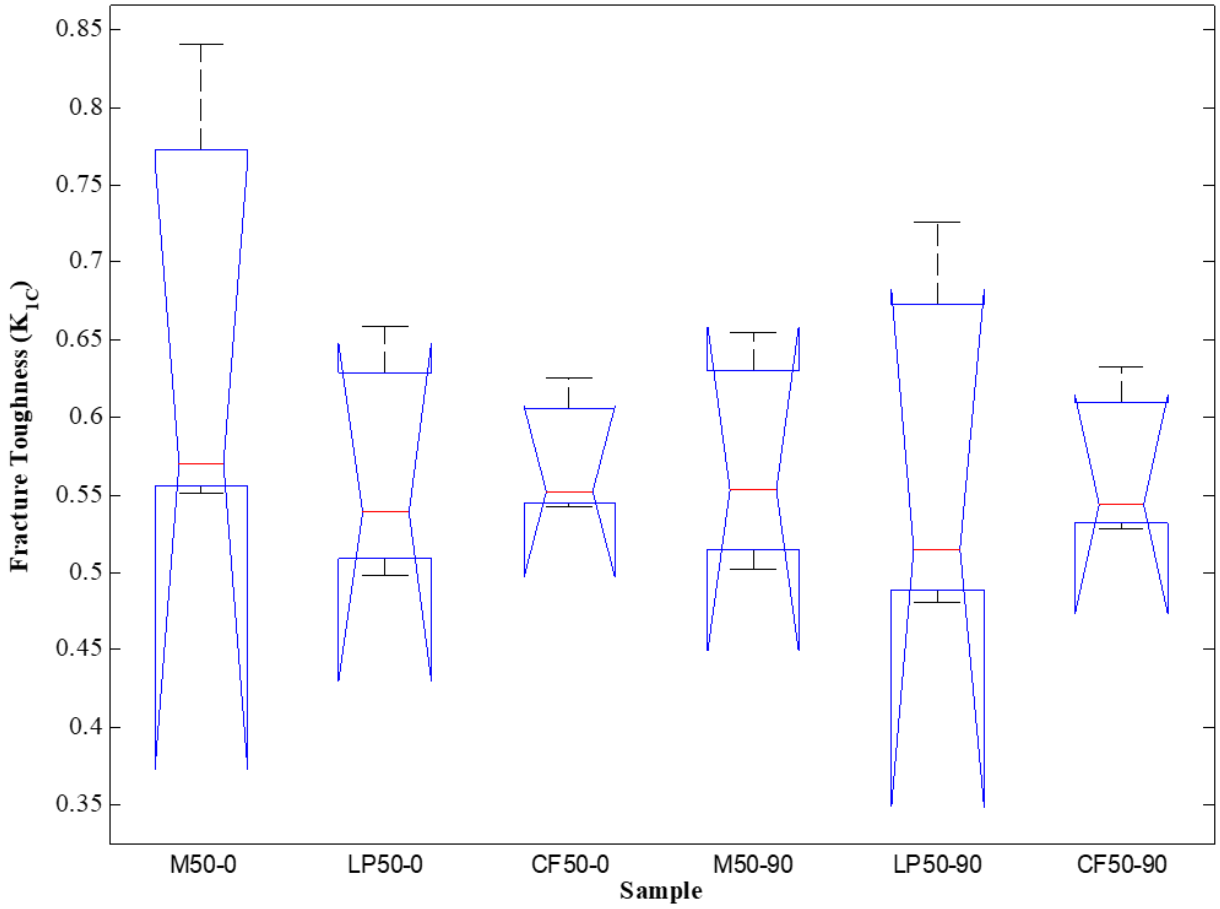

Figure 5.45: Box plot of ANOVA results for fracture toughness of 50 µm layer height.

From the results of the ANOVA testing the p-value of 0.878 is greater than that of 0.05 for the 95% confidence level chosen. This indicates that there is not a significant difference between the sample groups tested [50]. From Figure 5.45, a visual determination can be made to confirm that the groups do not differ, and it can be seen that the medians of the samples (red line) in the box plots are similar. For the 50 μm layer height samples the addition of carbon fiber and/or thermal initiator along with the print orientation had no influence on the fracture toughness. For completeness, the Tukey HSD test was still carried out with none of the results indicating any significant differences. The results of the Tukey test for the 90º sample groups can be found in APPENDIX B, Table B.40.

6. CONCLUSIONS AND RECOMMENDATIONS

6.1. Conclusions

The use of carbon fiber as a reinforcement in a short-fiber composite produced using stereolithography was experimentally investigated through this research. The use of a dual curing system consisting of a photo initiator for forming the part geometry, and a thermal initiator to completely cure the part was shown to be an effective method when using carbon fiber to manufacture composites using SLA printers.

To identify and evaluate the effectiveness of using a dual cure system for the manufacturing of carbon fiber composites, several thermal initiators were investigated through DSC, and the solubility and stability of the thermal initiators in the system was explored.

From the solubility testing it was found that several thermal initiators could be incorporated into the system. The ease of use from a processing stand point, were the thermal initiators that were liquid at room temperature. This aided in the dispersion and incorporation of the thermal initiator into the resin. The stability aspect that was evaluated proved to be an important area, due to some thermal initiators being evaluated that resulted in the system gelling within a short period of time. This could lead to polymerization during the printing process causing part failure, and potential damage to the print apparatus. While the Luperox P was stable during the printing process, it was observed that resin left out for a week at ambient temperatures would began to gel. This would only happen to the carbon fiber that had settled to the bottom of the container, while the remaining resin would still be unreacted. This could have been due to the thermal initiator undergoing induced decomposition from the increased concentration of carbon fiber [59]. Other possible thermal initiators to overcome this are discussed in the following Future Recommendations section.

From the DSC results it was determine that the neat Moai resin did not exhibit any curing due to thermal processing, but with the incorporation of a thermal initiator the resin would cure both with and without prior UV curing. Luperox P was chosen as the thermal initiator that yield the best results from the ones evaluated, both from a processing and material properties perspective.

To determine the effects of the printing process on the manufacturing of short-fiber composite the void content of the composite, fiber volume consistency, and resin viscosity were evaluated.

The void content of the samples produce showed to differ with the layer height of the sample printed. For a layer height of 100 μm a void content of 1.3% was found, while a layer height of 50 μm had a void content of 0.7%. The differences seen in the void content could have originated for two different sources. From when part is being printed, the layer that is currently being cured during the print has a reduction in the volume when going from the liquid state to the solid state, and creating free space. The smaller layer height would have less of a reduction due to less material changing phase, and therefore less free space. This would allow for the resin to recoat the vat easier, and therefore reducing the chance that voids could become trapped in the resin. The larger layer height would have more unreacted resin after the photo polymerization process, and while going through the thermal post curing process produce more gas byproducts from the reaction of the thermal initiator and resin, resulting in an increase in the void content [61].

The addition of the carbon fiber to the Moai resin was shown to increase the viscosity of the resin by 57%, but with the addition of the liquid thermal initiator (Luperox P) into the system it was lowered to only a 26% increase. The resin also showed some shear thinning behavior that

could have an influence on the fiber orientation with the part, and the ability for the fiber to stay suspended within the resin. To overcome this increase in resin viscosity, printing parameters where changed that increased the distance that the vat tilted down during the peel step to allow for more time and to increase resin flow over the processing area. The fiber volume consistency was found to not vary with time, but be due to the fiber dispersed in the resin within the immediate area of the part becoming depleted. To improve the fiber volume consistency a method of mixing the resin during the printing processes should be used in future research.

To evaluated the effects of the carbon fiber on the material properties the composite was evaluated by tensile, flexural, and fracture testing. While comparing what effects layer height and print orientation have on the material properties of the produced short-fiber composite.

From the tensile testing results, the carbon fiber samples showed an increase in Young's modulus of 21% for a 100 μm layer height, and a 27% for a 50 μm layer height. The change in the modulus due to the lower layer high is due to the fibers being aligned in the loading direction with in the sample. This demonstrates that manipulating a part's properties based off of fiber length and layer height could be possible. This increase was less than what was predicted by theoretical models. The lower modulus was thought to be due to large distribution of fiber lengths and poor interfacial properties between the carbon fiber and matrix. These defects also lead to the carbon fiber samples having a lower tensile strength then the neat Moai resin samples. With improvements in these areas the tensile properties of the composite could be further improved.

The flexural strength, flexural modulus, and fracture toughness showed no noticeable gains in material properties from the use of the carbon fiber reinforcement. For the flexural testing this is thought to be due because of the low fiber volume (5%) and high fiber volume

inconsistency of the samples. The low fiber volume (5%) and short fiber lengths (76 μm) of the fracture samples resulted in no improvements in fracture toughness, but also did not cause any decrease in the fracture toughness.

While factors such as interfacial strength, fiber length distribution and volume consistency, and low fiber volume content lowered the effectiveness of the carbon fiber as a reinforcement the main limiting factor is the fiber length itself. The average fiber length used was 76 μm. This is much shorter than the critical fiber length that was found to be 433 μm for the system. While it would be possible to incorporate fibers of this length into the resin and print parts, they could not have isotropic properties due to forced alignment of the layer height. The effects of fibers folding over within the layers could also affect the ability for the part to print successfully. This could be by limiting the amount of matrix material available to keep the layers attached to one and another. To avoid this it would require a layer height at least as larger as the fiber length itself. This is outside of the capabilities of even industrial grade SLA printers, that typical print at around 200 μm on the top end of layer height [5]. The incorporation of carbon fiber and the subsequent shadowing of the photo initiator from the UV source would even further limit the depth of cure that could be achieved. So while it might not be feasible to use fiber with a length of 433 μm, increasing the fiber length and tightening the fiber length distribution would aid in increasing the material properties for the samples studied in this research.

The research does show that the use of a dual cure resin system could be used for the additive manufacturing of carbon fiber composites, and can provide a good starting point for the continuation of this area of research.

6.2. Future Recommendations

To aid in the continuation of the research carried out in this study, the following section provides recommendations in both the areas of processing and material improvements. Looking specifically and the type of thermal initiators, fibers, and apparatus used.

For this research all of the thermal initiators looked at for their possible use in the dual cure system were organic peroxides There is another class of thermal initiators that are commonly used for free radical polymerization, known as aliphatic azo compounds (azo). The azo initiators are not as effected by fillers, and do not undergo radical induced decomposition [66]. This could prove useful for the long-term stability of the resins used for manufacturing short-fiber composites via SLA.

The carbon fiber used in this research was sized for an epoxy matrix. With the use of a carbon fiber sized for use with a urethane or vinyl ester matrix, the interfacial properties might be increased, and therefore the material properties of the composite. The other method of approach would be to use a different resin for the matrix material. There are SLA resins that are commercially available that are labeled as epoxy resins. While these are not true epoxies, they do contain bisphenol A in the polymer chain, and could prove to bond better to the carbon fiber sized for an epoxy matrix. If these types of resin are to be used with the SLA printer used in this research, a different vat bed/coating would have to be used. The epoxy SLA resins react with the silicon layer used in the vats, causing the parts to stick and subsequently fail.

During the process of conducting the research for this study, there was one factor within the printing process that seemed to limit the composites that could be produced, and this was the use of a bottom-up SLA style printer. This is mainly due to the peel step that is used to separate the layer from the vat. It was seen in the cracks that were produced when printing at the 50 μm

layer height causing failure, and why any attempts to print parts at higher fiber volumes (7.5% and 10%) resulted in print failure. By switching to a top-down style printer this peel step would be removed, and there would be an added benefit from not have to use as much support material. This is because it would only be need to keep the part in place, not support it from the forces generated in the peel step.

The use of a top-down style printer could also allow for the easy incorporation of a pump/mixing unit to help maintain fiber volume consistency. While this was tried for the Moai printer the main limitation was the lack of space for equipment of the necessary size to be incorporated, due to the limited free space available in the vat with the print bed present. Because of the large vat size need for the top-down style printer adding a pump to the tank, along with an angled bottom, should allow for mixing of the resin to maintain a constant fiber distribution during the printing process. One issue that would need to be addressed would be for the printing of parts that have random fiber orientation, and therefore isotropic properties. During the printing process for top-down style machines, a recoat blade moves across the top of the tank to smooth out the resin for the printing of the next layer. This has been shown by Cheah C. et al. to produce near unidirectional composites and could limit the applications of the parts produced [32]. This might be overcome by not including the recoat blade, but adjusting the raising and lowering settings for the build platform. This would allow for some settling to occur, but would increase the print time of the parts.

REFERENCES

[1] Hull, C. W., 1986, "Apparatus for production of three-dimensional objects by stereolithography," U.S. Patent 4575330A.

[2] Wang, X., Jiang, M., Zhou, Z., Gou, J., and Hui, D. "3D printing of polymer matrix composites: A review and prospective." *Composites Part B: Engineering* Vol. 110 (2017): pp. 442-458.

[3] Karalekas, D., and Antoniou, K. "Composite rapid prototyping: overcoming the drawback of poor mechanical properties." *Journal of Materials Processing Technology* Vol. 153-154 (2004): pp. 526-530.

[4] Parandoush, P., and Lin, D. "A review on additive manufacturing of polymer-fiber composites." *Composite Structures* Vol. 182 (2017): pp. 36-53.

[5] Jacobs, P. F., *Rapid Prototyping & Manufacturing: Fundamentals of Stereolithography*, Society of Manufacturing Engineers, (1992)

[6] Tumbleston, J. R., Shirvanyants, D., Ermoshkin, N., Janusziewicz, R., Johnson, A. R., Kelly, D., Chen, K., Pinschmidt, R., Rolland, J. P., and Ermoshkin, A. "Continuous liquid interface production of 3D objects." *Science* (2015): DOI 10.1126/science.aaa2397

[7] "DruckWege Resin Technical Datasheet," https://druckwege.de/wp-content/uploads/2018/07/Technical-Datasheet_TypD_English_v6.pdf. Accessed 2018

[8] "FLGPCL03 Clear Resin Technical Datasheet," https://formlabs.com/media/upload/Clear-DataSheet.pdf. Accessed 2018

[9] "Moai Clear Resin Technical Datasheet." ." http://wiki.peopoly.net/doku.php?id=moai-resin. Accessed 2018

[10] Zguris, Z. "How mechanical properties of stereolithography 3D prints are affected by UV curing." Formlabs, Inc., Somerville, MA, 2017.

[11] Stansbury, J. W., and Idacavage, M. J. "3D printing with polymers: Challenges among expanding options and opportunities." *Dental Materials* Vol. 32 No. 1 (2016): pp. 54-64.

[12] Ogale, A. A., and Renault, T. "3-D Photolithography for Composite Development: Discontinuous Reinforcements," *SAMPE Quarterly* Vol. 5, No. 6 (1991): pp. 28-38

[13] Agarwal, B. D., Broutman, L. J., and Chandrashekhara, K. *Analysis and Performance of Fiber Composites*, John Wiley & Sons, New York (2017).

[14] Taya, M., and Arsenault, R. J. "A comparison between a shear lag type model and an eshelby type model in predicting the mechanical properties of a short fiber composite," *Scripta Metallurgica* Vol. 21 No. 3 (1987): pp. 349-354.

[15] Mortazavian, S., and Fatemi, A. "Effects of fiber orientation and anisotropy on tensile strength and elastic modulus of short fiber reinforced polymer composites," *Composites Part B: Engineering*, Vol. 72 (2015): pp. 116-129.

[16] Papthanasiou, T. D., and Guell, D. C. *Flow-induced alignment in composite materials*, Elsevier (1997)

[17] Zainudin, E. S., Sapuan, S. M., Sulaiman, S., and Ahmad, M. "Fiber orientation of short fiber reinforced injection molded thermoplastic composites: A review," *Journal of Injection Molding Technology*, Vol. 6 No. 1 (2002): pp. 1.

[18] Tucker Iii, C. L., and Liang, E. "Stiffness predictions for unidirectional short-fiber composites: Review and evaluation," *Composites Science and Technology*, Vol. 59 No. 5 (199): pp. 655-671.

[19] Altan, M. C. "A Review of Fiber-Reinforced Injection Molding: Flow Kinematics and Particle Orientation," *Journal of Thermoplastic Composite Materials*, Vol. 3 No. 4 (1990): pp. 275-313.

[20] Vincent, M., Giroud, T., Clarke, A., and Eberhardt, C. "Description and modeling of fiber orientation in injection molding of fiber reinforced thermoplastics," *Polymer*, Vol. 46 No. 17 (2005): pp. 6719-6725.

[21] Chung, D. H., and Kwon, T. H. "Fiber orientation in the processing of polymer composites," *Korea-Australia Rheology Journal*, Vol. 14 No. 4 (2002): pp. 175-188.

[22] Goh, G. D., Dikshit, V., Nagalingam, A. P., Goh, G. L., Agarwala, S., Sing, S. L., Wei, J., and Yeong, W. Y. "Characterization of mechanical properties and fracture mode of additively manufactured carbon fiber and glass fiber reinforced thermoplastics." *Materials & Design* Vol. 137 (2018): pp. 79-89.

[23] Ferreira, R. T. L., Amatte, I. C., Dutra, T. A., and Bürger, D. "Experimental characterization and micrography of 3D printed PLA and PLA reinforced with short carbon fibers." *Composites Part B: Engineering*, Vol. 124 (2017): pp. 88-100.

[24] Ning, F., Cong, W., Qiu, J., Wei, J., and Wang, S. "Additive manufacturing of carbon fiber reinforced thermoplastic composites using fused deposition modeling." *Composites Part B: Engineering* Vol. 80 (2015): pp. 369-378.

[25] Hector Sandoval, J., and Wicker, R. B. "Functionalizing stereolithography resins: effects of dispersed multi-walled carbon nanotubes on physical properties." *Rapid Prototyping Journal* Vol. 12 No. 5 (2006): pp. 292-303.

[26] Yang, Z., Wu, G., Wang, S., Xu, M., and Feng, X. "Dynamic postpolymerization of 3D-printed photopolymer nanocomposites: Effect of cellulose nanocrystal and postcure temperature." *Journal of Polymer Science Part B: Polymer Physics* Vol. 56 No. 12 (2018): pp. 935-946.

[27] Feng, X., Yang, Z., Chmely, S., Wang, Q., Wang, S., and Xie, Y. "Lignin-coated cellulose nanocrystal filled methacrylate composites prepared via 3D stereolithography printing: Mechanical reinforcement and thermal stabilization." *Carbohydrate Polymers* Vol. 169 (2017): pp. 272-281.

[28] Tekinalp, H. L., Kunc, V., Velez-Garcia, G. M., Duty, C. E., Love, L. J., Naskar, A. K., Blue, C. A., and Ozcan, S. "Highly oriented carbon fiber–polymer composites via additive manufacturing." *Composites Science and Technology* Vol. 105 (2014): pp. 144-150.

[29] Thomas, H., David, B. P., Guido, T., and Hans, N. H. "State-of-the-art of fiber-reinforced polymers in additive manufacturing technologies." *Journal of Reinforced Plastics and Composites* Vol. 36 No. 15 (2017): pp. 1061-1073.

[30] Gupta, A., and Ogale, A. A. "Dual curing of carbon fiber reinforced photoresins for rapid prototyping." *Polymer Composites* Vol. 23 No. 6 (2002): pp. 1162-1170.

[31] Taormina, G., Sciancalepore, C., Bondioli, F., and Messori, M. "Special resins for stereolithography: In situ generation of silver nanoparticles." *Polymers* Vol. 10 No.2:(2018) pp. 212.

[32] Cheah, C. M., Nee, A. Y. C., Fuh, J. Y. H., and Lu, L., "Mechanical characteristics of fiber-filled photo-polymer used in stereolithography." *Rapid Prototyping Journal* Vol. 5 No. 3 (199): pp. 112-119.

[33] Grasso, M., Martorelli, M., Lanzotti, A., and Staiano, G. "The impact of process parameters on mechanical properties of parts fabricated in PLA with an open-source 3-D printer," *Rapid Prototyping Journal*, Vol. 21 No. 5 (2015): pp. 604-617.

[34] L. Dunn, M., Suwito, W., and Cunningham, S. "Fracture Initiation at Sharp Notches: Correlation Using Critical Stress Intensities." *International Journal of Solids and Structures* Vol. 34 No. 29 (1997): pp 3873-3883

[35] Lerch, B. A., Thesken, J. C., and Bunnell, C. T. "Polymethylmethacrylate (PMMA) material test results for the capillary flow experiments (CFE)."Technical Report No. NASA/TM-2007-214835 NASA STI Program, Cleveland, OH. 2007

[36] Huang Donald, D. "The application of fracture mechanics to short fiber composites." *Polymer Composites* Vol. 16 No. 1 (2004): pp. 10-16.

[37] Mower, T. M., and Li, V. C. "Fracture characterization of random short fiber reinforced thermoset resin composites," *Engineering Fracture Mechanics*, Vol. 26 No. 4 (1987): pp. 593-603.

[38] Fitzer, E. "Pan-based carbon fibers—present state and trend of the technology from the viewpoint of possibilities and limits to influence and to control the fiber properties by the process parameters," *Carbon*, Vol. 27 No. 5 (1989) pp. 621-645.

[39] Yao, S.-S., Jin, F.-L., Rhee, K. Y., Hui, D., and Park, S.-J. "Recent advances in carbon-fiber-reinforced thermoplastic composites: A review." *Composites Part B: Engineering* Vol. 142 (2018): pp. 241-250.

[40] Maradur, S. P., Kim, C. H., Kim, S. Y., Kim, B.-H., Kim, W. C., and Yang, K. S. "Preparation of carbon fibers from a lignin copolymer with polyacrylonitrile." *Synthetic Metals* Vol. 162 No.5 (2012): pp. 453-459.

[41] Chand, S. "Review Carbon fibers for composites." *Journal of Materials Science* Vol. 35 No. 6(2000) pp. 1303-1313.

[42] "Toray T-700S Technical Datasheet." https://www.toraycma.com/file_viewer.php?id=4459 Accessed 2018

[43] "Carbiso MF SM45R-100 Technical Datasheet." http://www.elgcf.com/assets/datasheets/Carbiso-MF-TDS.pdf Accessed 2018

[44] Anderson, T. L. *Fracture Mechanics: Fundamentals and Applications*, CRC press, Boca Rarton, FL, (2005)

[45] ASTM E2160-04 Standard Test Method for Heat of Reaction of Thermally Reactive Materials by Differential Scanning Calorimetry, ASTM International, West Conshohocken, PA, 2018

[46] Instruments, TA, *AR-G2/AR 2000ex Operator's Manual*, New Castle, DE. (2010)

[47] Shenoy, A. V. *Rheology of filled polymer systems*, Springer Science & Business Media. (2013)

[48] ASTM D638-14 Standard Test Method for Tensile Properties of Plastics, ASTM International, West Conshohocken, PA, 2014

[49] ASTM D3039/D3039M-17 Standard Test Method for Tensile Properties of Polymer Matrix Composite Materials, ASTM International, West Conshohocken, PA, 2017

[50] Levine, D. M., Ramsey, P. P., and Smidt, R. K. *Applied statistics for engineers and scientists: using Microsoft Excel and Minitab*, Prentice Hall, Upper Saddle River, (2001).

[51] Devore, J. L. *Probability and Statistics for Engineering and the Sciences*, Cengage learning. (2011)

[52] Tukey, J. W. "Comparing Individual Means in the Analysis of Variance," *Biometrics*, Vol. 5 No. 2 (1949): pp. 99-114.

[53] ASTM D790-17 Standard Test Methods for Flexural Properties of Unreinforced and Reinforced Plastics and Electrical Insulating Materials, ASTM International, West Conshohocken, PA, 2017

[54] ASTM D5045-14 Standard Test Methods for Plane-Strain Fracture Toughness and Strain Energy Release Rate of Plastic Materials, ASTM International, West Conshohocken, PA, 2014

[55] ASTM E399-17 Standard Test Method for Linear-Elastic Plane-Strain Fracture Toughness K_{Ic} of Metallic Materials, ASTM International, West Conshohocken, PA, 2017

[56] ASTM D3171-15 Standard Test Methods for Constituent Content of Composite Materials, ASTM International, West Conshohocken, PA, 2015

[57] ASTM D792-13 Standard Test Methods for Density and Specific Gravity (Relative Density) of Plastics by Displacement, ASTM International, West Conshohocken, PA, 2013

[58] Zhang, H., Zhang, Z., and Breidt, C. "Comparison of short carbon fibre surface treatments on epoxy composites: I. Enhancement of the mechanical properties," *Composites Science and Technology* Vol. 64 No. 13 (2004): pp. 2021-2029.

[59] Dixon, K. W. "Decomposition rates of organic free radical initiators," *Polymer handbook* Vol .4 (1999).

[60] Purslow, D. "Matrix fractography of fibre-reinforced epoxy composites," *Composites*, Vol. 17 No. 4 (1986): pp. 289-303.

[61] Masere, J., Chekanov, Y., Warren, J. R., Stewart, F. D., Al-Kaysi, R., Rasmussen, J. K., and Pojman, J. A. "Gas-free initiators for high-temperature free-radical polymerization," *Journal of Polymer Science Part A: Polymer Chemistry,* Vol. 38 No. 21 (2000): pp. 3984-3990.

[62] Braga, R. R., Ballester, R. Y., and Ferracane, J. L. "Factors involved in the development of polymerization shrinkage stress in resin-composites: A systematic review," *Dental Materials*, Vol. 21 No. 10 (2005): pp. 962-970.

[63] Chambers, A. R., Earl, J. S., Squires, C. A., and Suhot, M. A. "The effect of voids on the flexural fatigue performance of unidirectional carbon fibre composites developed for wind turbine applications," *International Journal of Fatigue,* Vol. 28 No. 10 (2006): pp. 1389-1398.

[64] Parry, T. V., and Wronski, A. S. "Kinking and tensile, compressive and interlaminar shear failure in carbon-fibre-reinforced plastic beams tested in flexure," *Journal of Materials Science*, Vol. 16 No. 2 (1981): pp. 439-450.

[65] Cholake, S. T., Moran, G., Joe, B., Bai, Y., Singh Raman, R. K., Zhao, X. L., Rizkalla, S., and Bandyopadhyay, S. "Improved Mode I fracture resistance of CFRP composites by reinforcing epoxy matrix with recycled short milled carbon fibre," *Construction and Building Materials,* Vol. 111 (2016): pp. 399-407.

[66] Sheppard Chester, S., and Kamath Vasanth, R. "The selection and use of free radical initiators," *Polymer Engineering & Science*, Vol. 19 No. 9 (2004) pp. 597-606.

APPENDIX A. EXPERIMENTAL DATA

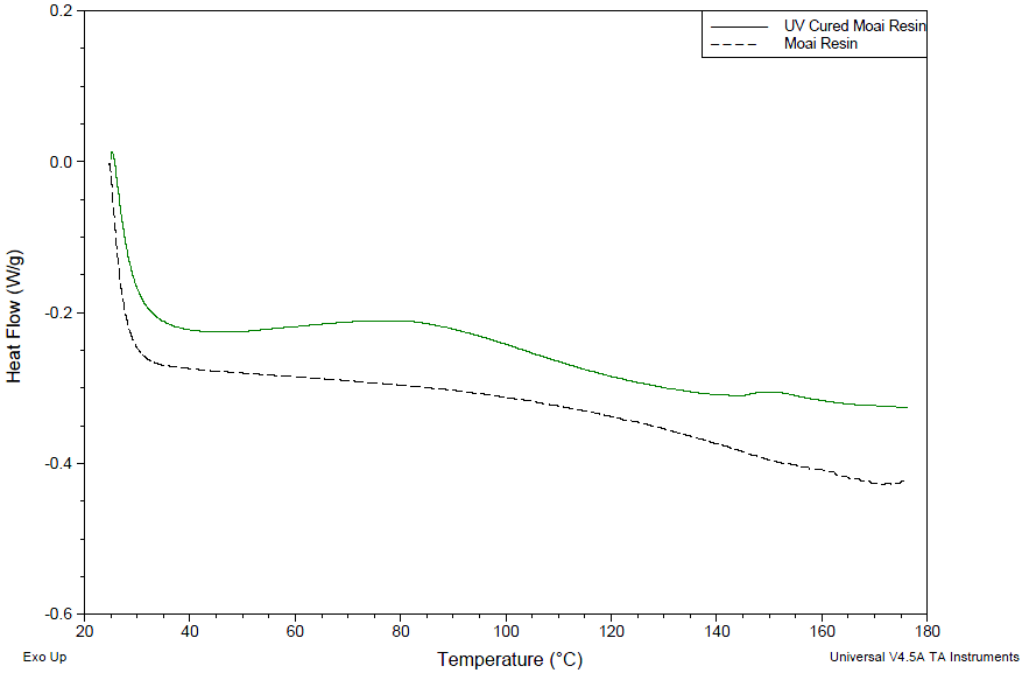

Figure A.1: DSC curves for Moai resin.

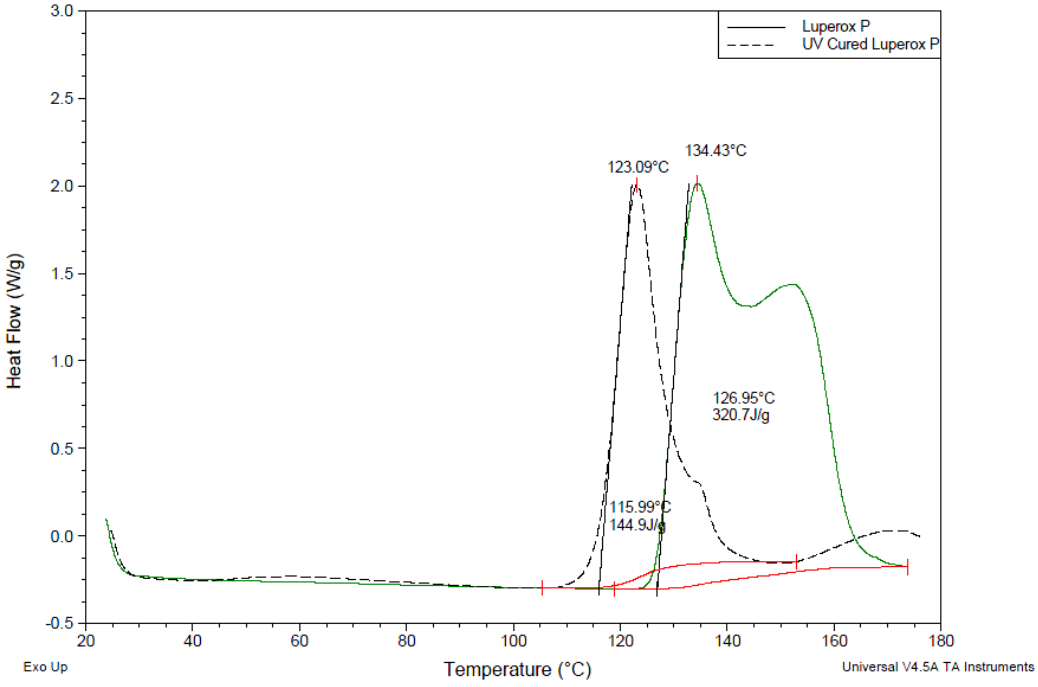

Figure A.2: DSC curves for Luperox P.

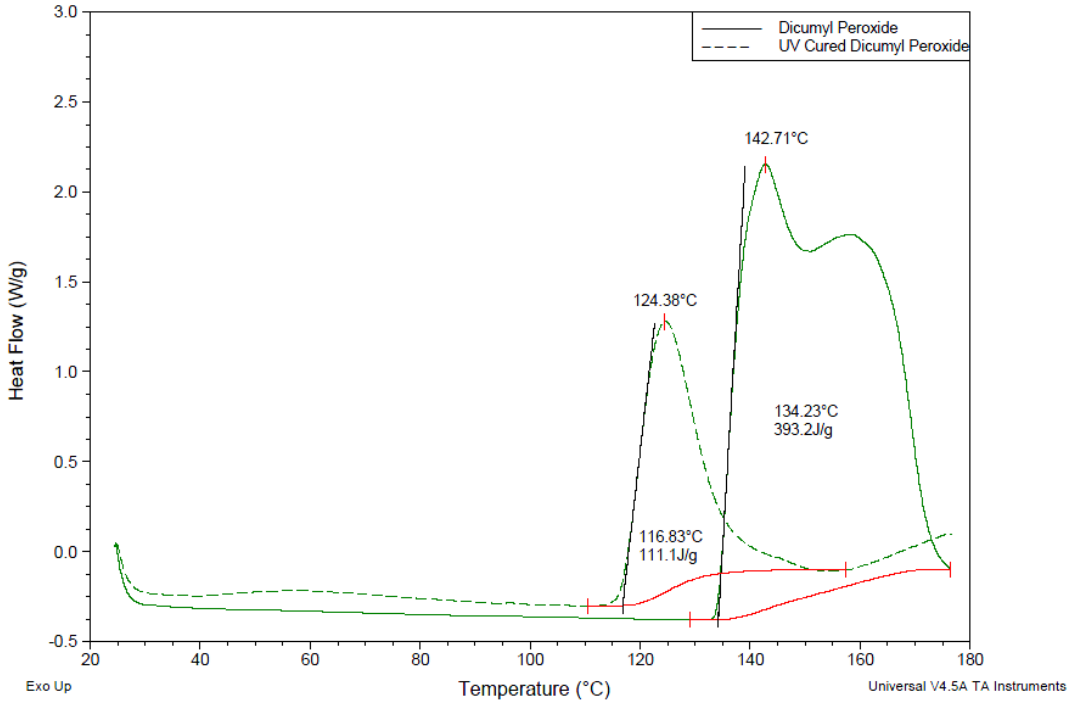

Figure A.3: DSC curves for dicumyl peroxide.

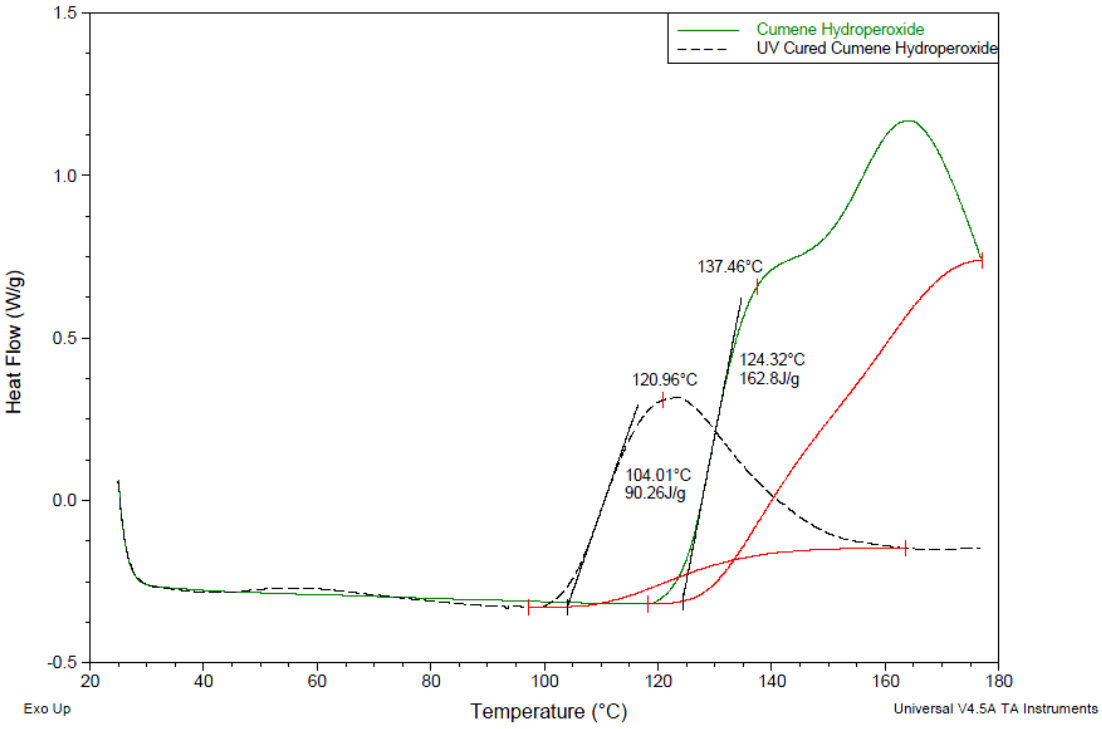

Figure A.4: DSC curves for cumene hydroperoxide.

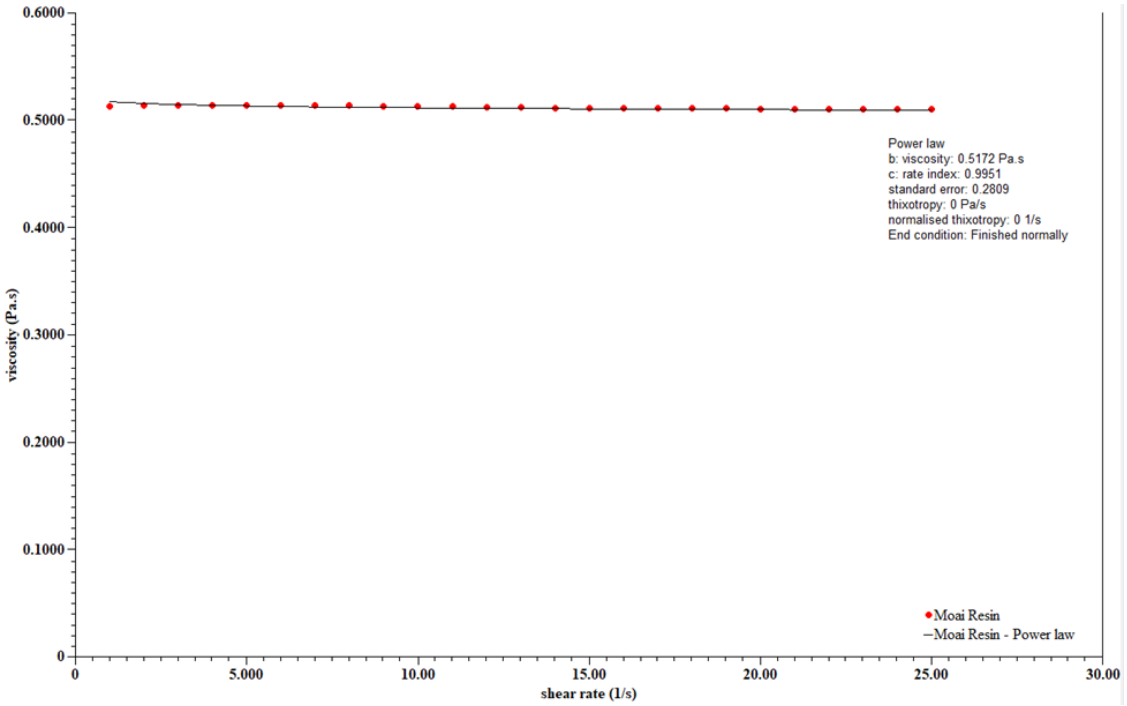

Figure A.5: Moai resin viscosity curve 1 s^{-1} to 25 s^{-1}.

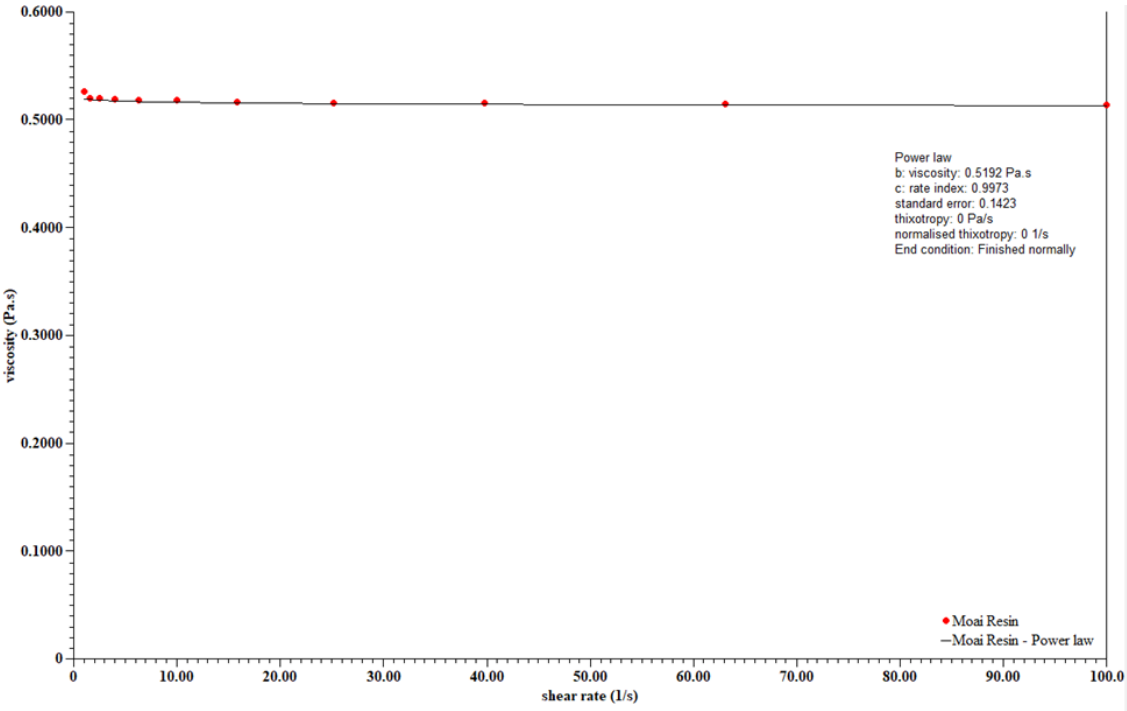

Figure A.6: Moai resin viscosity curve 1 s^{-1} to 100 s^{-1}.

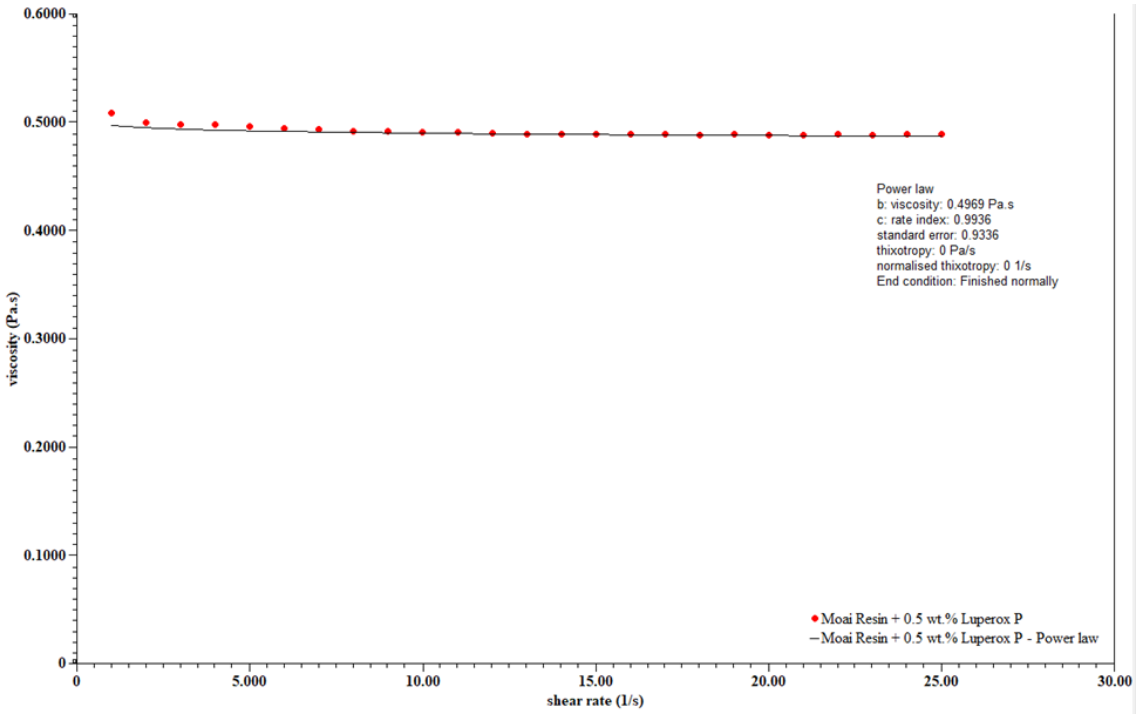

Figure A.7: Moai resin + Luperox P viscosity curve 1 s^{-1} to 25 s^{-1}.

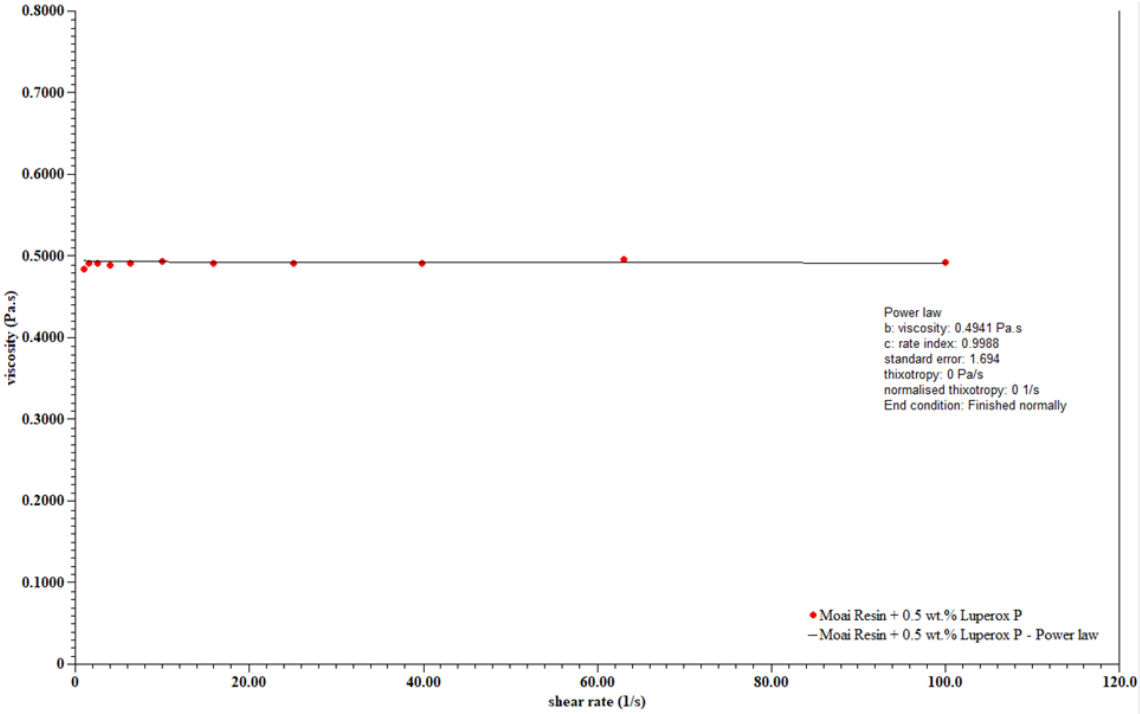

Figure A.8: Moai resin + Luperox P viscosity curve 1 s^{-1} to 100 s^{-1}.

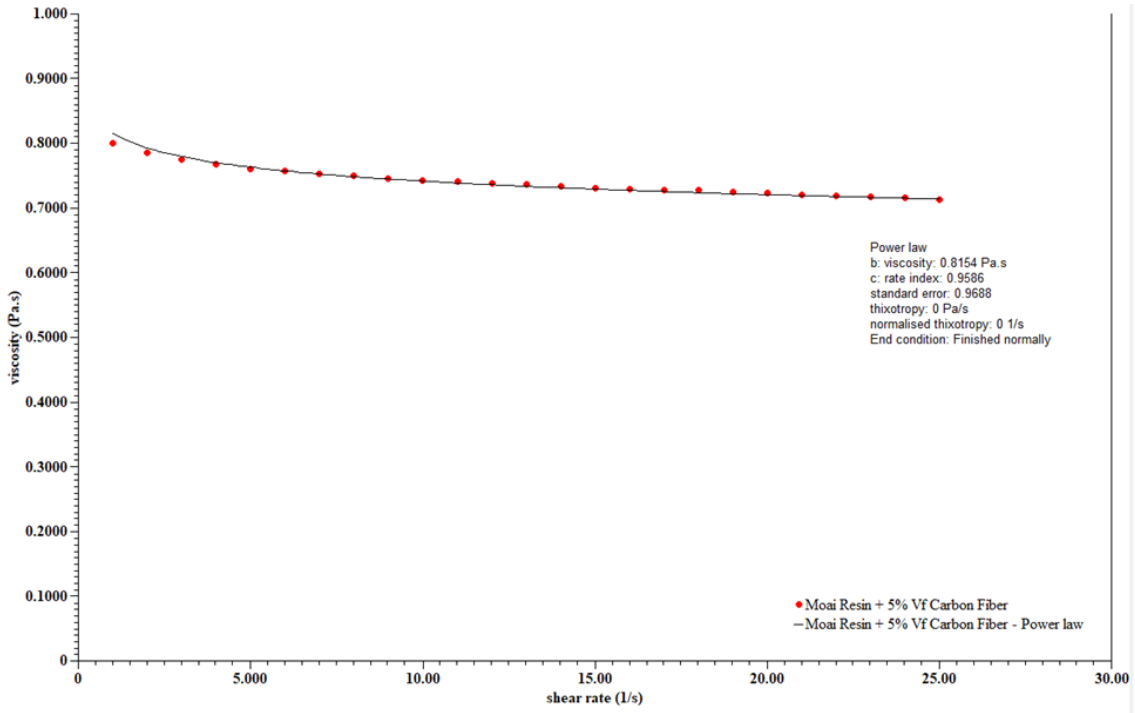

Figure A.9: Moai resin + carbon fiber viscosity curve 1 s^{-1} to 25 s^{-1}.

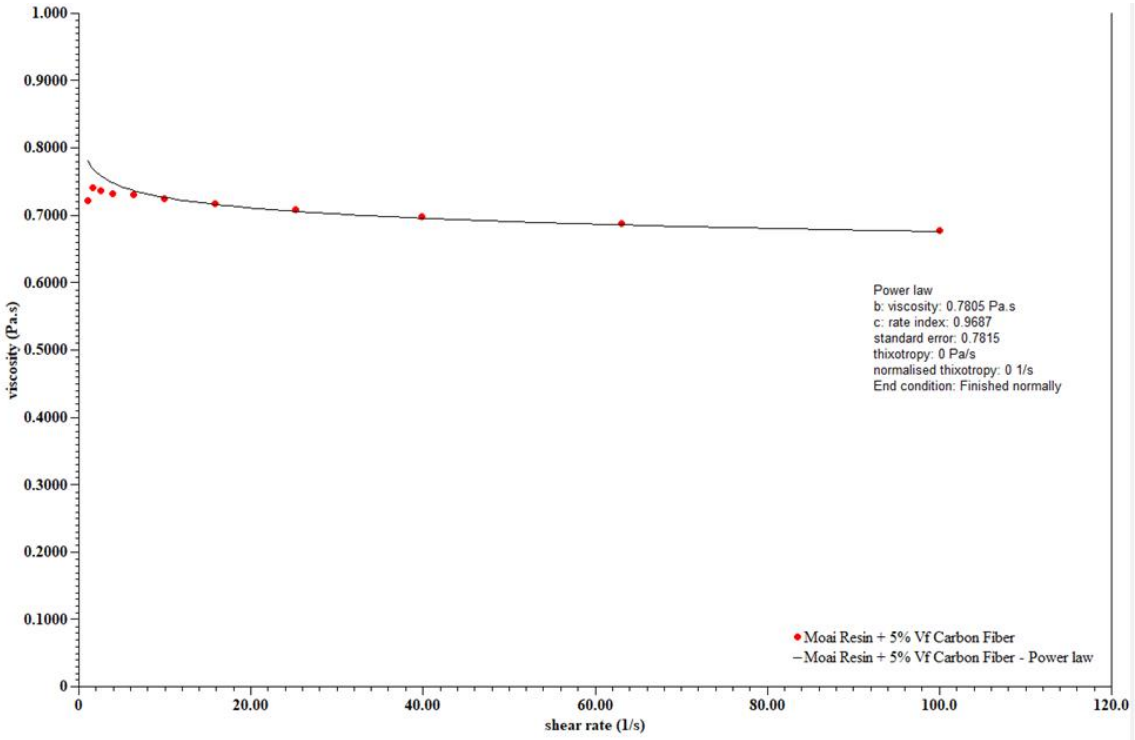

Figure A.10: Moai resin + carbon fiber viscosity curve 1 s^{-1} to 100 s^{-1}.

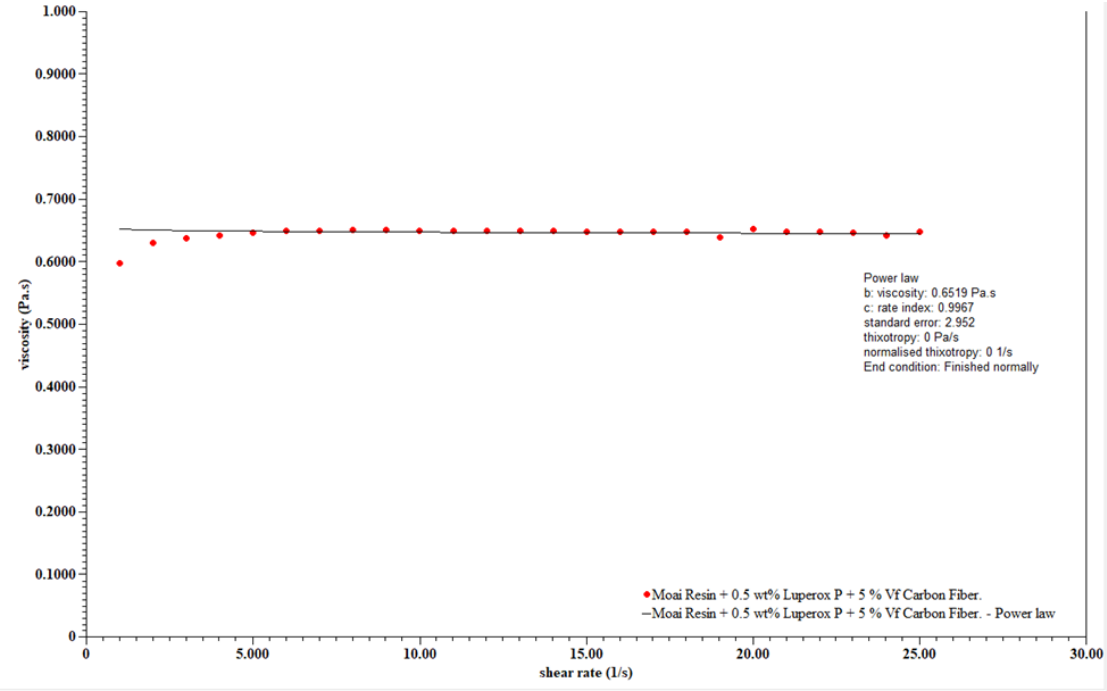

Figure A.11: Moai resin + carbon fiber + Luperox P viscosity curve 1 s^{-1} to 25 s^{-1}.

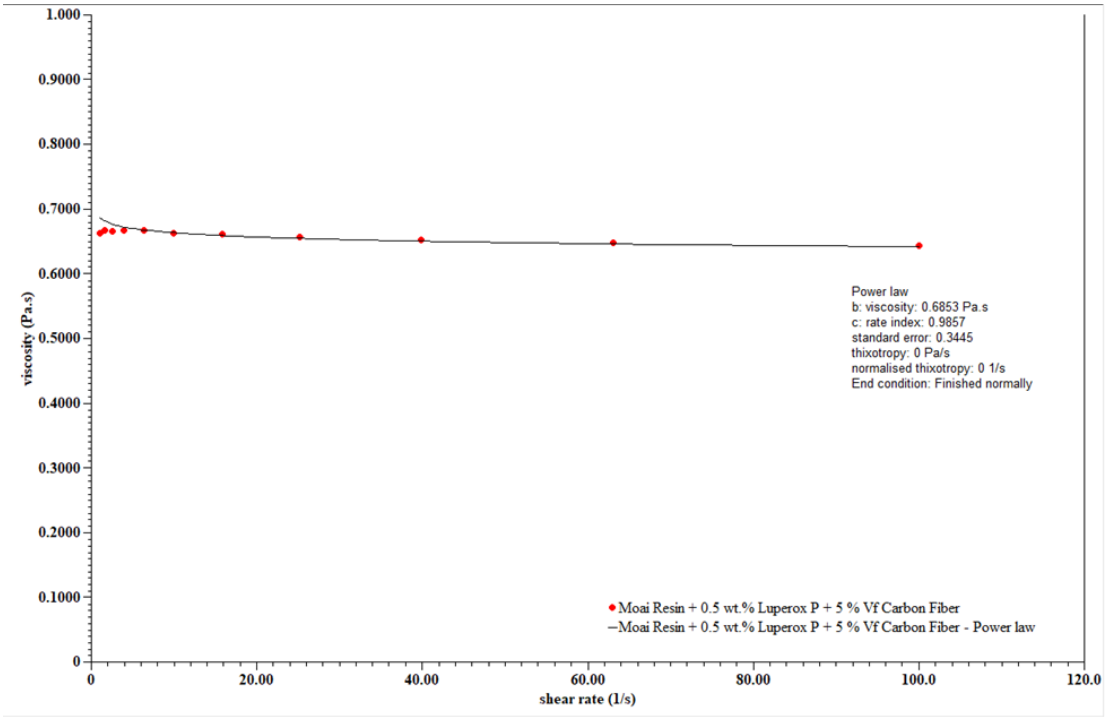

Figure A.12: Moai resin + carbon fiber + Luperox P viscosity curve 1 s^{-1} to 100 s^{-1}.

Table A.1: Fiber volume consistency for 100 μm layer height.

100 μm Layer Height			
	Top Weight (g)	**Middle Weight (g)**	**Bottom Weight (g)**
Crucible	6.0931	8.0662	7.7678
Before Burn off	6.2136	8.2070	7.9383
After Burn off	6.0994	8.0731	7.7742
Composite Mass	0.1205	0.1408	0.1705
Fiber Mass	0.0063	0.0069	0.0064
Fiber Weight %	5.2282	4.9006	3.7537
Average	5.2445	4.8363	3.5635
Standard Deviation	0.0230	0.0909	0.2689

Table A.2: Fiber volume consistency for 50 μm layer height.

50 μm Layer Height			
	Top Weight (g)	**Middle Weight (g)**	**Bottom Weight (g)**
Crucible	7.7620	8.0613	6.0937
Before Burn off	7.9545	8.2793	6.3391
After Burn off	7.7727	8.0709	6.1032
Composite Mass	0.1925	0.2180	0.2454
Fiber Mass	0.0107	0.0096	0.0095
Fiber Weight %	5.5584	4.4037	3.8712
Average	5.4544	4.4978	3.8813
Standard Deviation	0.1471	0.1331	0.0143

Table A.3: Density measurements results.

100 µm Layer Height 5%V_f Carbon Fiber + 0.5 wt.% Luperox P				
Sample	**Dry Weight (g)**	**Wet Weight (g)**	**Density (g/cm^3)**	**Submerged Wire Weight (g)**
1	1.2298	0.8488	1.2545	0.5993
2	1.2168	0.8465	1.2550	0.5993
50 µm Layer Height 5%V_f Carbon Fiber + 0.5 wt.% Luperox P				
Sample	**Dry Weight (g)**	**Wet Weight (g)**	**Density (g/cm^3)**	**Submerged Wire Weight (g)**
1	1.2582	0.8545	1.2544	0.5993
2	1.2456	0.8472	1.2485	0.5993
100 µm Layer Height 0.5 wt.% Luperox P				
Sample	**Dry Weight (g)**	**Wet Weight (g)**	**Density (g/cm^3)**	**Submerged Wire Weight (g)**
1	1.1958	0.8459	1.2424	0.6126
2	1.1866	0.8441	1.2424	0.6126

Table A.4: Void content measurement results.

100 µm Layer Height								
Sample	**Crucible (g)**	**Before Burn off (g)**	**After Burn off (g)**	**Composite Mass (g)**	**Fiber Mass (g)**	**Fiber Volume (%)**	**Matric Volume (%)**	**Void Content (%)**
1	7.7642	8.9973	7.8417	1.2331	0.0775	4.3646	94.4708	1.1646
2	8.0640	9.2859	8.1527	1.2219	0.0887	5.0411	93.4887	1.4702
50 µm Layer Height								
1	6.0954	7.3537	6.1505	1.2583	0.0551	3.0409	96.3922	0.5669
2	7.4096	8.6793	7.4763	1.2697	0.0667	3.6481	95.5109	0.8411

Table A.5: Shrinkage due to post-curing M100.

M100								
	Before Cure				After Cure			
Cube	X (mm)	Y (mm)	Z (mm)	Volume (mm^3)	X (mm)	Y (mm)	Z (mm)	Volume (mm^3)
1	9.83	9.84	10.4	1005.963	9.81	9.8	10.42	1001.758
2	9.86	9.74	10.38	996.8578	9.79	9.68	10.33	978.9452
3	9.79	9.84	10.58	1019.209	9.75	9.8	10.55	1008.053
4	9.74	9.74	10.58	1003.699	9.7	9.69	10.45	982.2269
5	9.74	9.75	10.48	995.2332	9.69	9.71	10.42	980.4168

Table A.6: Shrinkage due to post-curing M50.

M50								
	Before Cure				After Cure			
Cube	X (mm)	Y (mm)	Z (mm)	Volume (mm^3)	X (mm)	Y (mm)	Z (mm)	Volume (mm^3)
1	9.77	9.88	10.71	1033.811	9.7	9.85	10.74	1026.153
2	9.78	9.87	10.72	1034.787	9.76	9.82	10.73	1028.398
3	9.77	9.75	10.69	1018.303	9.69	9.74	10.75	1014.591
4	9.94	9.88	10.74	1054.745	9.95	9.83	10.7	1046.551
5	9.78	9.77	10.85	1036.724	9.75	9.72	10.76	1019.725

Table A.7: Shrinkage due to post-curing LP100.

LP100								
	Before Cure				After Cure			
Cube	X (mm)	Y (mm)	Z (mm)	Volume (mm^3)	X (mm)	Y (mm)	Z (mm)	Volume (mm^3)
1	9.8	9.85	10.54	1017.43	9.67	9.73	10.46	984.172
2	9.86	9.87	10.41	1013.08	9.62	9.75	10.31	967.026
3	9.73	9.75	10.44	990.417	9.61	9.62	10.39	960.537
4	9.8	9.75	10.45	998.498	9.66	9.62	10.37	963.676
5	9.86	9.87	10.43	1015.03	9.73	9.75	10.35	981.879

Table A.8: Shrinkage due to post-curing LP50.

LP50								
	Before Cure				After Cure			
Cube	X (mm)	Y (mm)	Z (mm)	Volume (mm^3)	X (mm)	Y (mm)	Z (mm)	Volume (mm^3)
1	9.84	9.85	10.65	1032.24	9.79	9.81	10.68	1025.71
2	9.78	9.82	10.63	1020.9	9.74	9.77	10.71	1019.16
3	9.77	9.76	10.74	1024.11	9.69	9.68	10.7	1003.65
4	9.73	9.74	10.68	1012.15	9.67	9.69	10.69	1001.68
5	9.75	9.86	10.74	1032.49	9.68	9.81	10.74	1019.88

Table A.9: Shrinkage due to post-curing CF100.

CF100								
	Before Cure				After Cure			
Cube	X (mm)	Y (mm)	Z (mm)	Volume (mm^3)	X (mm)	Y (mm)	Z (mm)	Volume (mm^3)
1	9.95	10.14	10.36	1045.25	9.89	10.11	10.23	1022.88
2	9.97	10.05	10.22	1024.03	9.96	9.99	10.22	1016.89
3	10.02	9.95	10.25	1021.91	9.99	9.9	10.32	1020.66
4	10.03	10.14	10.34	1051.62	9.98	10.08	10.35	1041.19
5	10.17	10.11	10.26	1054.92	10.12	10.04	10.22	1038.4

Table A.10: Shrinkage due to post-curing CF50.

CF50								
	Before Cure				After Cure			
Cube	X (mm)	Y (mm)	Z (mm)	Volume (mm^3)	X (mm)	Y (mm)	Z (mm)	Volume (mm^3)
1	10.01	10.16	10.4	1057.7	9.96	10.11	10.46	1053.28
2	10.13	10.08	10.45	1067.05	10.07	10.02	10.54	1063.5
3	10.13	10.15	10.46	1075.49	10.07	10.1	10.48	1065.89
4	9.98	10.03	10.45	1046.04	9.95	10.01	10.49	1044.8
5	10.05	10.13	10.53	1072.02	9.96	10.08	10.65	1069.23

APPENDIX B. STATISTICAL DATA

Table B.1: ANOVA summary for Young's modulus 0º print orientation.

Group	Count	Sum	Average	Variance		
M100-0	5	13.62	2.724	0.0035705	-	-
LP100-0	5	15.889	3.1778	0.0234822	-	-
CF100-0	5	16.451	3.2902	0.0810507	-	-
M50-0	5	14.074	2.8148	0.0229977	-	-
LP50-0	5	15.209	3.0418	0.0125272	-	-
CF50-0	5	17.311	3.4622	0.0290367	-	-
ANOVA						
Source of Variation	**SS**	**df**	**MS**	**F**	**P-value**	**F Critical**
Between Groups	1.99096946	5	0.39819389	13.836987	$2.0565*10^{-6}$	2.62065
Within Groups	0.69066	24	0.0287775	-	-	-
Total	2.68162946	29	-	-	-	-

Table B.2: Tukey HSD results Young's modulus 0º print orientation.

Treatments Pair	Tukey HSD Q Statistic	Tukey HSD p-value	Tukey HSD Inference
M100-0 vs LP100-0	5.9817	0.0035542	p<0.01
M100-0 vs CF100-0	7.4633	0.0010053	p<0.01
M100-0 vs M50-0	1.1969	0.8999947	insignificant
M100-0 vs LP50-0	4.189	0.0659969	insignificant
M100-0 vs CF50-0	9.7304	0.0010053	p<0.01
LP100-0 vs CF100-0	1.4816	0.894244	insignificant
LP100-0 vs M50-0	4.7848	0.0262724	p<0.05
LP100-0 vs LP50-0	1.7927	0.7746687	insignificant
LP100-0 vs CF50-0	3.7488	0.1235734	insignificant
CF100-0 vs M50-0	6.2664	0.0021738	p<0.01
CF100-0 vs LP50-0	3.2742	0.2268235	insignificant
CF100-0 vs CF50-0	2.2672	0.5922682	insignificant
M50-0 vs LP50-0	2.9922	0.312899	insignificant
M50-0 vs CF50-0	8.5336	0.0010053	p<0.01
LP50-0 vs CF50-0	5.5414	0.0075388	p<0.01

Table B.3: ANOVA summary for Young's modulus 90º print orientation.

Group	Count	Sum	Average	Variance		
M100-90	5	14.397	2.8794	0.0030163	-	-
LP100-90	5	15.892	3.1784	0.0673943	-	-
CF100-90	5	16.982	3.3964	0.5242093	-	-
M50-90	5	14.452	2.8904	0.1212383	-	-
LP50-90	5	14.129	2.8258	0.0097227	-	-
CF50-90	5	14.603	2.9206	0.0196288	-	-
ANOVA						
Source of Variation	**SS**	**df**	**MS**	**F**	**P-value**	**F Critical**
Between Groups	1.25392936	5	0.25078587	2.01918364	0.11204328	2.62065
Within Groups	2.9808388	24	0.12420161	-	-	-
Total	4.234768167	29	-	-	-	-

Table B.4: Tukey HSD results Young's modulus 90º print orientation.

Treatments Pair	Tukey HSD Q Statistic	Tukey HSD p-value	Tukey HSD Inference
M100-90 vs LP100-90	1.8971	0.7345185	insignificant
M100-90 vs CF100-90	3.2803	0.2251809	insignificant
M100-90 vs M50-90	0.0698	0.8999947	insignificant
M100-90 vs LP50-90	0.3401	0.8999947	insignificant
M100-90 vs CF50-90	0.2614	0.8999947	insignificant
LP100-90 vs CF100-90	1.3832	0.8999947	insignificant
LP100-90 vs M50-90	1.8273	0.7613445	insignificant
LP100-90 vs LP50-90	2.2372	0.6037964	insignificant
LP100-90 vs CF50-90	1.6357	0.8350009	insignificant
CF100-90 vs M50-90	3.2105	0.2444688	insignificant
CF100-90 vs LP50-90	3.6204	0.1464663	insignificant
CF100-90 vs CF50-90	3.0189	0.3039984	insignificant
M50-90 vs LP50-90	0.4099	0.8999947	insignificant
M50-90 vs CF50-90	0.1916	0.8999947	insignificant
LP50-90 vs CF50-90	0.6015	0.8999947	insignificant

Table B.5: ANOVA summary for Young's modulus printed at 100 μm layer height.

Group	Count	Sum	Average	Variance		
M100-0	5	13.62	2.724	0.0035705	-	-
LP100-0	5	15.889	3.1778	0.0234822	-	-
CF100-0	5	16.451	3.2902	0.0810507	-	-
M100-90	5	14.397	2.8794	0.0030163	-	-
LP100-90	5	15.892	3.1784	0.0673943	-	-
CF100-90	5	16.982	3.3964	0.5242093	-	-
ANOVA						
Source of Variation	**SS**	**df**	**MS**	**F**	**P-value**	**F Critical**
Between Groups	1.6295651	5	0.3259130	2.78271422	0.04040991	2.62065
Within Groups	2.8108932	24	0.1171205	-	-	-
Total	4.4404583	29	-	-	-	-

Table B.6: Tukey HSD results for Young's modulus printed at 100 μm layer height.

Treatments Pair	Tukey HSD Q Statistic	Tukey HSD p-value	Tukey HSD Inference
M100-0 vs LP100-0	2.9651	0.322048	insignificant
M100-0 vs CF100-0	3.6995	0.1316381	insignificant
M100-0 vs M100-90	1.0154	0.8999947	insignificant
M100-0 vs LP100-90	2.969	0.3207179	insignificant
M100-0 vs CF100-90	4.3934	0.0484687	$p<0.05$
LP100-0 vs CF100-0	0.7344	0.8999947	insignificant
LP100-0 vs M100-90	1.9497	0.7143055	insignificant
LP100-0 vs LP100-90	0.0039	0.8999947	insignificant
LP100-0 vs CF100-90	1.4283	0.8999947	insignificant
CF100-0 vs M100-90	2.6841	0.429128	insignificant
CF100-0 vs LP100-90	0.7305	0.8999947	insignificant
CF100-0 vs CF100-90	0.6939	0.8999947	insignificant
M100-90 vs LP100-90	1.9536	0.7127964	insignificant
M100-90 vs CF100-90	3.378	0.1998074	insignificant
LP100-90 vs CF100-90	1.4244	0.8999947	insignificant

Table B.7: ANOVA summary for Young's modulus printed at 50 μm layer height.

Group	Count	Sum	Average	Variance		
M50-0	5	14.074	2.8148	0.0229977	-	-
LP50-0	5	15.209	3.0418	0.0125272	-	-
CF50-0	5	17.311	3.4622	0.0290367	-	-
M50-90	5	14.452	2.8904	0.1212383	-	-
LP50-90	5	14.129	2.8258	0.0097227	-	-
CF50-90	5	14.603	2.9206	0.0196288	-	-
ANOVA						
Source of Variation	**SS**	**df**	**MS**	**F**	**P-value**	**F Critical**
Between Groups	1.4900436	5	0.29800872	8.31067016	$1.13*10^{-4}$	2.62065
Within Groups	0.8606056	24	0.03585856	-	-	-
Total	2.3506492	29	-	-	-	-

Table B.8: Tukey HSD results for Young's modulus printed at 50 μm layer height.

Treatments Pair	Tukey HSD Q Statistic	Tukey HSD p-value	Tukey HSD Inference
M50-0 vs LP50-0	2.6805	0.4305806	insignificant
M50-0 vs CF50-0	7.6447	0.0010053	p<0.01
M50-0 vs M50-90	0.8927	0.8999947	insignificant
M50-0 vs LP50-90	0.1299	0.8999947	insignificant
M50-0 vs CF50-90	1.2493	0.8999947	insignificant
LP50-0 vs CF50-0	4.9642	0.0196729	p<0.05
LP50-0 vs M50-90	1.7878	0.7765395	insignificant
LP50-0 vs LP50-90	2.5506	0.4827762	insignificant
LP50-0 vs CF50-90	1.4312	0.8999947	insignificant
CF50-0 vs M50-90	6.752	0.0010053	p<0.01
CF50-0 vs LP50-90	7.5148	0.0010053	p<0.01
CF50-0 vs CF50-90	6.3954	0.001736	p<0.01
M50-90 vs LP50-90	0.7628	0.8999947	insignificant
M50-0 vs LP50-0	2.6805	0.4305806	insignificant
M50-0 vs CF50-0	7.6447	0.0010053	p<0.01

Table B.9: ANOVA summary for tensile strength 0º print orientation.

Group	Count	Sum	Average	Variance		
M100-0	5	294.888	58.9776	25.7157088	-	-
LP100-0	5	184.331	36.8662	63.8093842	-	-
CF100-0	5	262.163	52.4326	13.3336853	-	-
M50-0	5	217.372	43.4744	59.4877828	-	-
LP50-0	5	251.5	50.3	62.082573	-	-
CF50-0	5	252.942	50.5884	42.9189113	-	-
ANOVA						
Source of Variation	**SS**	**df**	**MS**	**F**	**P-value**	**F Critical**
Between Groups	1465.00493	5	293.000987	6.57572013	$5.5152*10^{-4}$	2.62065
Within Groups	1069.39218	24	44.5580075	-	-	-
Total	2.68162946	29	-	-	-	-

Table B.10: Tukey HSD results tensile strength 0º print orientation.

Treatments Pair	Tukey HSD Q Statistic	Tukey HSD p-value	Tukey HSD Inference
M100-0 vs LP100-0	7.4069	0.0010053	p<0.01
M100-0 vs CF100-0	2.1924	0.6209932	insignificant
M100-0 vs M50-0	5.1935	0.0135044	p<0.05
M100-0 vs LP50-0	2.9068	0.3428317	insignificant
M100-0 vs CF50-0	2.8102	0.3792512	insignificant
LP100-0 vs CF100-0	5.2144	0.0130433	p<0.05
LP100-0 vs M50-0	2.2134	0.6129331	insignificant
LP100-0 vs LP50-0	4.5001	0.0411466	p<0.05
LP100-0 vs CF50-0	4.5967	0.0353984	p<0.05
CF100-0 vs M50-0	3.001	0.3099344	insignificant
CF100-0 vs LP50-0	0.7144	0.8999947	insignificant
CF100-0 vs CF50-0	0.6178	0.8999947	insignificant
M50-0 vs LP50-0	2.2866	0.5847886	insignificant
M50-0 vs CF50-0	2.3833	0.547652	insignificant
LP50-0 vs CF50-0	0.0966	0.8999947	insignificant

Table B.11: ANOVA summary for tensile strength 90º print orientation.

Group	Count	Sum	Average	Variance		
M100-90	5	342.617	68.5234	0.7425458	-	-
LP100-90	5	138.154	27.6308	510.090223	-	-
CF100-90	5	207.034	41.4068	4.9820447	-	-
M50-90	5	322.953	64.5906	2.7124953	-	-
LP50-90	5	344.35	68.87	35.2706625	-	-
CF50-90	5	58.439	11.6878	5.2346707	-	-
ANOVA						
Source of Variation	**SS**	**df**	**MS**	**F**	**P-value**	**F Critical**
Between Groups	14521.5012	5	2904.30024	31.1713487	$9.490*10^{-10}$	2.62065
Within Groups	2236.13056	24	93.1721070	-	-	-
Total	16757.6317	29	-	-	-	-

Table B.12: Tukey HSD results tensile strength 90º print orientation.

Treatments Pair	Tukey HSD Q Statistic	Tukey HSD p-value	Tukey HSD Inference
M100-90 vs LP100-90	9.473	0.0010053	p<0.01
M100-90 vs CF100-90	6.2817	0.0021166	p<0.01
M100-90 vs M50-90	0.9111	0.8999947	insignificant
M100-90 vs LP50-90	0.0803	0.8999947	insignificant
M100-90 vs CF50-90	13.1663	0.0010053	p<0.01
LP100-90 vs CF100-90	3.1913	0.2500577	insignificant
LP100-90 vs M50-90	8.5619	0.0010053	p<0.01
LP100-90 vs LP50-90	9.5533	0.0010053	p<0.01
LP100-90 vs CF50-90	3.6933	0.1327498	insignificant
CF100-90 vs M50-90	5.3706	0.0100509	p<0.05
CF100-90 vs LP50-90	6.362	0.0018398	p<0.01
CF100-90 vs CF50-90	6.8846	0.0010053	p<0.01
M50-90 vs LP50-90	0.9913	0.8999947	insignificant
M50-90 vs CF50-90	12.2552	0.0010053	p<0.01
LP50-90 vs CF50-90	13.2466	0.0010053	p<0.01

Table B.13: ANOVA summary for tensile strength printed at 100 μm layer height.

Group	Count	Sum	Average	Variance		
M100-0	5	294.888	58.9776	25.7157088	-	-
LP100-0	5	184.331	36.8662	63.8093842	-	-
CF100-0	5	262.163	52.4326	13.3336853	-	-
M100-90	5	342.617	68.5234	0.7425458	-	-
LP100-90	5	138.154	27.6308	510.090223	-	-
CF100-90	5	207.034	41.4068	4.9820447	-	-
ANOVA						
Source of Variation	**SS**	**df**	**MS**	**F**	**P-value**	**F Critical**
Between Groups	5714.61108	5	1142.92221	11.0842508	$1.287*10^{-5}$	2.62065
Within Groups	2474.69436	24	103.112265	-	-	-
Total	8189.30544	29	-	-	-	-

Table B.14: Tukey HSD results for tensile strength printed at 100 μm layer height.

Treatments Pair	Tukey HSD Q Statistic	Tukey HSD p-value	Tukey HSD Inference
M100-0 vs LP100-0	4.8691	0.0229462	$p<0.05$
M100-0 vs CF100-0	1.4413	0.8999947	insignificant
M100-0 vs M100-90	2.102	0.6557424	insignificant
M100-0 vs LP100-90	6.9028	0.0010053	$p<0.01$
M100-0 vs CF100-90	3.8692	0.104493	insignificant
LP100-0 vs CF100-0	3.4278	0.1877148	insignificant
LP100-0 vs M100-90	6.9711	0.0010053	$p<0.01$
LP100-0 vs LP100-90	2.0337	0.6820189	insignificant
LP100-0 vs CF100-90	0.9999	0.8999947	insignificant
CF100-0 vs M100-90	3.5433	0.1621786	insignificant
CF100-0 vs LP100-90	5.4615	0.0086307	$p<0.01$
CF100-0 vs CF100-90	2.428	0.5304711	insignificant
M100-90 vs LP100-90	9.0048	0.0010053	$p<0.01$
M100-90 vs CF100-90	5.9712	0.0036196	$p<0.01$
LP100-90 vs CF100-90	3.0336	0.2991623	insignificant

Table B.15: ANOVA summary for tensile strength printed at 50 μm layer height.

Group	Count	Sum	Average	Variance		
M50-0	5	217.372	43.4744	59.4877828	-	-
LP50-0	5	251.5	50.3	62.082573	-	-
CF50-0	5	252.942	50.5884	42.9189113	-	-
M50-90	5	322.953	64.5906	2.7124953	-	-
LP50-90	5	344.35	68.87	35.2706625	-	-
CF50-90	5	58.439	11.6878	5.2346707	-	-
ANOVA						
Source of Variation	**SS**	**df**	**MS**	**F**	**P-value**	**F Critical**
Between Groups	10307.3551	5	2061.47102	59.5493674	$9.669*10^{-13}$	2.62065
Within Groups	830.828382	24	34.6178492	-	-	-
Total	11138.1835	29	-	-	-	-

Table B.16: Tukey HSD results for tensile strength printed at 50 μm layer height.

Treatments Pair	Tukey HSD Q Statistic	Tukey HSD p-value	Tukey HSD Inference
M50-0 vs LP50-0	2.594	0.4653725	insignificant
M50-0 vs CF50-0	2.7036	0.4212952	insignificant
M50-0 vs M50-90	8.0251	0.0010053	p<0.01
M50-0 vs LP50-90	9.6515	0.0010053	p<0.01
M50-0 vs CF50-90	12.0803	0.0010053	p<0.01
LP50-0 vs CF50-0	0.1096	0.8999947	insignificant
LP50-0 vs M50-90	5.4311	0.0090823	p<0.01
LP50-0 vs LP50-90	7.0574	0.0010053	p<0.01
LP50-0 vs CF50-90	14.6744	0.0010053	p<0.01
CF50-0 vs M50-90	5.3215	0.0109131	p<0.05
CF50-0 vs LP50-90	6.9478	0.0010053	p<0.01
CF50-0 vs CF50-90	14.784	0.0010053	p<0.01
M50-90 vs LP50-90	1.6264	0.8385893	insignificant
M50-0 vs LP50-0	20.1054	0.0010053	p<0.01
M50-0 vs CF50-0	21.7318	0.0010053	p<0.01

Table B.17: ANOVA summary for flexural modulus 0º print orientation.

Group	Count	Sum	Average	Variance		
M100-0	5	12.584	2.5168	0.0049087	-	-
LP100-0	5	11.71	2.342	0.023488	-	-
CF100-0	5	12.958	2.5916	0.0039833	-	-
M50-0	5	12.737	2.5474	0.0001933	-	-
LP50-0	5	11.129	2.2258	0.0439837	-	-
CF50-0	5	13.229	2.6458	0.0121702	-	-
ANOVA						
Source of Variation	**SS**	**df**	**MS**	**F**	**P-value**	**F Critical**
Between Groups	0.64742056	5	0.12948411	8.75610500	$7.7833*10^{-5}$	2.62065
Within Groups	0.3549088	24	0.01478786	-	-	-
Total	1.00232936	29	-	-	-	-

Table B.18: Tukey HSD results flexural modulus 0º print orientation.

Treatments Pair	Tukey HSD Q Statistic	Tukey HSD p-value	Tukey HSD Inference
M100-0 vs LP100-0	3.2142	0.2434026	insignificant
M100-0 vs CF100-0	1.3754	0.8999947	insignificant
M100-0 vs M50-0	0.5627	0.8999947	insignificant
M100-0 vs LP50-0	5.3509	0.010389	p<0.05
M100-0 vs CF50-0	2.372	0.5519618	insignificant
LP100-0 vs CF100-0	4.5896	0.0357898	p<0.05
LP100-0 vs M50-0	3.7769	0.1188913	insignificant
LP100-0 vs LP50-0	2.1367	0.6424315	insignificant
LP100-0 vs CF50-0	5.5862	0.0069875	p<0.01
CF100-0 vs M50-0	0.8127	0.8999947	insignificant
CF100-0 vs LP50-0	6.7263	0.0010053	p<0.01
CF100-0 vs CF50-0	0.9966	0.8999947	insignificant
M50-0 vs LP50-0	5.9136	0.0039968	p<0.01
M50-0 vs CF50-0	1.8094	0.7682441	insignificant
LP50-0 vs CF50-0	7.7229	0.0010053	p<0.01

Table B.19: ANOVA summary for flexural modulus 90º print orientation.

Group	Count	Sum	Average	Variance		
M100-90	5	12.105	2.421	0.0027865	-	-
LP100-90	5	12.384	2.4768	0.0094907	-	-
CF100-90	5	11.549	2.3098	0.0059202	-	-
M50-90	5	13.146	2.6292	0.0032957	-	-
LP50-90	5	12.505	2.501	0.0407685	-	-
CF50-90	5	12.909	2.5818	0.0243977	-	-
ANOVA						
Source of Variation	**SS**	**df**	**MS**	**F**	**P-value**	**F Critical**
Between Groups	0.326314	5	0.0652628	4.51857792	0.00481529	2.62065
Within Groups	0.3466372	24	0.01444321	-	-	-
Total	0.6729512	29	-	-	-	-

Table B.20: Tukey HSD results flexural modulus 90º print orientation.

Treatments Pair	Tukey HSD Q Statistic	Tukey HSD p-value	Tukey HSD Inference
M100-90 vs LP100-90	1.0382	0.8999947	insignificant
M100-90 vs CF100-90	2.069	0.6684498	insignificant
M100-90 vs M50-90	3.8738	0.1038179	insignificant
M100-90 vs LP50-90	1.4885	0.8915884	insignificant
M100-90 vs CF50-90	2.9918	0.3130062	insignificant
LP100-90 vs CF100-90	3.1072	0.275549	insignificant
LP100-90 vs M50-90	2.8356	0.3695135	insignificant
LP100-90 vs LP50-90	0.4503	0.8999947	insignificant
LP100-90 vs CF50-90	1.9536	0.7127917	insignificant
CF100-90 vs M50-90	5.9428	0.0037998	$p<0.01$
CF100-90 vs LP50-90	3.5575	0.1591998	insignificant
CF100-90 vs CF50-90	5.0608	0.0168014	$p<0.05$
M50-90 vs LP50-90	2.3853	0.5468678	insignificant
M50-90 vs CF50-90	0.8819	0.8999947	insignificant
LP50-90 vs CF50-90	1.5034	0.8858666	insignificant

Table B.21: ANOVA summary for flexural modulus printed at 100 μm layer height.

Group	Count	Sum	Average	Variance		
M100-0	5	12.584	2.5168	0.0049087	-	-
LP100-0	5	11.71	2.342	0.023488	-	-
CF100-0	5	12.958	2.5916	0.0039833	-	-
M100-90	5	12.105	2.421	0.0027865	-	-
LP100-90	5	12.74	2.548	0.0537415	-	-
CF100-90	5	11.549	2.3098	0.0059202	-	-
ANOVA						
Source of Variation	**SS**	**df**	**MS**	**F**	**P-value**	**F Critical**
Between Groups	0.33067866	5	0.06613573	4.18456113	0.00708992	2.62065
Within Groups	0.3793128	24	0.0158047	-	-	-
Total	0.70999146	29	-	-	-	-

Table B.22: Tukey HSD results for flexural modulus printed at 100 μm layer height.

Treatments Pair	Tukey HSD Q Statistic	Tukey HSD p-value	Tukey HSD Inference
M100-0 vs LP100-0	3.1091	0.274957	insignificant
M100-0 vs CF100-0	1.3304	0.8999947	insignificant
M100-0 vs M100-90	1.704	0.8087667	insignificant
M100-0 vs LP100-90	0.5549	0.8999947	insignificant
M100-0 vs CF100-90	3.6818	0.1348276	insignificant
LP100-0 vs CF100-0	4.4395	0.0451671	$p<0.05$
LP100-0 vs M100-90	1.4051	0.8999947	insignificant
LP100-0 vs LP100-90	3.664	0.1381086	insignificant
LP100-0 vs CF100-90	0.5727	0.8999947	insignificant
CF100-0 vs M100-90	3.0344	0.298896	insignificant
CF100-0 vs LP100-90	0.7755	0.8999947	insignificant
CF100-0 vs CF100-90	5.0123	0.0181893	$p<0.05$
M100-90 vs LP100-90	2.2589	0.5954551	insignificant
M100-90 vs CF100-90	1.9779	0.7034754	insignificant
LP100-90 vs CF100-90	4.2368	0.0614543	insignificant

Table B.23: ANOVA summary for flexural modulus printed at 50 μm layer height.

Group	Count	Sum	Average	Variance		
M50-0	5	12.737	2.5474	0.0001933	-	-
LP50-0	5	11.129	2.2258	0.0439837	-	-
CF50-0	5	13.229	2.6458	0.0121702	-	-
M50-90	5	13.146	2.6292	0.0032957	-	-
LP50-90	5	12.505	2.501	0.0407685	-	-
CF50-90	5	12.909	2.5818	0.0243977	-	-
ANOVA						
Source of Variation	**SS**	**df**	**MS**	**F**	**P-value**	**F Critical**
Between Groups	0.59607376	5	0.11921475	5.73106063	0.00128690	2.62065
Within Groups	0.4992364	24	0.02080151	-	-	-
Total	1.09531016	29	-	-	-	-

Table B.24: Tukey HSD results for flexural modulus printed at 50 μm layer height.

Treatments Pair	Tukey HSD Q Statistic	Tukey HSD p-value	Tukey HSD Inference
M50-0 vs LP50-0	4.986	0.0189857	p<0.05
M50-0 vs CF50-0	1.5256	0.8773325	insignificant
M50-0 vs M50-90	1.2682	0.8999947	insignificant
M50-0 vs LP50-90	0.7194	0.8999947	insignificant
M50-0 vs CF50-90	0.5333	0.8999947	insignificant
LP50-0 vs CF50-0	6.5116	0.0014191	p<0.01
LP50-0 vs M50-90	6.2542	0.0022196	p<0.01
LP50-0 vs LP50-90	4.2666	0.0587536	insignificant
LP50-0 vs CF50-90	5.5193	0.0078275	p<0.01
CF50-0 vs M50-90	0.2574	0.8999947	insignificant
CF50-0 vs LP50-90	2.2449	0.6008153	insignificant
CF50-0 vs CF50-90	0.9922	0.8999947	insignificant
M50-90 vs LP50-90	1.9876	0.6997429	insignificant
M50-0 vs LP50-0	0.7349	0.8999947	insignificant
M50-0 vs CF50-0	1.2527	0.8999947	insignificant

Table B.25: ANOVA summary for flexural strength 0º print orientation.

Group	Count	Sum	Average	Variance		
M100-0	5	430.15	86.03	88.7898	-	-
LP100-0	5	139.67	27.934	29.15978	-	-
CF100-0	5	424.87	84.974	18.13463	-	-
M50-0	5	410.95	82.19	124.59595	-	-
LP50-0	5	119.32	23.864	13.88708	-	-
CF50-0	5	216.82	43.364	30.53483	-	-
ANOVA						
Source of Variation	**SS**	**df**	**MS**	**F**	**P-value**	**F Critical**
Between Groups	21909.2795	5	4381.85590	86.1716061	$1.566*10^{-14}$	2.62065
Within Groups	1220.40828	24	50.850345	-	-	-
Total	23129.6877	29	-	-	-	-

Table B.26: Tukey HSD results flexural strength 0º print orientation.

Treatments Pair	Tukey HSD Q Statistic	Tukey HSD p-value	Tukey HSD Inference
M100-0 vs LP100-0	18.2173	0.0010053	p<0.01
M100-0 vs CF100-0	0.3311	0.8999947	insignificant
M100-0 vs M50-0	1.2041	0.8999947	insignificant
M100-0 vs LP50-0	19.4936	0.0010053	p<0.01
M100-0 vs CF50-0	13.3789	0.0010053	p<0.01
LP100-0 vs CF100-0	17.8862	0.0010053	p<0.01
LP100-0 vs M50-0	17.0132	0.0010053	p<0.01
LP100-0 vs LP50-0	1.2762	0.8999947	insignificant
LP100-0 vs CF50-0	4.8384	0.0241039	p<0.05
CF100-0 vs M50-0	0.873	0.8999947	insignificant
CF100-0 vs LP50-0	19.1624	0.0010053	p<0.01
CF100-0 vs CF50-0	13.0478	0.0010053	p<0.01
M50-0 vs LP50-0	18.2894	0.0010053	p<0.01
M50-0 vs CF50-0	12.1748	0.0010053	p<0.01
LP50-0 vs CF50-0	6.1147	0.002827	p<0.01

Table B.27: ANOVA summary for flexural strength 90º print orientation.

Group	Count	Sum	Average	Variance		
M100-90	5	480.77	96.154	3.04043	-	-
LP100-90	5	73.17	14.634	9.05208	-	-
CF100-90	5	330.25	66.05	110.18255	-	-
M50-90	5	504.12	100.824	11.60793	-	-
LP50-90	5	65.78	13.156	0.39383	-	-
CF50-90	5	97.1	19.42	6.4429	-	-
ANOVA						
Source of Variation	**SS**	**df**	**MS**	**F**	**P-value**	**F Critical**
Between Groups	42483.8722	5	8496.77444	362.285020	$8.897*10^{-22}$	2.62065
Within Groups	562.87888	24	23.4532866	-	-	-
Total	43046.7511	29	-	-	-	-

Table B.28: Tukey HSD results flexural strength 90º print orientation.

Treatments Pair	Tukey HSD Q Statistic	Tukey HSD p-value	Tukey HSD Inference
M100-90 vs LP100-90	37.6398	0.0010053	p<0.01
M100-90 vs CF100-90	13.8998	0.0010053	p<0.01
M100-90 vs M50-90	2.1563	0.6349047	insignificant
M100-90 vs LP50-90	38.3222	0.0010053	p<0.01
M100-90 vs CF50-90	35.43	0.0010053	p<0.01
LP100-90 vs CF100-90	23.74	0.0010053	p<0.01
LP100-90 vs M50-90	39.7961	0.0010053	p<0.01
LP100-90 vs LP50-90	0.6824	0.8999947	insignificant
LP100-90 vs CF50-90	2.2098	0.6143173	insignificant
CF100-90 vs M50-90	16.056	0.0010053	p<0.01
CF100-90 vs LP50-90	24.4225	0.0010053	p<0.01
CF100-90 vs CF50-90	21.5302	0.0010053	p<0.01
M50-90 vs LP50-90	40.4785	0.0010053	p<0.01
M50-90 vs CF50-90	37.5862	0.0010053	p<0.01
LP50-90 vs CF50-90	2.8922	0.3481944	insignificant

Table B.29: ANOVA summary for flexural strength printed at 100 μm layer height.

Group	Count	Sum	Average	Variance		
M100-0	5	430.15	86.03	88.7898	-	-
LP100-0	5	139.67	27.934	29.15978	-	-
CF100-0	5	424.87	84.974	18.13463	-	-
M100-90	5	480.77	96.154	3.04043	-	-
LP100-90	5	73.17	14.634	9.05208	-	-
CF100-90	5	330.25	66.05	110.18255	-	-
ANOVA						
Source of Variation	**SS**	**df**	**MS**	**F**	**P-value**	**F Critical**
Between Groups	28448.9887	5	5689.79774	132.136874	$1.187*10^{-16}$	2.62065
Within Groups	1033.43708	24	43.0598783	-	-	-
Total	29482.4257	29	-	-	-	-

Table B.30: Tukey HSD results for flexural strength printed at 100 μm layer height.

Treatments Pair	Tukey HSD Q Statistic	Tukey HSD p-value	Tukey HSD Inference
M100-0 vs LP100-0	19.7968	0.0010053	p<0.01
M100-0 vs CF100-0	0.3598	0.8999947	insignificant
M100-0 vs M100-90	3.4499	0.1825546	insignificant
M100-0 vs LP100-90	24.3289	0.0010053	p<0.01
M100-0 vs CF100-90	6.8084	0.0010053	p<0.01
LP100-0 vs CF100-0	19.437	0.0010053	p<0.01
LP100-0 vs M100-90	23.2466	0.0010053	p<0.01
LP100-0 vs LP100-90	4.5321	0.0391507	p<0.05
LP100-0 vs CF100-90	12.9884	0.0010053	p<0.01
CF100-0 vs M100-90	3.8097	0.1135974	insignificant
CF100-0 vs LP100-90	23.9691	0.0010053	p<0.01
CF100-0 vs CF100-90	6.4485	0.0015818	p<0.01
M100-90 vs LP100-90	27.7788	0.0010053	p<0.01
M100-90 vs CF100-90	10.2582	0.0010053	p<0.01
LP100-90 vs CF100-90	17.5205	0.0010053	p<0.01

Table B.31: ANOVA summary for flexural strength printed at 50 μm layer height.

Group	Count	Sum	Average	Variance		
M50-0	5	410.95	82.19	124.595	-	-
LP50-0	5	119.32	23.86	13.887	-	-
CF50-0	5	216.82	43.36	30.535	-	-
M50-90	5	504.12	100.82	11.607	-	-
LP50-90	5	65.78	13.16	0.394	-	-
CF50-90	5	97.1	19.42	6.442	-	-
ANOVA						
Source of Variation	**SS**	**df**	**MS**	**F**	**P-value**	**F Critical**
Between Groups	32949.0764	5	6589.81528	210.916249	$5.179*10^{-19}$	2.62065
Within Groups	749.85008	24	31.2437533	-	-	-
Total	33698.9265	29	-	-	-	-

Table B.32: Tukey HSD results for flexural strength printed at 50 μm layer height.

Treatments Pair	Tukey HSD Q Statistic	Tukey HSD p-value	Tukey HSD Inference
M50-0 vs LP50-0	23.3327	0.0010053	p<0.01
M50-0 vs CF50-0	15.532	0.0010053	p<0.01
M50-0 vs M50-90	7.4543	0.0010053	p<0.01
M50-0 vs LP50-90	27.6164	0.0010053	p<0.01
M50-0 vs CF50-90	25.1105	0.0010053	p<0.01
LP50-0 vs CF50-0	7.8008	0.0010053	p<0.01
LP50-0 vs M50-90	30.7871	0.0010053	p<0.01
LP50-0 vs LP50-90	4.2836	0.0572648	insignificant
LP50-0 vs CF50-90	1.7778	0.7803873	insignificant
CF50-0 vs M50-90	22.9863	0.0010053	p<0.01
CF50-0 vs LP50-90	12.0844	0.0010053	p<0.01
CF50-0 vs CF50-90	9.5786	0.0010053	p<0.01
M50-90 vs LP50-90	35.0707	0.0010053	p<0.01
M50-0 vs LP50-0	32.5649	0.0010053	p<0.01
M50-0 vs CF50-0	2.5059	0.5005274	insignificant

Table B.33: ANOVA summary for fracture toughness 0º print orientation.

Group	Count	Sum	Average	Variance		
M100-0	3	1.88	0.627	0.0158	-	-
LP100-0	3	1.74	0.579	0.0333	-	-
CF100-0	3	2.18	0.726	0.0215	-	-
M50-0	3	1.96	0.654	0.0262	-	-
LP50-0	3	1.67	0.565	0.00695	-	-
CF50-0	3	1.72	0.573	0.00199	-	-
ANOVA						
Source of Variation	**SS**	**df**	**MS**	**F**	**P-value**	**F Critical**
Between Groups	0.0579	5	0.0116	0.6567	0.6627	3.1059
Within Groups	0.2116	12	0.0176	-	-	-
Total	0.2696	17	-	-	-	-

Table B.34: Tukey HSD results fracture toughness 0º print orientation.

Treatments Pair	Tukey HSD Q Statistic	Tukey HSD p-value	Tukey HSD Inference
M100-0 vs LP100-0	0.6127	0.8999947	insignificant
M100-0 vs CF100-0	1.3009	0.8999947	insignificant
M100-0 vs M50-0	0.3516	0.8999947	insignificant
M100-0 vs LP50-0	0.8007	0.8999947	insignificant
M100-0 vs CF50-0	0.6973	0.8999947	insignificant
LP100-0 vs CF100-0	1.9136	0.7305605	insignificant
LP100-0 vs M50-0	0.9644	0.8999947	insignificant
LP100-0 vs LP50-0	0.1879	0.8999947	insignificant
LP100-0 vs CF50-0	0.0846	0.8999947	insignificant
CF100-0 vs M50-0	0.9493	0.8999947	insignificant
CF100-0 vs LP50-0	2.1016	0.6619393	insignificant
CF100-0 vs CF50-0	1.9982	0.6996842	insignificant
M50-0 vs LP50-0	1.1523	0.8999947	insignificant
M50-0 vs CF50-0	1.0489	0.8999947	insignificant
LP50-0 vs CF50-0	0.1034	0.8999947	insignificant

Table B.35: ANOVA summary for fracture toughness 90º print orientation.

Group	Count	Sum	Average	Variance		
M100-90	3	2.07	0.688	0.00328	-	-
LP100-90	3	1.97	0.656	0.01353	-	-
CF100-90	3	1.73	0.578	0.00426	-	-
M50-90	3	1.71	0.570	0.00611	-	-
LP50-90	3	1.72	0.574	0.01757	-	-
CF50-90	3	1.70	0.568	0.00312	-	-
ANOVA						
Source of Variation	**SS**	**df**	**MS**	**F**	**P-value**	**F Critical**
Between Groups	0.0418	5	0.0084	1.0466	0.4350	3.1059
Within Groups	0.0957	12	0.0080	-	-	-
Total	0.1375	17	-	-	-	-

Table B.36: Tukey HSD results fracture toughness 90º print orientation.

Treatments Pair	Tukey HSD Q Statistic	Tukey HSD p-value	Tukey HSD Inference
M100-90 vs LP100-90	0.6247	0.8999947	insignificant
M100-90 vs CF100-90	2.1515	0.6437169	insignificant
M100-90 vs M50-90	2.2941	0.5916295	insignificant
M100-90 vs LP50-90	2.2268	0.616226	insignificant
M100-90 vs CF50-90	2.3371	0.5759534	insignificant
LP100-90 vs CF100-90	1.5267	0.8718246	insignificant
LP100-90 vs M50-90	1.6694	0.8197351	insignificant
LP100-90 vs LP50-90	1.602	0.8443332	insignificant
LP100-90 vs CF50-90	1.7123	0.804062	insignificant
CF100-90 vs M50-90	0.1427	0.8999947	insignificant
CF100-90 vs LP50-90	0.0753	0.8999947	insignificant
CF100-90 vs CF50-90	0.1856	0.8999947	insignificant
M50-90 vs LP50-90	0.0674	0.8999947	insignificant
M50-90 vs CF50-90	0.0429	0.8999947	insignificant
LP50-90 vs CF50-90	0.1103	0.8999947	insignificant

Table B.37: ANOVA summary for fracture toughness printed at 100 μm layer height.

Group	Count	Sum	Average	Variance		
M100-0	3	1.88	0.627	0.0158	-	-
LP100-0	3	1.74	0.580	0.0333	-	-
CF100-0	3	2.18	0.727	0.0215	-	-
M100-90	3	2.07	0.688	0.0033	-	-
LP100-90	3	1.97	0.656	0.0135	-	-
CF100-90	3	1.73	0.578	0.0043	-	-
ANOVA						
Source of Variation	**SS**	**df**	**MS**	**F**	**P-value**	**F Critical**
Between Groups	0.0533	5	0.0107	0.6972	0.6358	3.10588
Within Groups	0.1834	12	0.0153	-	-	-
Total	0.2367	17	-	-	-	-

Table B.38: Tukey HSD results for fracture toughness printed at 100 μm layer height.

Treatments Pair	Tukey HSD Q Statistic	Tukey HSD p-value	Tukey HSD Inference
M100-0 vs LP100-0	A vs B	0.6581	0.8999947
M100-0 vs CF100-0	A vs C	1.3974	0.8999947
M100-0 vs M100-90	A vs D	0.8644	0.8999947
M100-0 vs LP100-90	A vs E	0.413	0.8999947
M100-0 vs CF100-90	A vs F	0.69	0.8999947
LP100-0 vs CF100-0	B vs C	2.0555	0.6787622
LP100-0 vs M100-90	B vs D	1.5225	0.8733787
LP100-0 vs LP100-90	B vs E	1.0712	0.8999947
LP100-0 vs CF100-90	B vs F	0.0318	0.8999947
CF100-0 vs M100-90	C vs D	0.533	0.8999947
CF100-0 vs LP100-90	C vs E	0.9843	0.8999947
CF100-0 vs CF100-90	C vs F	2.0873	0.6671383
M100-90 vs LP100-90	D vs E	0.4513	0.8999947
M100-90 vs CF100-90	D vs F	1.5543	0.8617563
LP100-90 vs CF100-90	E vs F	1.103	0.8999947

Table B.39: ANOVA summary for fracture toughness printed at 50 μm layer height.

Group	Count	Sum	Average	Variance		
M50-0	3	1.96	0.654	0.0262	-	-
LP50-0	3	1.70	0.565	0.0070	-	-
CF50-0	3	1.72	0.573	0.0020	-	-
M50-90	3	1.71	0.570	0.0061	-	-
LP50-90	3	1.72	0.574	0.0176	-	-
CF50-90	3	1.70	0.568	0.0031	-	-
ANOVA						
Source of Variation	**SS**	**df**	**MS**	**F**	**P-value**	**F Critical**
Between Groups	0.0176	5	0.0035	0.3416	0.8780	3.10588
Within Groups	0.1240	12	0.0103	-	-	-
Total	0.1416	17	-	-	-	-

Table B.40: Tukey HSD results for fracture toughness printed at 50 μm layer height.

Treatments Pair	Tukey HSD Q Statistic	Tukey HSD p-value	Tukey HSD Inference
M50-0 vs LP50-0	1.5057	0.8794967	insignificant
M50-0 vs CF50-0	1.3707	0.8999947	insignificant
M50-0 vs M50-90	1.4243	0.8999947	insignificant
M50-0 vs LP50-90	1.3651	0.8999947	insignificant
M50-0 vs CF50-90	1.462	0.8954682	insignificant
LP50-0 vs CF50-0	0.1351	0.8999947	insignificant
LP50-0 vs M50-90	0.0815	0.8999947	insignificant
LP50-0 vs LP50-90	0.1407	0.8999947	insignificant
LP50-0 vs CF50-90	0.0437	0.8999947	insignificant
CF50-0 vs M50-90	0.0536	0.8999947	insignificant
CF50-0 vs LP50-90	0.0056	0.8999947	insignificant
CF50-0 vs CF50-90	0.0913	0.8999947	insignificant
M50-90 vs LP50-90	0.0592	0.8999947	insignificant
M50-0 vs LP50-0	0.0377	0.8999947	insignificant
M50-0 vs CF50-0	0.0969	0.8999947	insignificant